

NORTHWESTERN UNIVERSITY

Rheological Modeling and Texture Design for Advanced Lubrication

A DISSERTATION

SUBMITTED TO THE GRADUATE SCHOOL
IN PARTIAL FULFILLMENT OF THE REQUIREMENTS

for the degree

DOCTOR OF PHILOSOPHY

Field of Mechanical Engineering

By

Pinzhi Liu

EVANSTON, ILLINOIS

December 2016

© Copyright by Pinzhi Liu 2016

All Rights Reserved

Abstract

Rheological Modeling and Texture Design for Advanced Lubrication

Pinzhi Liu

Tribological behaviors of lubricated interfaces are strongly affected by the interactions between mating surfaces and the rheological properties of the lubricant between them. This research aims to improve lubrication through two approaches: 1) designing surface textures for lubrication enhancement and adhesion reduction, and 2) developing lubricants of desired rheology.

Molecular dynamics (MD) simulations enable us to predict the properties of a lubricant based on its molecular structures. However, due to the time- and length-scale limitations, direct viscosity calculations cannot be achieved for lubricants under a high pressure or for molecules with high molecular weights. To overcome such challenges, 1) direct Non-equilibrium molecular dynamics (NEMD) simulations and a time-temperature superposition (TTS)-based extrapolation from the NEMD at elevated temperatures were used to calculate the high-pressure viscosities of a main constituent of a synthetic base stock, 1-Decene trimer, and the pressure-viscosity coefficient was acquired; 2) The shear-thinning behavior was correlated with the molecular conformation, which is quantified using the radius of gyration, and the critical shear rates for 1-Decene trimer, squalane, and an olefin-copolymer of medium molecular weight at various

pressures and temperatures were predicted using the change in the radius of gyration; 3) Viscosities of high molecular weight Polyethylene (PE) and Poly- α -olefin (PAO) fluids, representing a linear polymer and a branched polymer, respectively, were predicted using an empirical-theoretical structural-viscosity model, where the structural factors are calculated through MD only.

Adhesion reduction may be accomplished by means of surface textures. A high precision manufacturing process was developed. Adequately designed surface textures were applied on the drill bits, and adhesion reduction and tool life improvements were observed for drilling of the metal material, a Titanium alloy. A flat-flat numerical model was developed for understanding the effect on the load capacity owing to the surface textures. A wide range of texture geometries was studied, and the geometric parameters were optimized based on the boundary conditions. Empirical equations were established based on the simulated results.

The results in this study provide multiple tools for advancing the understanding of lubrication performances at the lubricating interfaces and designing of mating surface topography and the lubricant between them. The rheological modeling of the lubricant enables us to predict the viscosities of lubricants based on their molecular structures and the operating conditions, such as temperature, pressure, and shear rates. The predictive capabilities of the models enable us to develop and tailor the lubricants to offer optimal performances at the specific working conditions. Meanwhile, guidelines for texture design and promising texture

patterns were provided. At the given working conditions, either one or both of these solutions can be utilized to seek for solutions for improving tribological performances of lubricating interfaces.

Acknowledgements

First and foremost, I would like to express my sincere gratitude to my advisor, Professor Q. Jane Wang, for her guidance and support throughout my PhD study. Professor Wang's expert advice, direction, and patience have made my research time at Northwestern University a valuable experience. Her passion in research and life, insights into problems, will be an inspiration to me throughout my career.

I am grateful to Professor Leon M. Keer, Professor Sinan Keten, and Dr. Ning Ren for serving in my thesis committee. I enjoyed the discussions with them and appreciate their invaluable suggestions to my research work. Professor Keer's knowledge of mechanics and attention to details have always kept my modeling process honest and sound, and avoiding jumping to conclusions. When I discussed my PhD proposal with Prof. Keten, he said that I should have a backup plan if the MD simulations don't work as hoped, which was essentially all that I did after my PhD proposal. Dr. Ning Ren provided valuable industry insights and directions for the rheological modeling research, and also provided test materials for validations.

I would also like to thank Dr. Tiffany Davis Ling, Dr. Chengjiao Yu for their help on laser surface texturing; Dr. Shangwu Xiong, Dr. Zhanjiang Wang, Dr. Jordan Liu on texture modeling; Dr. Hualong Yu, Dr. Yifeng He, Mr. Jie Lu and Dr. Thomas Zolper on rheological modeling, especially Dr. Hualong Yu for showing the steps and falls in the MD simulations. I thank the faculty of Northwestern University including Prof. Jian Cao, Prof. Tobin Marks, Prof. Yip-Wah

Chung for a range of discussions, advices and recommendations that they have provided. The assistances from the Mechanical Engineering staff, Ms. Pat Dyess, Brianna Mello, Sinta Kulanda, Amy Masters, and from the international office staff, Ms. Stephanie Cisnero, are also acknowledged.

My gratitude extends to colleagues and friends Drs. Xingliang He, Wei Chen, Zhe Li, Christie Twist, Lechun Xie, Qinghua Zhou, Yang Bai, Xiangyu Li, Yang Li, Peidong Han, Zhongbi Chen, Zitao Zhang, and Mr. Thomas Gu, Zhong Liu, Blake Johnson, Mengqi Zhang, Jingchuan Liu for their help and friendship. I wish to thank all visiting professors and scholars in the Tribology group for their help and discussions.

I am also grateful for the financial supports that I received from Ashland Inc., NU-Ford-Boeing Alliance, NIST foundation (collaboration with Caterpillar Inc.), and the Walter P. Murphy fellowship; the computational resources and staff contributions provided for the Quest high performance computing facility at Northwestern University which is jointly supported by the Office of the Provost, the Office for Research, and Northwestern University Information Technology.

Finally, I wish to express my deep appreciation and love to my family for their continuous support.

Abbreviations

EHL	Elastohydrodynamic Lubrication
HTHS	High-Temperature-High-Shear
LAMMPS	Large-scale Atomic/Molecular Massively Parallel Simulator
MD	Molecular Dynamics
MSD	Mean-Square Displacement
MSDS	Material Safety Data Sheet
NEMD	Non-equilibrium Molecular Dynamics
OCP	Olefin-Copolymer
PAO	Poly- α -olefin
PE	Polyethylene
RMS	Root Mean Square
TTPS	Time-Temperature-Pressure Superposition
TTS	Time-Temperature Superposition
UA	United Atom
VM	Viscosity Modifier
VI	Viscosity Index

Nomenclature

Rome Letters

a	Exponent of the Berry and Fox model
a_B	Ratio of the branch atomic length to the main chain spacer length
a_m	Parametric constants for the torsional interactions [Kcal/mol]
A	Size of the dimple along the flow direction [mm]
B	Size of the dimple perpendicular to the flow direction [mm]
B_B	Number of branches
$C^1(t)$	Reorientation autocorrelation function
$C_{20}, C_{40}, C_{76}, C_{90}$	Each molecule contains 20 carbons, 40 carbons, 76 carbons, 90 carbons
d	Depth of the dimple [μm]
d_r, d_s	Incremental movement in the radial and scanning direction [mm]
d_w	Effective working diameter of the laser beam [μm]
D	$D=d/H_{ref}$, non-dimensionalized depth
D_s	Self-diffusion coefficient [$\text{\AA}^2/\text{ns}$]
$\mathbf{e}_1(t), \mathbf{e}_1(0)$	Unit vectors representing the longest principal axis of the molecule ellipsoid of inertia at a time interval t and at the initial point
f_B	Branch functionality

g	Ratio between the mean square radius of gyration of the branch content to that of a linear chain
G	Effective shear modulus [MPa]
G_R	Effective shear modulus at the reference state [MPa]
h	Local thickness of the film [μm]
H_{ref}	Reference film thickness [μm]
k_{str}	Force constant for the bond-stretching interactions [Kcal/(mol \AA^2)]
k_{ben}	Force constant for the bond-bending interactions [Kcal/(mol rad^2)]
l, l_{eq}	Distance and equilibrium distance for bond-stretching [\AA]
L	Length and width of the solution domain [mm]
M	Molecular weight of the molecule [g/mol]
n	Power-law exponent in the Carreau and Carreau-Yasuda equation
n_{Rg}	Power-law exponent for the Carreau-Yasuda type equation for R_g
N_0	Avogadro's number
N_1, N_2	Number of dimples along the perpendicular and the flow direction
O	Overlap for laser texturing [%]
p	Local pressure [bar]
p_0	Ambient pressure [bar]
p_c	Cavitation pressure [bar]

P_{avg}	Average generated pressure [bar]
P	Pressure [MPa]
P	$P=P_{avg}/p_0$, non-dimensionalized generated pressure
$P_{mKWW}(t)$	Modified Kohlrausch-Williams-Watts (mKWW) function
r	Distance between the particles [\AA]
$\mathbf{R}_{cm}(t)$	Location of the molecule's center of mass at time t
R_g	Radius of gyration [\AA]
$\langle s^2 \rangle_0$	Unperturbed mean square radius of gyration [\AA^2]
$\langle s^2 \rangle_{br}$, $\langle s^2 \rangle_l$	Branched and linear mean square radii of gyration [\AA^2]
T	Temperature [K] or [$^{\circ}\text{C}$]
T_R	Reference temperature [K]
U	Relative speed between the mating surface [m/s]
v_0	Specific volume [cm^3/g]
$V_{ben}(\theta)$	Bond-bending interactions [Kcal]
$V_{LJ}(r)$	Pairwise Lennard-Jones potential [Kcal]
$V_{str}(l)$	Bond-stretching interactions [Kcal]
$V_{tor}(\phi)$	The torsional interactions [Kcal]
x	Cartesian coordinate (sliding direction) [mm]
X	$X=x/L$, non-dimensionalized x -coordinate

X	Viscosity dimensional factor
X_c	Critical dimensional factor
y	Cartesian coordinate (perpendicular to the sliding direction) [mm]
Y	$Y=y/L$, non-dimensionalized y-coordinate
Z	Chain length

Greek Letters

α	Pressure-viscosity coefficient [1/GPa]
α_0	Ambient pressure-viscosity coefficient [1/GPa]
α^*	Reciprocal asymptotic isoviscous pressure [1/GPa]
β	Width of the stretched exponential decay
$\dot{\gamma}$	Shear rate [s^{-1}]
$\dot{\gamma}_{cr}$	Critical shear rate [s^{-1}]
Γ	Gamma function
$\Delta d, \Delta D$	Variation in texture depth [μm]
$\Delta z, \Delta Z$	Distance from focal point [mm]
ε_{ij}	Depth of the potential well [Kcal]
$\zeta_0(T)$	Monomeric friction coefficient [cp]
η	Dynamic viscosity [cp]

η_0	Dynamic viscosity at 0.1 MPa [cp]
η_1	Dynamic viscosity at zero shear rate (1 st Newtonian) [cp]
η_R	Dynamic viscosity at the reference state [cp]
θ, θ_{eq}	Angle and equilibrium angle for bond-bending [°]
λ	Critical dimple size
ν	Kinematic viscosity [cSt]
ρ	Density of the lubricant [g/cm ³]
ρ_c	Averaged density in the cavitation region [g/cm ³]
ρ_R	Density of the lubricant at the reference state [g/cm ³]
σ_{ij}	Lennard-Jones size [Å]
τ	Rotational relaxation time [ns]
τ_0, τ_{kWW}	Two characteristic times of the mKWW function [ns]
φ_2	Volume fraction
ϕ	Torsional angle [°]
χ	Weight factor for the modified Kohlrausch-Williams-Watts (mKWW) function

Dedication

I dedicate this thesis to my wife, Shicong Zhou, for her support, my one-year old daughter, Abigail, and my parents.

Table of Contents

Abstract.....	3
Acknowledgements.....	6
Abbreviations	8
Nomenclature	9
Dedication.....	14
Table of Contents	15
List of Figures.....	17
List of Tables.....	24
Chapter 1 Introduction	25
1.1 Research Background	25
1.2 Research Methodology	26
Chapter 2 Pressure-Viscosity Coefficient Calculations for Hydrocarbon Base Oil.....	30
2.1 Introduction.....	31
2.2 Model Description	37
2.3 Molecular Dynamics Simulation Details for 1-Decene Trimer	40
2.4 Simulation Results	44
2.4.1 Validations of the Kinematic Viscosity and Density.....	44
2.4.2 Evaluations of the Relaxation Time	46
2.4.3 Viscosity Calculations at Low and High Pressures.....	47
2.4.4 Comparisons of the α Value with the Experimental Data	52
2.5 Chapter Summary	55
Chapter 3 Predicting the Critical Shear Rates of Hydrocarbon Lubricants	56
3.1 Introduction.....	57
3.2 Model Description	59
3.3 Molecular Dynamics Simulation Details for Squalane, 1-Decene Trimer, and OCP	62
3.4 Results and Discussions.....	64
3.4.1 Model Validation: Shear Viscosities of Squalane.....	64
3.4.2 Change in the Radius of Gyration under Shearing in the Non-Newtonian Regime.....	66
3.4.3 Comparisons between the Critical Shear Rates Calculated from the Viscosity Curves and those from the Radius of Gyration Curves.....	68
3.4.4 Time-Temperature-Pressure Superpositioning (TTPS) of the Viscosity and the Radius of Gyration	75
3.5 Chapter Summary	77
Chapter 4 Viscosity Modeling of Synthetic Polymer Lubricants	79
4.1 Introduction.....	80

4.2	Structural-Viscosity Model.....	81
4.3	Molecular Dynamics Simulation Setups for Polyethylene and Poly- α -olefin.....	85
4.4	Simulation Results	86
4.4.1	Validations of the Radius of Gyration Calculations	86
4.4.2	Estimations of the Critical Dimensional Factor, X_c	89
4.4.3	Viscosity Predictions and Comparisons with the Experimental Data.....	90
4.5	Chapter Summary	93
Chapter 5	Laser Surface Texturing for Reducing Adhesion at the Contact and Rubbing Interfaces.....	95
5.1	Introduction.....	95
5.2	Design and Optimization of the Laser Texturing Process	99
5.3	Fixture Design and Processing Method for Texturing Cylindrical Workpieces	104
5.4	Surface Texturing High-Speed Drill Bit Margins for Adhesion Reduction.....	108
5.4.1	Laser Surface Texturing Drill Bit Margins	108
5.4.2	Drilling Test Results and Discussions.....	114
5.5	Chapter Summary	118
Chapter 6	Understanding the Hydrodynamics of Surface Textures.....	119
6.1	Introduction.....	120
6.2	Numerical Model of a Flat-Flat Interface with Textures	121
6.3	Numerical Results and Discussions.....	126
6.3.1	Design and Optimization of a Single Texture	126
6.3.2	Design and Optimization of Multiple Textures.....	134
6.3.3	Influence of the Original Surface Roughness	137
6.3.4	Cavitation Effect	138
6.4	Chapter Summary	141
Chapter 7	Conclusions	144
References	151

List of Figures

Figure 1.1 Schematic of the Stribeck curve. Based on the lubrication parameter: $\eta V/P$, lubrication regimes can be divided into boundary lubrication (BL), mixed lubrication (ML), elastohydrodynamic lubrication (EHL) and hydrodynamic lubrication (HL) regimes.	26
Figure 1.2 Proposed approaches for improving the tribological behaviors of lubricating interfaces in different lubrication regimes.....	29
Figure 2.1 Typical change in the shear viscosity with an increasing shear rate.	36
Figure 2.2 Molecular structure of the 1-Decene trimer.....	37
Figure 2.3 Flow chart for calculation of the α value of alkanes.	40
Figure 2.4 Kinematic viscosity of 1-Decene trimer vs. the temperature at 0.1 MPa pressure. The dynamic viscosity is fitted to Equation 2.2, and then converted into kinematic viscosity using the calculated density.	45
Figure 2.5 Calculated density of 1-Decene trimer vs. temperature at 0.1 MPa pressure. A clear transition can be observed around 680 K, suggesting a change from liquid state to gas state.	45
Figure 2.6 mKWW fit of the reorientation autocorrelation function of the longest principal axis of the molecule ellipsoid of inertia at 400 MPa, 100 °C, fitted to Equation 2.5, to acquire the relaxation time.....	46
Figure 2.7 Calculated viscosities vs. the total calculation time at various pressures. The viscosity values stabilize within 100 ns.	48
Figure 2.8 Calculated viscosities at different shear rates at 600 MPa, 175 °C. The arrow indicates the estimated critical shear rate calculated from the reciprocal of the rotational relaxation time.	49
Figure 2.9 Viscosities calculated and extrapolated for 600 MPa.....	50
Figure 2.10 Viscosities calculated and extrapolated for 800 MPa.....	51
Figure 2.11 Viscosities calculated and extrapolated for 1 GPa.....	51

- Figure 2.12 Semi-log plot of the viscosity vs. pressure for the 1-Decene trimer. The trend shows a systematic difference between the two curves but their slopes are similar. 54
- Figure 2.13 Relative viscosity after normalization with the viscosity value at 0.1 MPa. 54
- Figure 3.1 A typical shear thinning curve. Critical shear rate $\dot{\gamma}_{cr}$ is defined as the onsite of temporary shear thinning. 58
- Figure 3.2 A spherically conformed polymer (left) and its alignment (right) with the shear field at sufficiently high shear rates. 60
- Figure 3.3 Flowchart for the simulation. 61
- Figure 3.4 Molecular Structures of (a) squalane, (b) PAO 4 and (c) OCP. 63
- Figure 3.5 Model validation: Shear thinning curves for squalane at (a) State 1: 0.1 MPa, 40 °C, (b) State 2: 0.1 MPa, 60 °C, and (c) State 3: 316 MPa, 100 °C, compared to the MD results in [46]. 66
- Figure 3.6 Variation of the radius of gyration vs. simulation time. The radius of gyration of the molecule increased under a sufficiently high shear rate. 67
- Figure 3.7 (a) Viscosity and (b) the radius of gyration calculations for PAO 4 at various shear rates (log scale). Two lines can be drawn for the 1st Newtonian and the shear thinning regimes. The cross point of the two lines is an estimation of the critical shear rate value, which are $5.6 \times 10^8 \text{ s}^{-1}$ and $6.7 \times 10^8 \text{ s}^{-1}$, respectively. 68
- Figure 3.8 The shear thinning and R_g curves for PAO 4 at (a) State 1: 0.1 MPa, 40 °C, (b) State 2: 0.1 MPa, 100 °C, (c) State 3: 0.1 MPa, 150 °C, (d) State 4: 250 MPa, 40 °C, (e) State 5: 250 MPa, 100 °C, (f) State 6: 600 MPa, 175 °C. The critical shear rate reached below 10^8 s^{-1} for State 4, and cannot be properly captured directly through viscosity calculation, whereas it can be estimated using the radius of gyration. The MD calculated viscosity (square) and the radius of gyration (circle) are fitted using Equations 3.2 and 3.5, respectively. 72
- Figure 3.9 The shear thinning and R_g curves for OCP at (a) State 1: 0.1 MPa, 100 °C, (b) State 2: 0.1 MPa, 150 °C, (c) State 3: 0.1 MPa, 200 °C, and (d) State 4: 250 MPa, 200 °C. The MD calculated viscosity (square) and R_g (circle) are fitted using Equations 3.2 and 3.5, respectively. 73

- Figure 3.10 The shear thinning and R_g curves for squalane at (a) State 1: 0.1 MPa, 40 °C, (b) State 2: 0.1 MPa, 100 °C, and (c) State 3: 316 MPa, 100 °C. The MD calculated viscosity (square) and the radius of gyration (circle) are fitted using Equations 3.2 and 3.5, respectively. 74
- Figure 3.11 Critical shear rates of (a) PAO 4, (b) OCP, and (c) squalane at various states. The critical shear rates are fitted from calculations of the viscosity and the radius of gyration using Equations 3.2 and 3.5, respectively..... 75
- Figure 3.12 The reduced viscosity and the reduced R_g vs. the reduced shear rate for PAO4 ((a) and (b)), OCP ((c) and (d)), and squalane ((e) and (f)). 77
- Figure 4.1 Flow chart for the structural-viscosity model..... 85
- Figure 4.2 Structure of PAO at $Z=6$ 86
- Figure 4.3 Radii of gyration calculated for Polyethylenes of various molecular weights, the values are plotted in the log scale, and curvefitted to acquire the exponent..... 87
- Figure 4.4 Calculated ratio of radii of gyration, g , normalized by that of 1-Decene trimer compared with that from the Bonchev model [92]. 88
- Figure 4.5 Calculated MSD for PE with $Z=76$, 140 and 200, respectively. The self-diffusion coefficient is proportional to the slope of the curve..... 89
- Figure 4.6 Calculated self-diffusion coefficient for (a) PE and (b) PAO vs. molecular weight. The values were plotted in the log scale in order to acquire the exponents. The transition point at $Z=178$ for PE is marked; no transition point was observed for PAO. 90
- Figure 4.7 Zero-shear rate viscosity vs. molecular weight. The diamond symbol is from experimental measurements [95]; the triangle and rectangular symbols are predictions from the structural-viscosity model, one set uses the X_c from the MD simulations (triangle), while the other uses the X_c from the original Berry and Fox model (square). 91
- Figure 4.8 Zero-shear rate viscosity vs. molecular weight with $a=3.4$. Experimental measurements are from commercially available data from ExxonMobil [98]. 92
- Figure 4.9 Comparison of zero-shear rate viscosity vs. molecular weight; the results from modeling were calculated with the modified a , fitted using two data points of KV40, and three data points of KV100 (circled in red), respectively. 93

Figure 5.1 Nd:YVO ₄ picosecond laser micro-machining system.	99
Figure 5.2 An image of a flat-bottom circular dimple acquired using a white-light interferometer.	100
Figure 5.3 Illustration of the laser scanning. Between each firing of the pulse, the focus of the laser moves d_s along the scanning direction; and moves d_r along the radial direction after completing a full circle.	100
Figure 5.4 Depth variation with respect to the distance from the focal location.	101
Figure 5.5 Effect of the overlap on the depth. O_r is the overlap along the radial direction, O_s is the overlap along the scanning direction.	102
Figure 5.6 Effect of overlap on the bottom surface roughness. O_r is the overlap along the radial direction, O_s is the overlap along the scanning direction.	103
Figure 5.7 CAD model of the collet fixture for mounting cylindrical parts.	104
Figure 5.8 Photos of the collet system.	105
Figure 5.9 Photos of the 3-jaw chuck system.	105
Figure 5.10 Positions for testing the translational focus variation.	106
Figure 5.11 Test points for the rotational focus variation.	106
Figure 5.12 Focus variation at different test points	107
Figure 5.13 Trajectory of the helix line. The lead, l , is the amount travel along the translational direction with a 360 degrees rotation.	108
Figure 5.14 Photo of the textured rectangular grooves along the helix (left) and the measured cross section of the texture using a white-light interferometer (right).	108
Figure 5.15 Example of titanium buildup on the drill margin and the cutting edge.	109
Figure 5.16 Candidate surfaces of a drill bit for texturing.	110
Figure 5.17 Texture design of a triangular distribution on the margin. A section of the margin is plotted, the rectangles are the location of the textures with dimensions L and W.	111

- Figure 5.18 Cross section of the texture design. A flat bottom shape is used.....111
- Figure 5.19 Estimate of the fluid pressure around the rectangular depressions.112
- Figure 5.20 Comparison of the drills: untreated, 10% of the margins micro-textured, and 20% of the margins micro-textured. Each rectangular depression is 50 μm wide, 450 μm long and 4 μm deep. Note that the tip of the margin, shown in the circle, was not textured.113
- Figure 5.21 Average texture depth of each laser textured drill bit.....113
- Figure 5.22 Tool life comparison for the untreated, 10%, and 20% textured area drills, respectively.115
- Figure 5.23 Images of the baseline drill #2 after (a) 0 holes drilled, (b) 30 holes drilled, and (c) 52 holes drilled (Images taken after the drilling of 10, 20, 40 and 52 holes are omitted here due to space concerns).116
- Figure 5.24 Baseline drills at failure (a) #1 after 30 holes drilled, (b) #2 after 52 holes drilled, and (c) #3 after 60 holes drilled.116
- Figure 5.25 10% textured drills at failure (a) #1 after 45 holes drilled, (b) #2 after 60 holes drilled, and (c) #3 after 60 holes drilled. Circles indicate the tips of the drill bit margin where no textures were made.116
- Figure 5.26 20% textured area at failure (a) #1 after 60 holes drilled, (b) #2 after 30 holes drilled, and (c) #3 after 60 holes drilled. Circles indicate the tips of the drill bit margin where no textures were made.117
- Figure 6.1 A schematic of a nominally flat-flat interface with a single texture. The textured (bottom) surface is fixed while the top surface is sliding with velocity U 122
- Figure 6.2 Distribution of the textured features. Square indicates the basic cell and the calculation domain for each dimple; circle indicates the dimple. N_1 is the number of dimples along the perpendicular direction, and N_2 is the number of dimples along the flow direction. 124
- Figure 6.3 Three different boundary condition treatments corresponding to (a) B.C.1: periodic in the flow direction, prescribed in the perpendicular direction, (b) B.C.2: prescribed in both the directions, and (c) B.C.3: prescribed in the flow direction, periodic in the perpendicular direction. 124

- Figure 6.4 Parameters for single texture design for the elliptical (ellip) and rectangular (rect) dimples. A is the width along the flow direction, and B is the width along the perpendicular direction, respectively. 125
- Figure 6.5 Cross sections studied for a single texture design, which are flat-bottom (flat), arc (cos), triangular center (triC), triangular left (triL), and triangular right (triR), respectively, from left to right..... 126
- Figure 6.6 Effect of B/L on P_{avg} for elliptical, flat-bottom dimple with $A/L=0.6$, depth= $3\ \mu\text{m}$ (circle), rectangular, flat-bottom dimple with $A/L=0.6$, depth= $2\ \mu\text{m}$ (diamond), rectangular, flat-bottom dimple with $A/L=0.2$, depth= $2\ \mu\text{m}$ (square), rectangular, arc-bottom dimple with $A/L=0.2$, depth= $2\ \mu\text{m}$ (triangle). 127
- Figure 6.7 Effect of depth $D=d/H_{ref}$ on pressure $P=P_{avg}/p_0$ for various geometries. $B/L=0.9$. The symbols are from the simulations, and the curves are from the fitted Equation 6.3a. The flat-bottom elliptical dimple generated the highest pressure. 128
- Figure 6.8 Effect of $D=d/H_{ref}$ on pressure $P=P_{avg}/p_0$ for different values of A/L of the flat-bottom elliptical dimple. $B/L=0.9$. The symbols are from the simulation, and the curve are from fitted Equation 6.3a with a unique C_1 for each A/L . As C_1 is unique for each A/L , it can be written as a function of A/L , $F(A/L)$ 129
- Figure 6.9 Third order polynomial form for $F(A/L)$ vs. A/L for the flat-bottom elliptical dimple, $B/L=0.9$. The symbols are from the simulation, and the curve is fitted to a third order polynomial. 130
- Figure 6.10 Effect of A/L on P for the arc-bottom elliptical dimple and the flat-bottom rectangular dimple, respectively. $B/L=0.9$. The symbols are from the simulation, and the curves are fitted to a third order polynomial. 130
- Figure 6.11 Maximum P for various dimple geometries, $B/L=0.9$. The flat-bottom elliptical dimple generated the highest pressure. 131
- Figure 6.12 Effect of $D=d/H_{ref}$ on pressure $P=P_{avg}/p_0$ at three relative speeds. $B/L=0.9$. The symbols are from the simulation, and the curves are from the fitted Equation 6.4. . 133
- Figure 6.13 Effect of A/L on $P=P_{avg}/p_0$ for various speeds at an appropriate D . $B/L=0.9$. The symbols are from the simulation, and the curves are from the fitted Equation 6.4. . 133

- Figure 6.14 Size effect of A/L for multiple dimples with an increasing N_2 . $N_1=1$, $B/L=0.9$. The symbols are from the simulation, and the curves are from the fitted third-order polynomial. 135
- Figure 6.15 Size effect of A/L for multiple dimples with an increasing N_1 . $N_2=1$, $B/L=0.9$. The symbols are from the simulation, and the curves are from the fitted third-order polynomial. 135
- Figure 6.16 Effect of N_2/N_1 on the optimal A/L . $B/L=0.9$. At different N_2/N_1 ratio, the optimal A/L value changes. For $N_2/N_1 < \lambda \approx 0.4$, the textures always generate a negative effect. 136
- Figure 6.17 Combined effect of the surface texture and surface roughness on P_{avg} for the flat-bottom elliptical dimple with $D=1.5$, $A/L=0.8$, $B/L=0.9$ 138
- Figure 6.18 Pressure distributions for the cases with different texture top geometries. The elliptical dimple showed smaller cavitation region and a higher pressure build-up. 140
- Figure 6.19 Pressure distribution over the textures with the same top geometry but different texture sizes A/L . Larger texture size generated a larger cavitation region with a higher pressure build-up. A balance between the cavitation region and the pressure build-up is necessary for optimization. 140
- Figure 6.20 Pressure distributions for textures of different cross sections. Compared with the arc-bottom dimple (described with a cosine function), the flat-bottom dimples generated a higher pressure build-up, whereas the cavitation regions are similar.... 141

List of Tables

Table 2.1 Parameters for the Lennard-Jones Potential.....	41
Table 2.2 Parameters for the intramolecular interactions	42
Table 2.3 Comparisons of α_0 and α^* between the experimental data [49] and the calculated MD data.....	53
Table 3.1 NEMD simulation conditions for three molecules at different pressures and temperatures. Three different states of squalane, six different states of PAO 4, and four different states of OCP were calculated	65

Chapter 1 Introduction

1.1 Research Background

Friction and wear of components have a significant impact on the environment and economy in terms of the fuel consumption and replacement costs. As mentioned in the 1966 Jost report [1], economic losses that could be ascribed to wear and friction were equivalent to approximately 4% of the United Kingdom's gross national. In passenger cars, one-third of the fuel energy is used for overcoming friction in the engine, transmission, tires, and brakes [2]. In recent decades, the reduction of friction due to rubbing and wear of contacting surfaces has become increasingly important as industries strive to improve the energy efficiency in the manufacturing processes and machine operations.

Figure 1.1 shows a typical Stribeck curve which was first proposed by Richard Stribeck in 1901 and 1902 [3,4]. The Stribeck curve has been widely used as a guideline for categorizing lubrication regimes for the experimental and numerical study of lubricated contacts [5-7]. Lubrication regimes can be divided into boundary lubrication (BL), mixed lubrication (ML), elastohydrodynamic lubrication (EHL) and hydrodynamic lubrication (HL), based on the lubrication parameter : $\eta V/P$, where η is the fluid viscosity, V is the relative speed of the surface,

and P is the load. In the boundary lubrication and mixed lubrication regimes, the interactions between the contacting asperities contribute significantly to the frictional forces and wear at the interfaces. In the hydrodynamic and elastohydrodynamic lubrication regimes, the fluid completely separates the mating surfaces; therefore, the rheological properties of the lubricant play a significant role in determining the friction coefficient. Additionally, in the hydrodynamic lubrication regime, the friction coefficient gradually increases owing to the viscous drag of the fluid, leading to additional energy loss.

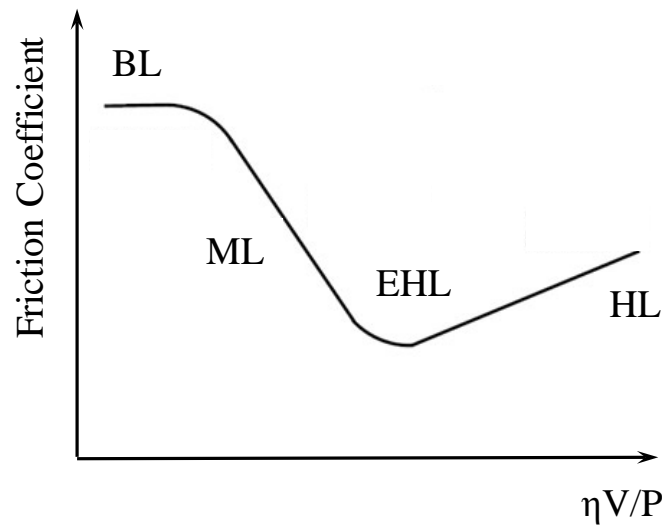


Figure 1.1 Schematic of the Stribeck curve. Based on the lubrication parameter: $\eta V/P$, lubrication regimes can be divided into boundary lubrication (BL), mixed lubrication (ML), elastohydrodynamic lubrication (EHL) and hydrodynamic lubrication (HL) regimes.

1.2 Research Methodology

The goal of our research is to improve the tribological behaviors of lubricated interfaces which are considerably affected by the properties of the mating surfaces and the rheological

properties of the lubricant between them. Therefore, attempts to reduce the friction and wear of a complex system would require methods for tackling one or both of these categories, either by improving on the mating surfaces or by advancing the lubricant. In this work, both the categories are researched through two different approaches, as given below:

1. Modeling of the rheological properties of hydrocarbon lubricants based on their molecular structures, for the characterization and development of the lubricants, in the elastohydrodynamic lubrication and hydrodynamic lubrication regimes.

As the performance of EHL and HL significantly depends on the rheological properties of the lubricant, the rheological modeling of the lubricant is performed by combining the available empirical-theoretical models with molecular dynamics simulations. The rheological properties of the lubricant are determined by the selection of the base oil and the viscosity modifiers (VMs). The base oil is usually composed of low molecular weight structures, whereas the VM consists of high molecular weight polymer chains. Molecular dynamics simulations enable us to predict the rheological behaviors of lubricants based on their molecular structures. Simulation methods were developed for the calculations of the pressure-viscosity coefficient and the critical shear rate, which are crucial parameters for determining the film generation, at different loads and speeds. Combined with the existing empirical-theoretical models, the viscosities of high molecular weight polymer chains are predicted based on the calculations of the related structural parameters. The development of a modeling tool for predicting the rheological performance of

the lubricant based on molecular structure, pressure, temperature, and operating shear rate is attempted.

2. Investigation of the effect of the surface texture, for tribological performance improvements on the interacting surfaces, in the boundary and mixed lubrication regimes.

In the boundary lubrication regime, experiments were performed for demonstrating the surface texture effect of adhesion reduction by drilling of the metal material. A high precision manufacturing process was developed. Adequately designed surface textures were applied on the drill bits for adhesion reduction and tool life improvements. Drilling tests were performed and compared with the non-textured samples. For investigation of the surface texturing effect on film generation, a flat-flat model is developed for understanding the increase in the load capacity owing to the surface textures. Increased separation will lead to the reduction of friction coefficient as the magnitude of asperity contact is reduced. A wide range of texture geometry was studied, and the geometric parameters were optimized depending on the boundary conditions. Empirical equations were established based on the simulated results and can be used as guidelines for surface texture design of various applications.

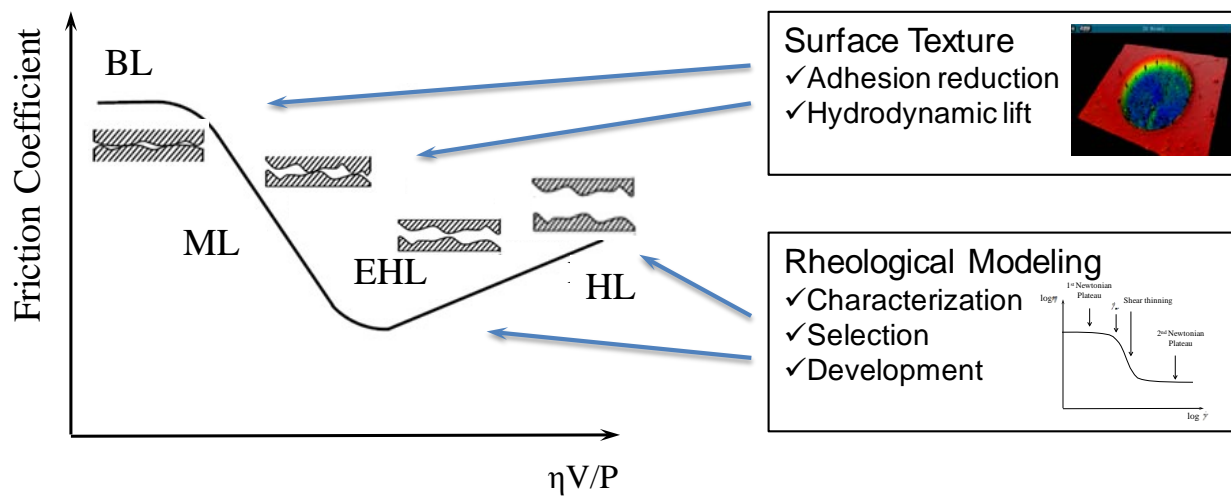


Figure 1.2 Proposed approaches for improving the tribological behaviors of lubricating interfaces in different lubrication regimes.

Chapter 2 Pressure-Viscosity Coefficient Calculations for Hydrocarbon Base Oil

The pressure-viscosity coefficient (the α value), which represents the variation in the viscosity as a function of pressure, is an important parameter for elastohydrodynamic lubrication (EHL) analyses. The properties of hydrocarbons in the C₂₀-C₄₀ mass ranges are of fundamental importance because they are the basic constituents of synthetic- and mineral-based lubricant stocks. The conventional acquisition of the α value requires the preparation of lubricant samples and experimental testing using a high-pressure viscometer. In this chapter, we present a method to obtain the α value of a typical base oil (1-Decene trimer) based solely on molecular dynamics (MD) simulations. Non-equilibrium molecular dynamics (NEMD) simulations were performed for calculating the shear viscosity of the lubricant at various temperatures (ranging from 313-750 K) and pressures (up to 1 GPa). Elevated temperatures and time-temperature superposition (TTS)-based extrapolations were applied to further extend the ability of the NEMD simulations, and the rotational relaxation time was calculated and utilized for determining the validity of the NEMD calculations. The α value at 100 °C was calculated and compared with the experimental results. The effectiveness of the extrapolation was evaluated with a 95% confidence interval.

2.1 Introduction

The rheological properties of a lubricant are determined by the molecular structures of its base oil and additives. The properties of alkanes in the C₂₀-C₄₀ mass range are of fundamental importance because they are the key constituents of the base stocks of synthetic and mineral lubricants. In elastohydrodynamic lubrication (EHL), the pressure-viscosity coefficient, the α value, which has been used to characterize the pressure dependence of the shear viscosity, is critical for evaluating the lubricant film thickness at the contact interface under a high pressure in the mega- and giga-pascal ranges, where the viscosity properties change significantly from those at the ambient conditions. Therefore, an accurate evaluation of the shear viscosity at such a high pressure is of great importance.

The most commonly used definition of the α value comes from the exponential viscosity-pressure relationship [8] shown below:

$$\eta(T, P) = \eta(T, 0)e^{\alpha(T)P} \quad (2.1)$$

where $\eta(T, P)$ is the viscosity at the pressure P and temperatures T . $\eta(T, 0)$ represents the viscosity value at the atmospheric pressure and temperature T . In practice, the ambient pressure-viscosity coefficient,

$$\alpha_0 = \left. \frac{1}{\eta} \frac{\partial \eta}{\partial P} \right|_{P=0} \quad (2.1a)$$

and the reciprocal asymptotic isoviscous pressure,

$$\alpha^* = \left[\int_0^\infty \frac{\eta_0 dP}{\eta(P)} \right]^{-1}, \quad (2.1b)$$

which is a generalized pressure-viscosity coefficient, are often obtained by a piecewise integration of the test data points [9].

The Walther equation has been widely used to characterize the viscosity relationship with the temperature [10,11], and is the basis for the ASTM viscosity-temperature charts, shown below:

$$\log \log(\nu + c_W) = a_W - b_W \log T, \quad (2.2)$$

where ν is the kinematic viscosity and T the temperature in Kelvin, a_W and b_W are lubricant-specific parameters, and c_W is a constant, which is approximately 0.7.

The Vogel-Fulcher-Tammann-Hesse (VFTH) equation [12-14],

$$\log_e(\eta) = A_{VFTH} + \frac{B_{VFTH}}{T - T_0} \quad (2.3)$$

where η is the dynamic viscosity, and A_{VFTH} , B_{VFTH} and T_0 are lubricant-specific parameters, was also used over a wide viscosity range for several liquids, and is considered more accurate [15]. However, its non-linear nature and the three fluid specific coefficients render it more difficult for generalization [10].

Currently, most α -value evaluations are being performed by means of experiments. Viscometers and rheogoniometers are often used for viscosity measurements at atmospheric conditions. The development of new viscometers has enabled valuable high-pressure viscosity measurements at 1 GPa or higher [16-18]. EHL film measurements combined with the Hamrock-Dowson equation [19,20] have been utilized for determining the pressure-viscosity

coefficient. α value acquisitions have also been performed using empirical correlations with the relevant material properties [21,22].

However, preparations and measurements of the lubricant samples can be expensive and difficult, particularly, for viscosity measurements at high pressures and high shear rates. Moreover, lubricant samples, even the "pure" base oils, are often mixtures of several constituents with different molecular chains, for which the measured results are generally the resultant responses from all the major constituents. The effect and influence of each component on the lubricant properties can hardly be decoupled and determined by test only.

The implementation of molecular dynamics (MD) simulations for the viscosity evaluation of alkanes has gained momentum since the 1990s, benefited by the increase in the computational power and development of various advanced numerical models [23-27]. Equilibrium molecular dynamics (EMD) and Non-equilibrium molecular dynamics (NEMD) [28] simulations are widely used for this purpose. NEMD simulations of the steady shear flow, in particular, can be directly used for shear viscosity calculations.

The rheological properties of a wide range of alkanes have been studied through molecular dynamic simulations, with the strain-rate dependent viscosities a major focus of the studies. Morriss et al. [29] examined the rheology of n-decane and n-eicosane. Cui et al. [30,31] demonstrated the NEMD results for n-decane, n-hexadecane, n-tetracosane, 10-n-hexylnonadecane, and squalane. Khare et al. [32] studied n-docosane, n-octacosane, and

5,12-dipropylhexadecane. In these studies, a Newtonian plateau was observed at low shear rates; at high shear rates, the alkanes demonstrate shear thinning behavior over several magnitudes of the strain rate. The influences of the branches of the isomers on the viscosity values have also been of interest. Kioupis and Maginn [33] compared the rheological properties of the three isomers of C_{18} . Moore et al. [34] examined the rheological behavior of the isomers of C_{30} and reached the C_{20} - C_{40} range for base oils. Both studies showed that widely spaced long branches would have better temperature performances than those with closely packed short branches. Jabbarzadeh et al. [35] studied the rheological properties of a number of molecular configurations of C_{100} . Though the calculations were only in the non-Newtonian domain owing to the limitation of the NEMD simulations, they further demonstrated that the effective length of the molecule and its degree of branching ultimately dictate the shear response. Attempts to use MD simulations for acquiring the temperature-viscosity and pressure-viscosity coefficients have also been reported. Predictions of the viscosity index (VI) or the viscosity number (VN) of squalane [36], n-octadecane [33], and 9-octyldocosane [34] have all been reported. Pressure-viscosity coefficients have been calculated through EMD [37] and NEMD [38,39], with the latter approach being more successful than the former. Results from pressure- and temperature-dependent viscosity studies have shown that while the applied MD models underpredict the actual Newtonian viscosity, they can determine the temperature or pressure dependence of the viscosity with a reasonable accuracy.

Viscosity evaluation with MD simulations faces several major challenges. First of all, the inaccuracy in the Newtonian regime because the force field were not specifically acquired for such transport properties. Furthermore, due to low signal-to-noise ratio, in NEMD simulations, the minimum achievable shear rate is usually around 10^8 s^{-1} at ambient temperature and pressure [30], which is higher than what appears in most current engineering applications. More importantly, a lubricant may experience temporary shear thinning at sufficiently high shear rates, in which the shear stress induces molecular alignment and lowers the effective viscosity [40]. Figure 2.1 shows the change in the shear viscosity with an increasing shear rate for a typical lubricant. In the low shear rate region, the shear stress in the fluid increases linearly with the shear rate, depicted as the 1st Newtonian plateau. The transition from the Newtonian to a non-Newtonian regime takes place at the critical shear rate, $\dot{\gamma}_{cr}$, corresponding to the onset of the shear thinning behavior. As the shear rate increases further, the effective viscosity decreases until the 2nd Newtonian plateau is reached. In order to capture the 1st Newtonian plateau, the shear rate applied in the NEMD simulations must be lower than the critical shear rate. For alkane fluids, studies have shown that the critical shear rate is approximately the reciprocal of the rotational relaxation time [31]. For molecules of a larger carbon number or for lubricants at low temperatures and/or high pressure, the systems demonstrate “slow” dynamics or long relaxation times [41], rendering it even more difficult to calculate the 1st Newtonian plateau at high pressures.

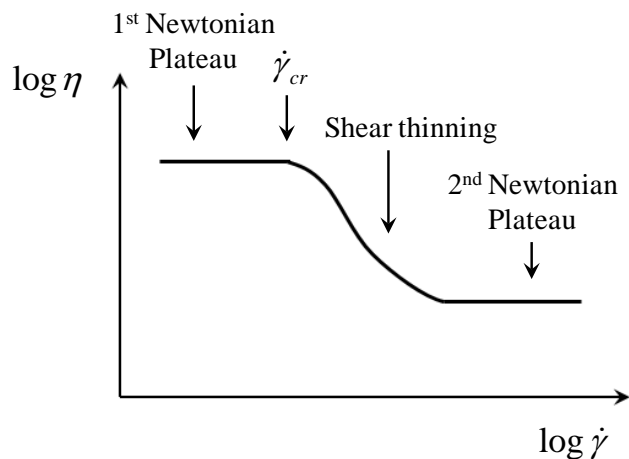


Figure 2.1 Typical change in the shear viscosity with an increasing shear rate.

Considerable efforts have been made to overcome this difficulty. Gordon attempted to predict the viscosity of heavier molecules based on the Stokes-Einstein relationship [42]. Pan and McCabe [43] applied the Transient Time Correlation Function (TTCF) formalism [44,45] to calculate the viscosity of n-decane. Their results demonstrated that the TTCF method agreed well with the NEMD simulations for viscosity calculations, and the shear rate could attain a value as low as 10^4 s^{-1} . Bair et al. [46] applied the concept of time-temperature superposition successfully and compared the NEMD simulation results with experimental viscosity data for squalane. A mastercurve for the shear-rate dependent viscosity was acquired based on the experimental and MD results since it was difficult to calculate low-shear viscosities at the ambient temperature and high pressure directly from the MD simulations.

1-Decene trimer is a major component of poly- α -olefin (PAO) 4cSt, or PAO 4, an important fluid in the current synthetic base oil market. Its molecular structure, shown in Figure

2.2, may also be considered as a representative structure for all the branched alkanes in the C_{20} - C_{40} range. Understanding the lubrication properties of the 1-Decene trimer requires the knowledge of its pressure-viscosity coefficient. The research reported in this chapter is aimed at acquiring the α value of the 1-Decene trimer based solely on the MD simulations. The concept of time-temperature superposition (TTS) is used to further extend the pressure range in which the viscosity can be evaluated.

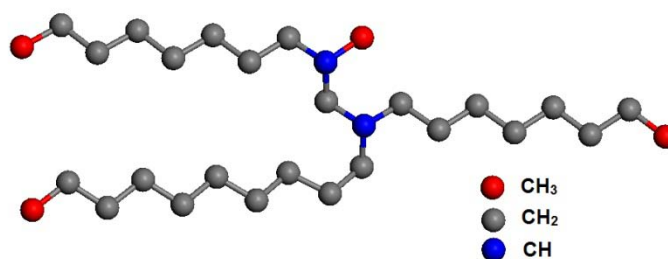


Figure 2.2 Molecular structure of the 1-Decene trimer.

2.2 Model Description

The acquisition of the pressure-viscosity coefficient for the 1-Decene trimer requires the shear viscosity values for a range of pressures and the assurance that the 1st Newtonian plateau can be successfully captured through NEMD simulations, i.e., the applied NEMD shear rate should be lower than the critical shear rate. To ensure this, the applicable NEMD shear rate is compared to the reciprocal of the rotational relaxation time. The rotational relaxation time, τ , is

calculated through the integration of the reorientation autocorrelation function [47] as shown below:

$$\tau = \int_0^{\infty} C^1(t) dt = \int_0^{\infty} \langle (\mathbf{e}_1(t) \cdot \mathbf{e}_1(0)) \rangle dt, \quad (2.4)$$

where $C^1(t)$ is the reorientation autocorrelation function. For branched hydrocarbons, $\mathbf{e}_1(t)$ and $\mathbf{e}_1(0)$ are the unit vectors representing the longest principal axis of the molecule ellipsoid of inertia at a time interval t and at the initial point, respectively. The principle axes were determined from the eigenvectors of the symmetric inertia tensors of the molecule as an eigenvalue problem.

The modified Kohlrausch-Williams-Watts (mKWW) function [48], shown below, was applied for the regression of the reorientation autocorrelation function owing to the low signal to noise ratio of the autocorrelation function at large time intervals.

$$P_{\text{mKWW}}(t) = \chi e^{-\frac{t}{\tau_0}} + (1 - \chi) e^{-\left(\frac{t}{\tau_{\text{KWW}}}\right)^\beta}, \quad (2.5)$$

where τ_0 and τ_{KWW} are the two characteristic times of the mKWW function. The first term, $e^{-\frac{t}{\tau_0}}$, characterizes the initial exponential decay of the molecule orientation correlations, and $e^{-\left(\frac{t}{\tau_{\text{KWW}}}\right)^\beta}$ describes the stretched exponential decay contributions, χ and $(1 - \chi)$ are used to weigh the two contributions, and β illustrates the width of the stretched exponential decay.

The rotational relaxation time is then calculated by the integration of the mKWW function:

$$\tau = \int_0^{\infty} P_{\text{mKWW}}(t) dt = \chi \tau_0 + (1 - \chi) \tau_{\text{KWW}} \frac{1}{\beta} \Gamma\left(\frac{1}{\beta}\right) \approx \int_0^{\infty} C^1(t) dt. \quad (2.6)$$

Here Γ is the gamma function.

Therefore, at low pressures, NEMD simulations should be performed at the targeted temperature of interest because they can directly capture the 1st Newtonian plateau and obtain the low-shear viscosity values. To acquire high-pressure viscosity data at the temperatures of practical interest, where direct NEMD simulations can hardly capture the 1st Newtonian plateau, the NEMD simulations will be first performed to calculate the viscosities at elevated temperatures and then the viscosities are extrapolated to the temperature of interest using the temperature-viscosity relationship (Equation 2.2). At an elevated temperature, the relaxation time is shorter; therefore, the critical shear rate should be higher [39], allowing the capture of the 1st Newtonian plateau. The magnitude of the required temperature increase is determined based on the calculation of the reciprocal of the rotational relaxation time corresponding to the critical shear rate. The flow chart for the numerical approach is given in Figure 2.3. To evaluate the effectiveness of the viscosity extrapolation using the high temperature data, viscosities at the temperature of interest were calculated with 95% confidence intervals using the NLPARCI function in MATLAB based on the elevated temperature results. The computational results were then compared with the experimental results by Bair [49].

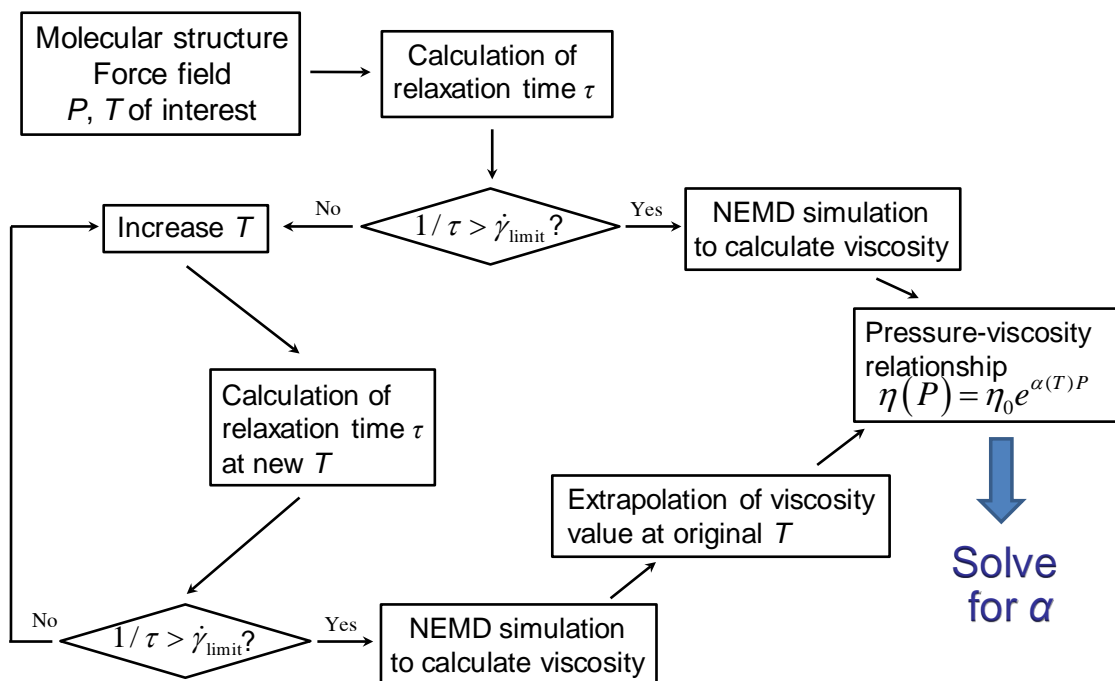


Figure 2.3 Flow chart for calculation of the α value of alkanes.

2.3 Molecular Dynamics Simulation Details for 1-Decene Trimer

The united atom (UA) method was used for generating the 1-Decene trimer. CH_3 , CH_2 and CH were each considered as pseudoatoms within the hydrocarbon chain with the interaction center at the nucleus of each carbon atom. The temperature of interest in the current study is $100\text{ }^\circ\text{C}$.

The force field used to describe the alkane molecules is similar to the one used by McCabe et al. [39]. This force field was proposed by Siepmann et al. [50], and later extended to branched alkanes by Mondello and Grest [23]. Although it underestimated the absolute viscosity values in general, the calculated α value of 9-octylheptadecane was in an excellent agreement

with the experimental measurements. Moreover, the fixed bond length was replaced by a stiff harmonic potential to generate a fully flexible bond [51].

Nonbonded interactions are described using a pairwise Lennard Jones (LJ) potential [52],

$$V_{LJ}(r) = 4\varepsilon_{ij} \left[\left(\frac{\sigma_{ij}}{r} \right)^{12} - \left(\frac{\sigma_{ij}}{r} \right)^6 \right] \quad (2.7)$$

where ε_{ij} is the depth of the potential well, r the distance between the particles, and σ_{ij} the LJ size. The LJ parameters for interaction between like pseudoatoms are listed in Table 2.1. LJ parameters for unlike interactions are computed using the standard Lorentz-Berthelot combining rules, shown below.

$$\begin{aligned} \sigma_{ij} &= \frac{\sigma_{ii} + \sigma_{jj}}{2} \\ \varepsilon_{ij} &= \sqrt{\varepsilon_{ii}\varepsilon_{jj}} \end{aligned} \quad (2.8)$$

The cutoff distance was set at 11.5 Å.

Table 2.1 Parameters for the Lennard-Jones Potential

Group	ε (Kcal/mol)	σ (Å)
CH ₃	0.227	3.93
CH ₂	0.093	3.93
CH	0.08	3.81

Bond-stretching and bond-bending interactions are described by harmonic potentials, as shown below:

$$V_{str}(l) = \frac{1}{2} k_{str} (l - l_{eq})^2 \quad (2.9)$$

$$V_{ben}(\theta) = \frac{1}{2} k_{ben} (\theta - \theta_{eq})^2 \quad (2.10)$$

where k_{str} and k_{ben} are the force constants, and l_{eq} and θ_{eq} are the equilibrium distance and angle, respectively.

The torsional interaction is described by the model proposed by Jorgensen et al. [53]

$$V_{tor}(\phi) = \sum_{m=0}^3 a_m (\cos \phi)^m, \quad (2.11)$$

where a_m are the parametric constants. Parameters for intramolecular interactions can be found in Table 2.2.

Table 2.2 Parameters for the intramolecular interactions

	Value	Unit
k_{str}	901.24	Kcal/(mol Å ²)
l_{eq}	1.54	Å
k_{ben}	124.28	Kcal/(mol rad ²)
θ_{eq}	114	Degree
a_0	2.007	Kcal/mol
a_1	4.012	Kcal/mol
a_2	0.271	Kcal/mol
a_3	-6.290	Kcal/mol

a_0 (X-CH ₂ -CH-Y)	0.814	Kcal/mol
a_1	1.792	Kcal/mol
a_2	0.389	Kcal/mol
a_3	-3.673	Kcal/mol

Eighty (80) molecules were generated in the system. The system was first created and relaxed in the Materials Studios software to acquire the initial distribution of the pseudoatoms. The Large-scale Atomic/Molecular Massively Parallel Simulator (LAMMPS) software [54,55] was used for the MD simulations, and a timestep of 1 fs was applied in the simulations. A further equilibrium for 10 ns at the assigned temperature and pressure in the MD simulations was performed to acquire the equilibrium configuration. This equilibrium configuration provides the initial state for the NEMD simulations. Then, the alkanes were allowed to undergo a planar Couette flow using the SLLOD equations of motion [28], which are usually written in the form of two first-order differential equations:

$$\dot{\mathbf{r}}_i = \frac{\mathbf{p}_i}{m_i} + \mathbf{r}_i \cdot \nabla \mathbf{u}, \quad \dot{\mathbf{p}}_i = \mathbf{F}_i^\Phi + \mathbf{p}_i \cdot \nabla \mathbf{u}, \quad (2.12)$$

where m_i , \mathbf{r}_i , and \mathbf{p}_i represent the mass, position, and thermal momentum, respectively, of particle i , \mathbf{F}_i^Φ represents the total force due to intermolecular potentials of all particles on particle i , and $\nabla \mathbf{u}$ represents the velocity gradient tensor. The Lees-Edwards periodic boundary conditions [56], which are an adaptation of the standard periodic boundary conditions for MD

simulations of a shear flow, were applied. A Nosé/Hoover thermostat was coupled to achieve the energy conservation of the system, as proposed by Tuckerman et al. [57]. The measured resulting shear stress divided by the imposed strain is the value of the shear viscosity.

2.4 Simulation Results

2.4.1 Validations of the Kinematic Viscosity and Density

The kinematic viscosities of the 1-Decene trimer at various temperatures under the pressure of 0.1 MPa are shown in Figure 2.4. Based on extrapolation using the temperature-viscosity relationship, the kinematic viscosities for 1-Decene trimer at $T=40\text{ }^{\circ}\text{C}$ and $100\text{ }^{\circ}\text{C}$ are 6.7 cSt and 1.53 cSt, respectively, after curvefitting the calculated data. The corresponding experimental data at $40\text{ }^{\circ}\text{C}$ and $100\text{ }^{\circ}\text{C}$ are 16.25 cSt and 3.74 cSt, respectively. An underprediction by a factor of 2.43-2.44 in absolute value was found; however, the prediction of the slope itself is accurate. Calculated densities with respect to temperature at 0.1 MPa are plotted in Figure 2.5. Densities of 0.8 g/cm^3 and 0.76 g/cm^3 were used based on the MD calculations of the 1-Decene trimer at 0.1 MPa and temperatures of $40\text{ }^{\circ}\text{C}$ and $100\text{ }^{\circ}\text{C}$, respectively. Although PAO 4 also contains a certain amount of 1-Decene dimer and tetramer, a simple comparison between the calculated density and a commercially available MSDS data sheet for PAO4cSt [58] can be made. The density at $15.6\text{ }^{\circ}\text{C}$ was reported to be 0.82 g/cm^3 , comparable with the 0.819 g/cm^3 predicted from the current MD simulations. The boiling point

was reported to be 687 K in the MSDS, well within the range of 673-698 K from the current MD simulations, where a significant change in the density was observed.

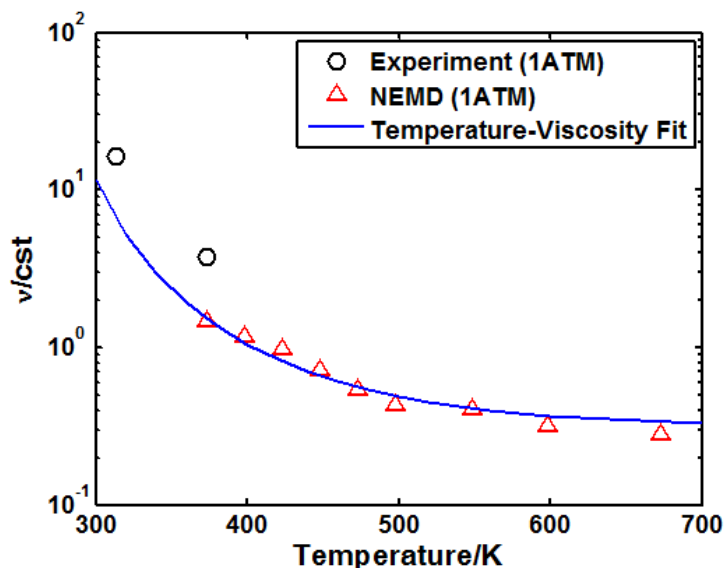


Figure 2.4 Kinematic viscosity of 1-Decene trimer vs. the temperature at 0.1 MPa pressure. The dynamic viscosity is fitted to Equation 2.2, and then converted into kinematic viscosity using the calculated density.

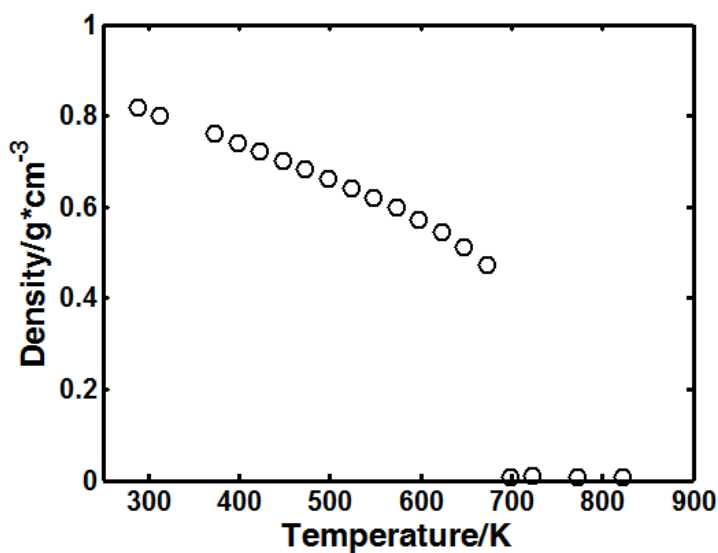


Figure 2.5 Calculated density of 1-Decene trimer vs. temperature at 0.1 MPa pressure. A clear transition can be observed around 680 K, suggesting a change from liquid state to gas state.

2.4.2 Evaluations of the Relaxation Time

The relaxation times were calculated for various pressures at 100 °C to determine a suitable pressure at which the transition from the direct NEMD to an NEMD committed at elevated temperatures can occur. Figure 2.6 illustrates the mKWW function (Equation 2.5) fit for the calculated autocorrelation function at 400 MPa. Based on the fitted parameters, the relaxation time was determined to be 5.2 ns using Equation 2.6. As aforementioned, the signal-to-noise ratio of the autocorrelation function deteriorates for large time intervals, and the parameters were adjusted to best fit the initial portion of the curve. A suitable transition point for the direct NEMD and the NEMD approaches at elevated temperatures was determined to be 400 MPa, where the critical shear rate is estimated at approximately $2 \times 10^8 \text{ s}^{-1}$, which is higher than the minimum applicable NEMD shear limit of 10^8 s^{-1} for ensuring the capture of the 1st Newtonian plateau.

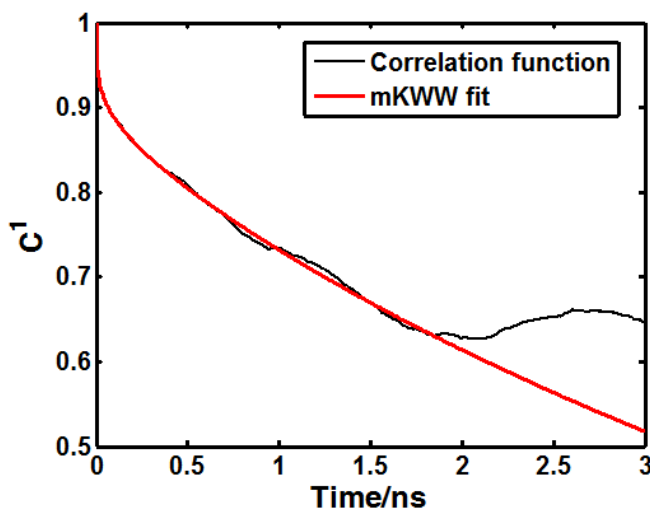


Figure 2.6 mKWW fit of the reorientation autocorrelation function of the longest principal axis of the molecule ellipsoid of inertia at 400 MPa, 100 °C, fitted to Equation 2.5, to acquire the relaxation time.

2.4.3 Viscosity Calculations at Low and High Pressures

Figure 2.7 demonstrates the viscosity results with respect to the total calculation time at various pressures at $T=100$ °C. A shear rate of 2×10^8 s^{-1} was applied to the simulations at pressures of 0.1 MPa, 100 MPa and 250 MPa; a shear rate of 10^8 s^{-1} was selected for the simulations at the pressure of 400 MPa. As the computation time increases, the viscosity gradually reaches a constant value, although data oscillations were still observed. For the cases with a larger rotational relaxation time (or a higher pressure), convergence is more difficult to achieve. Based on the observed oscillation of the viscosity data, the total calculation time to reach an equilibrium is recommended as 5-20 times the rotational relaxation time, which in turn would result in 50-200 ns if the critical shear rate is at the NEMD limit of 10^8 s^{-1} . The total NEMD simulation time of 100 ns for each data point is therefore believed to be a suitable time period, and is used for further calculations. However, non-convergent solutions were still observed for certain cases, which may be owing to some improper molecular conformations at the starting point of the NEMD simulations.

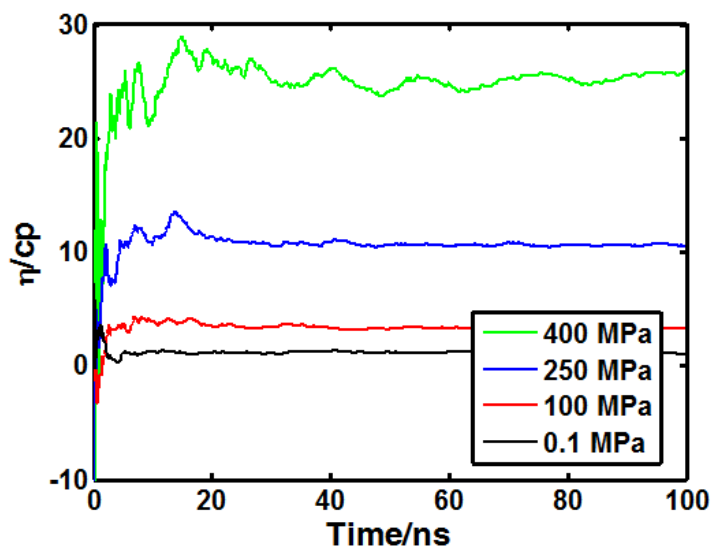


Figure 2.7 Calculated viscosities vs. the total calculation time at various pressures. The viscosity values stabilize within 100 ns.

The shear viscosities at 600 MPa and 175 °C at various shear rates were calculated and plotted in Figure 2.8. The critical shear rate was found to be $3.07 \times 10^8 \text{ s}^{-1}$ from the calculations of the reciprocal of the rotational relaxation time, as marked by the arrow, which agreed well with the calculated NEMD results for depicting the onset of the shear thinning behavior. At high strain rates, a shear thinning behavior was captured. At different shear rates lower than the critical shear rate, the viscosities were consistent, indicating that the current approach had indeed captured the 1st Newtonian plateau of the lubricant. Therefore, it is valid to consider the calculated viscosities at the shear rates below the critical shear rate as the low-shear viscosity at the targeted temperature and pressure.

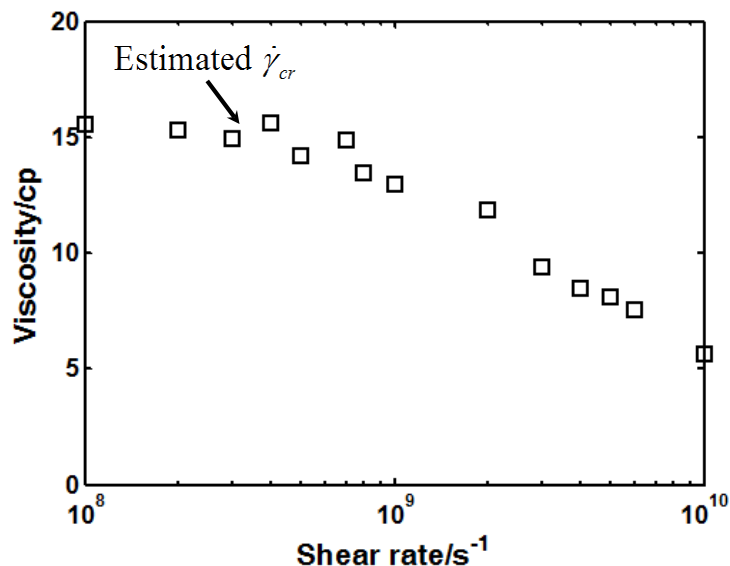


Figure 2.8 Calculated viscosities at different shear rates at 600 MPa, 175 °C. The arrow indicates the estimated critical shear rate calculated from the reciprocal of the rotational relaxation time.

Figures 2.9-2.11 demonstrate the extrapolation of the viscosities to lower temperature segments for high pressures of 600 MPa, 800 MPa, and 1 GPa, respectively. The constant c_w in Equation 2.2 is set to 0.7 in the current analyses. For higher pressures, a larger increase in temperature is required to capture the 1st Newtonian plateau with the NEMD simulations. Meanwhile, at higher temperatures, the applicable NEMD shear rate limit increases further as the signal-to-noise ratio further deteriorates. This in turn requires a significant temperature increase for the case of 1 GPa pressure, compared with those for the 600 MPa or 800 MPa cases. Different initial configurations were used for each individual simulation. Different shear rates that were less than the critical shear rate were used for each case to further validate the capture of the 1st Newtonian plateau. The values were first given in a semi-log plot and then rescaled to the

double-log plot. For all three cases, the absolute viscosities were lower than the experimental data as expected; however, they demonstrated a good trend even for a temperature as low as 40°C. 95% confidence limits were calculated based on the available data points to ensure the effectiveness of extrapolations. The author also examined extrapolations using the VFTH equation (Equation 2.3). However, owing to the non-linear nature of this equation, the 95% confidence limit would suggest a value range of two or three magnitudes, diminishing the significance of the extrapolation.

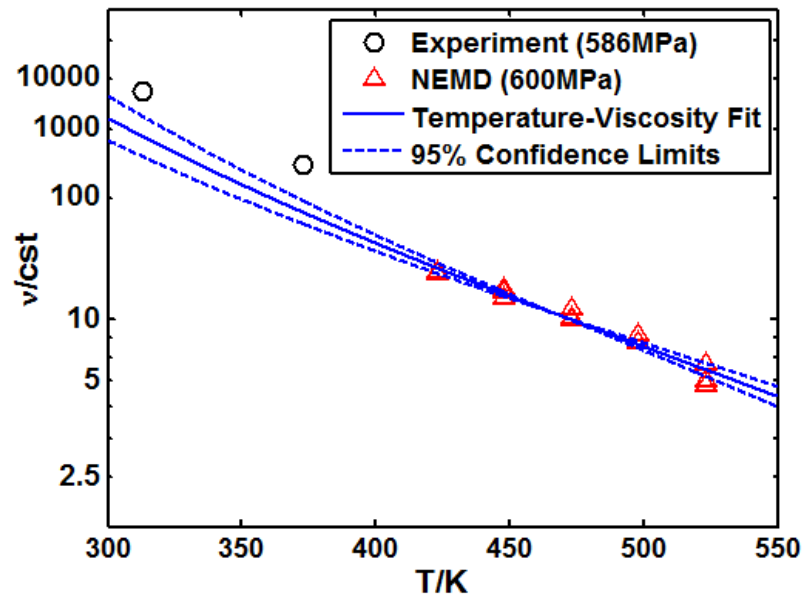


Figure 2.9 Viscosities calculated and extrapolated for 600 MPa.

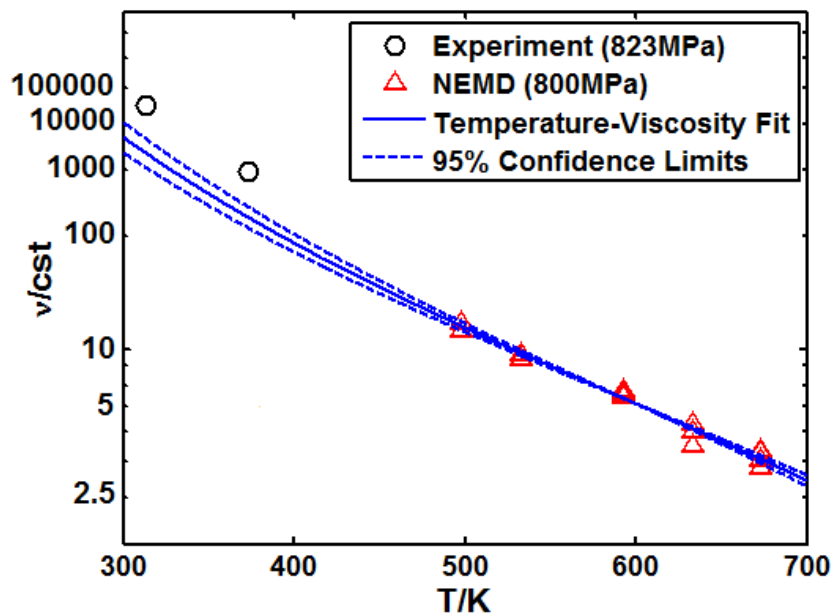


Figure 2.10 Viscosities calculated and extrapolated for 800 MPa.

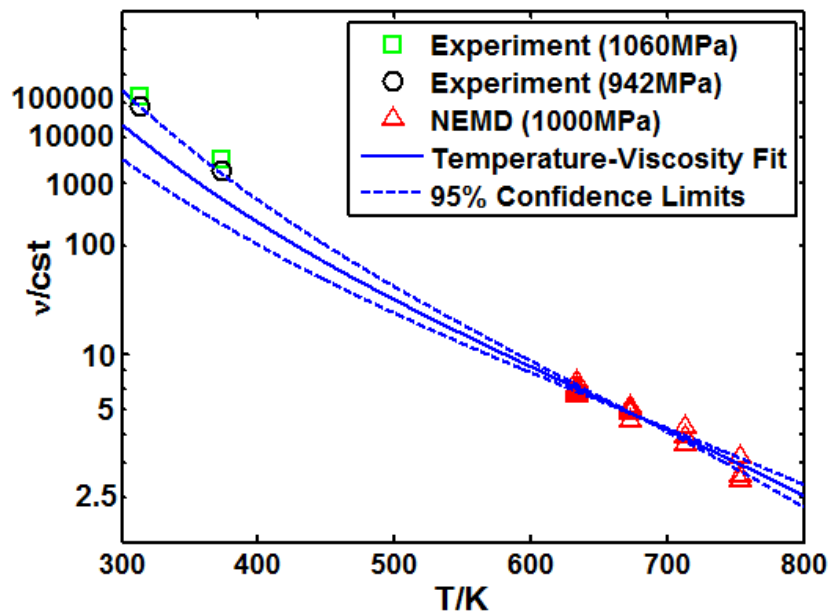


Figure 2.11 Viscosities calculated and extrapolated for 1 GPa.

2.4.4 Comparisons of the α Value with the Experimental Data

The experimental results [49] and MD simulation results of the pressure-viscosity relationship are plotted together in Figure 2.12. The error bars for the first seven data points (from the direct NEMD) were smaller than the marker size. The error bar values for the last three data points (from the extrapolations of the NEMD calculations at elevated temperatures) were obtained from the upper and lower limits of the 95% confidence intervals. As expected, the standard deviation of the viscosity increased with pressure owing to the extrapolations from higher temperatures. The variation in the viscosity extrapolated from the 1 GPa pressure is significantly larger than that from the 600 MPa and 800 MPa cases, indicating that calculations for even higher pressures are not recommended with the current modeling system. While the absolute value in terms of the viscosity variation at each temperature was found to be approximately the same, this would imply a larger variation, in percentage, for higher temperature cases since viscosity decreases with increasing temperature. For higher pressure cases, more data points are required to obtain a trustworthy confidence level. Comparisons between the calculated α_0 and α^* with the experimental data [49] are shown in Table 2.3. It should be mentioned that the impurities in the samples used in the experiments may also contribute to the difference. Nevertheless, the α values demonstrate a good agreement between the measurements and the NEMD simulations. Densities of the 1-Decene trimer under 600 MPa, 800 MPa and 1 GPa and at 100 °C calculated from the MD simulations are 0.965, 0.996, and

1.021 g/cm³, respectively. Figure 2.13 shows the viscosity comparison after normalizing the viscosity values by that at 0.1 MPa (η_0), so that the two curves would share the same initial value at 0.1 MPa. The normalized viscosity comparison reveals that the MD simulations can capture the viscosity change with the pressure accurately, although the MD model tends to underpredict the absolute viscosity value. The error gradually increases with temperature, contributing to a slight underestimation of α^* . Such a discrepancy may also be owing to the inaccuracy of the Walther equation in such high temperature and pressure ranges because its extrapolations at high and low temperatures have both shown noticeable errors [59]. A more accurate empirical temperature-viscosity relationship for a wide temperature range should be more beneficial.

Table 2.3 Comparisons of α_0 and α^* between the experimental data [49] and the calculated MD data

	Experiment	MD	Relative Error
α_0	16.3	16.5	1.2%
α^*	10.9	10.1	7.3%

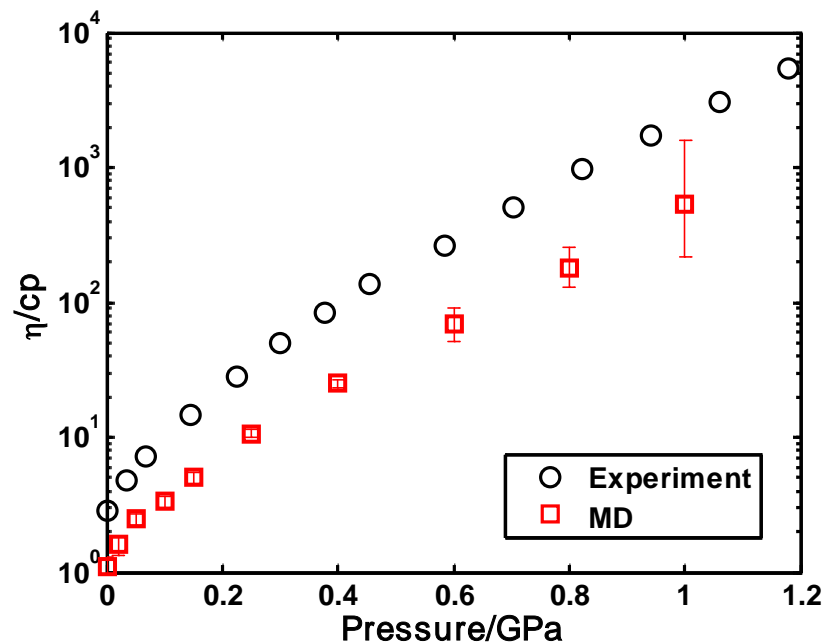


Figure 2.12 Semi-log plot of the viscosity vs. pressure for the 1-Decene trimer. The trend shows a systematic difference between the two curves but their slopes are similar.

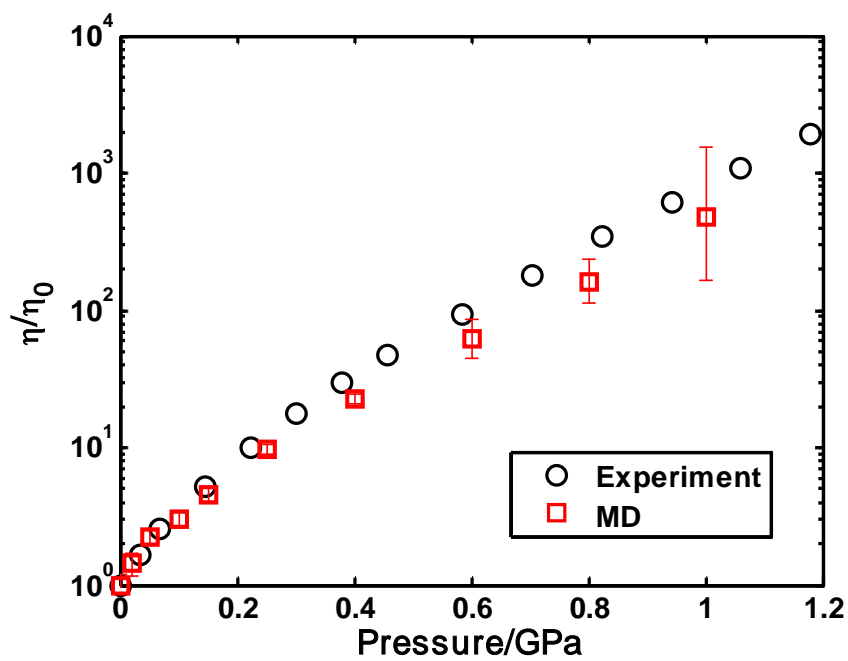


Figure 2.13 Relative viscosity after normalization with the viscosity value at 0.1 MPa.

2.5 Chapter Summary

The viscosity calculations for a branched alkane, 1-Decene trimer, under various pressures and temperatures were achieved through direct NEMD, together with a time-temperature superposition (TTS)-based extrapolations using the simulated results from the NEMD at elevated temperatures, based on the analyses of the rotational relaxation time to determine the successful capture of the 1st Newtonian.. The data were used to obtain the pressure-viscosity coefficients, α_0 and α^* , for this typical base oil. The calculated α values well agree with the experimentally measured data, although the absolute values of the shear viscosity were underestimated by the calculations in general. Well agreed experimental and calculated pressure-viscosity relationships indicate that the proposed model is a promising method for the evaluation of such relationships of base oils in the C₂₀-C₄₀ range. The acquisition of a more accurate and convenient temperature-viscosity model for extrapolation would further improve the accuracy of the α^* prediction.

Chapter 3 Predicting the Critical Shear Rates of Hydrocarbon Lubricants

The temporary apparent viscosity loss, or the temporary shear thinning, of a lubricant significantly affects lubrication film generation at sufficiently high shear rates. The critical shear rate, defined as the onset of the shear thinning, is an important parameter for lubrication system design. The calculation of the viscosity through molecular dynamic (MD) simulations, while having the advantage of attaining an ultra-high shear rate (above 10^8 s^{-1}), often fails to capture the entire shear thinning curve owing to low signal-to-noise ratios at comparatively lower shear rates (10^4 – 10^6 s^{-1}) that are often the shear rates of interest. In this chapter, we propose an approach that correlates the temporary shear thinning phenomenon with the change in the molecular conformation of the lubricant molecules by the characterization of the molecular radius of gyration. This may be valid because the major mechanism of shear thinning is the molecular alignment with the flow field. Squalane ($\text{C}_{30}\text{H}_{62}$), 1-Decene trimer ($\text{C}_{30}\text{H}_{62}$), and low molecular weight olefin-copolymer (OCP, $\text{C}_{90}\text{H}_{182}$) were used to demonstrate that the critical shear rate can be obtained by the proposed method. Time-temperature-pressure superposition (TTPS) was also demonstrated and this approach can be used to further extend the ranges of the temperature and pressure in which we can evaluate the shear thinning behaviors to more conditions of interest.

3.1 Introduction

The rheological properties of the lubricants are determined by the molecular structures of the base oil and the additives, and they in turn affect fluid film generation at the lubricating interfaces. The developments of the viscosity modifiers (VMs) have enabled modern lubricants to have considerably improved temperature-viscosity relationships. The common VMs used in the industry are often from large molecular weight polymers [60]. Owing to the size of the molecules, lubricants with VMs begin to demonstrate a temporary shear thinning behavior [61], when the apparent viscosity decreases as the shear rate increases at the lubricated interfaces. This phenomenon can affect the lubricant film thickness. Figure 3.1 shows a typical shear thinning curve, where the critical shear rate is defined as the onset of the temporary shear thinning. Currently, in order to adequately characterize the shear thinning curve, experimental methods are often used. High-temperature-high-shear (HTHS) measurements are usually performed for shear rates in the range of 10^6 - 10^7 s^{-1} at 100-150 °C, while high pressure viscometers may provide valuable shear-thinning curves at high pressure scenarios [17]. However, for viscometer measurements, the control of the generated heat, when the lubricant experiences severe shearing, is a significant challenge because shear heating alters the film thickness [62], which in turn alters the measured viscosity value. The other common experimental method uses elastohydrodynamic (EHD) film thickness measurements and then back-calculates the shear thinning curve using a

certain type of the EHL model. However, owing to variations in the temperature and pressure at the EHL interface, only an averaged value can be acquired [63].

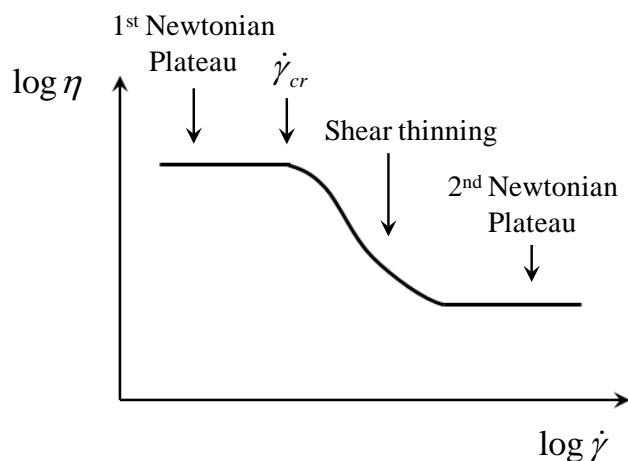


Figure 3.1 A typical shear thinning curve. Critical shear rate $\dot{\gamma}_{cr}$ is defined as the onsite of temporary shear thinning.

Meanwhile, with the improvements in the field of synthetic oils, along with the desire for fuel efficiency, chemical engineers began to tailor molecular structures to obtain the best performance at the given working conditions [64]. For a VM, this would imply that an adequately designed structure would shear thin at a desired shear rate, thereby, reducing the friction loss in the hydrodynamic lubrication regime. Owing to the vast number of possible molecular structures, a prescreening tool based on a molecular-level analysis would be beneficial for such a cause.

As mentioned in Chapter 2, molecular dynamics (MD) simulation is a computer simulation technique that enables the prediction of the time evolution of a system that contains

interacting particles (atoms, molecules, etc.) through the system of equations of motion. Non-equilibrium molecular dynamics (NEMD) [28] in particular, prescribes a shear rate on the system and calculates the shear stress. Because this ratio would be the apparent shear viscosity at such shear rate, it can be used for evaluating shear thinning behaviors. However, acquiring the viscosity value from the NEMD simulations at lower shear rates ($<10^8 \text{ s}^{-1}$) is considerably difficult owing to the low signal-to-noise ratio and the long calculation time required to reach an equilibrium. In Chapter 2, we utilized the concept of the time-temperature superpositioning (TTS) for capturing the 1st Newtonian regime. In this chapter, instead of directly calculating the viscosity as a function of the shear rates, which is significantly limited, we endeavor to use the radius of gyration that can capture the change in the molecular conformation, as an indicator of the change in the shear thinning process.

3.2 Model Description

The major mechanism for temporary shear thinning is that when the shear rate is sufficiently high, the system cannot respond fast enough to return to its relaxed state, and the alignment of the molecules with the flow field begin to appear, resulting in a reduced viscosity [40]. At sufficiently high shear rates, the shapes of the polymer coils change from spherical, or ellipsoidal, to elongated configurations, as shown in Figure 3.2.

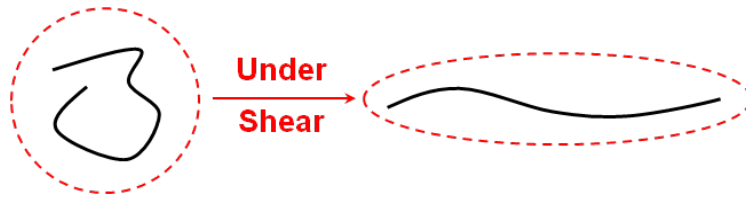


Figure 3.2 A spherically conformed polymer (left) and its alignment (right) with the shear field at sufficiently high shear rates.

The radius of gyration (R_g), defined below, can describe the overall spread of the molecule based on the mass distribution.

$$R_g^2 = \frac{1}{M} \sum m_i (\mathbf{r}_i - \mathbf{r}_{cm})^2 \quad (3.1)$$

where M is molecular weight of the molecule, m_i is the weight of each individual atom or particle i , \mathbf{r}_i is the location of the atom or particle i , and \mathbf{r}_{cm} is the location of the center of mass of the entire molecule.

During shear thinning, the degree of alignment of the molecule may be captured through the R_g calculations, and the change in R_g should correspond to the viscosity decrease during the shear thinning process, as shown in the Figure 3.3, method 1. To further extend the range of the pressure and temperature in which we can evaluate, we also attempted to incorporate the concept of the time-temperature-pressure superpositioning (TTPS), as shown in Figure 3.3, method 2, where certain shift rules are used for acquiring a mastercurve for combining cases at different pressures and temperatures.

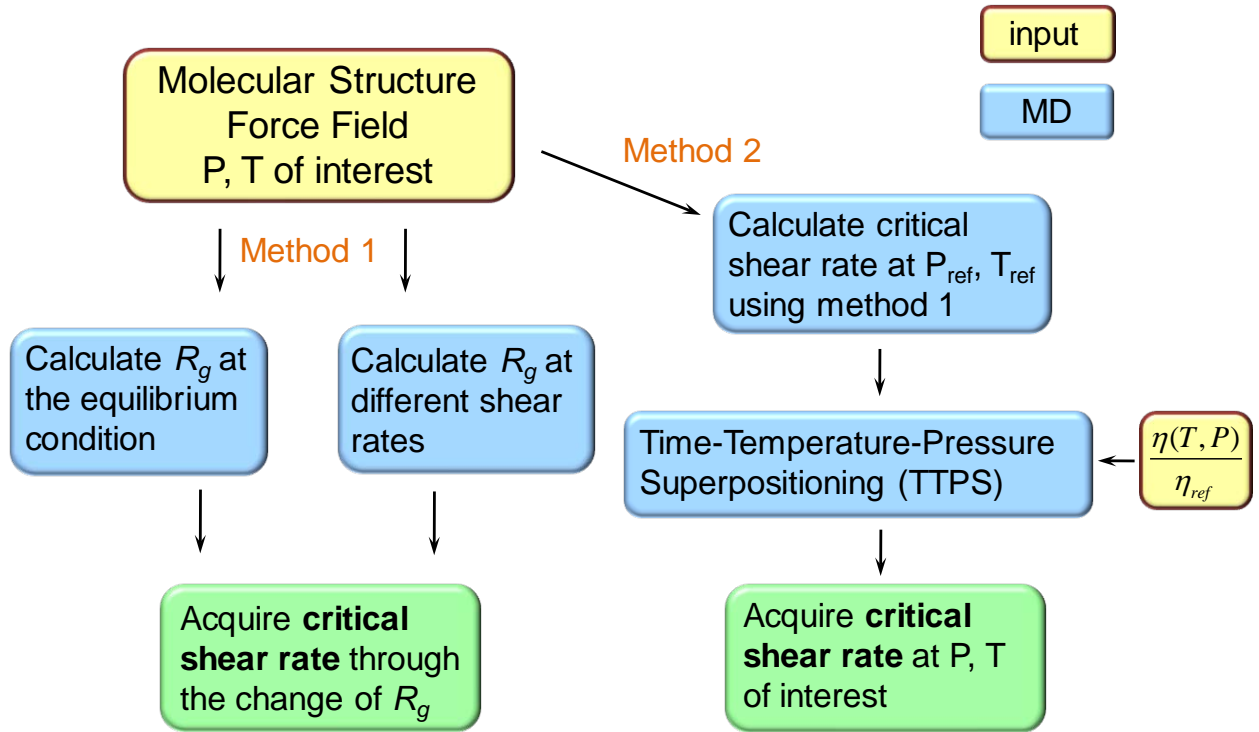


Figure 3.3 Flowchart for the simulation.

The shear thinning behavior of a lubricant, shown in Figure 3.2, follows the variation of the Carreau equation [40] as a function of shear rate, $\dot{\gamma}$, where η_1 is the first Newtonian viscosity, $\dot{\gamma}_{cr}$ is the critical shear rate, and n is the power-law exponent. Equation 3.3 shows the relationship between the critical shear rate and G , the effective shear modulus. For the TTPS, Equation 3.4 will be used as the shift rule because it has been demonstrated that mastercurves can be built for different lubricants [65], where ρ is the density of the lubricant, T is the temperature, and the subscript, R , indicates values at the reference state.

$$\eta_s(\dot{\gamma}) = \eta_1 \left[1 + \left(\frac{\dot{\gamma}}{\dot{\gamma}_{cr}} \right)^2 \right]^{\frac{n-1}{2}} \quad (3.2)$$

$$G = \eta_1 \dot{\gamma}_{cr} \quad (3.3)$$

$$G = G_R \frac{\rho T}{\rho_R T_R} \quad (3.4)$$

3.3 Molecular Dynamics Simulation Details for Squalane, 1-Decene Trimer, and OCP

The united atom (UA) method was used to generate the molecular structures. Each CH₃, CH₂ and CH group was considered as a pseudoatom within the hydrocarbon chain with the interaction center at the nucleus of each carbon atom. Three structures were simulated here based on the details shown in Figure 3.4. Squalane (2-, 6-, 10-, 15-, 19- and 3-hexamethyl-tetracosane) is commonly used as a reference liquid for model developments [66] because it can be purchased in a highly pure state and has thermophysical properties similar to the lubricating oils. 1-Decene trimer is the major component of poly- α -olefin (PAO) 4cSt or PAO 4, an important fluid in the current synthetic base oil market. It has a shorter backbone that connects with three sidechains of eight carbons each. Olefin copolymer (OCP) is an important type of viscosity modifier that is widely used in the lubricant industry. Its molecular weight can be as high as 300,000 g/mol in industrial applications, exceeding the limit of the MD simulation at the existing computational capability. Thus, a model OCP with an intermediate molecular weight (C₉₀H₁₈₂) was considered here to study the possible effects of an increased backbone length. The order of ethylene (C₂H₄) and propylene (C₃H₆) was randomly determined with a ratio set at 1:1. Thirty (30) molecules of

squalane, eighty (80) molecules of 1-Decene trimer, and twenty (20) molecules of OCP were generated in their respective systems.

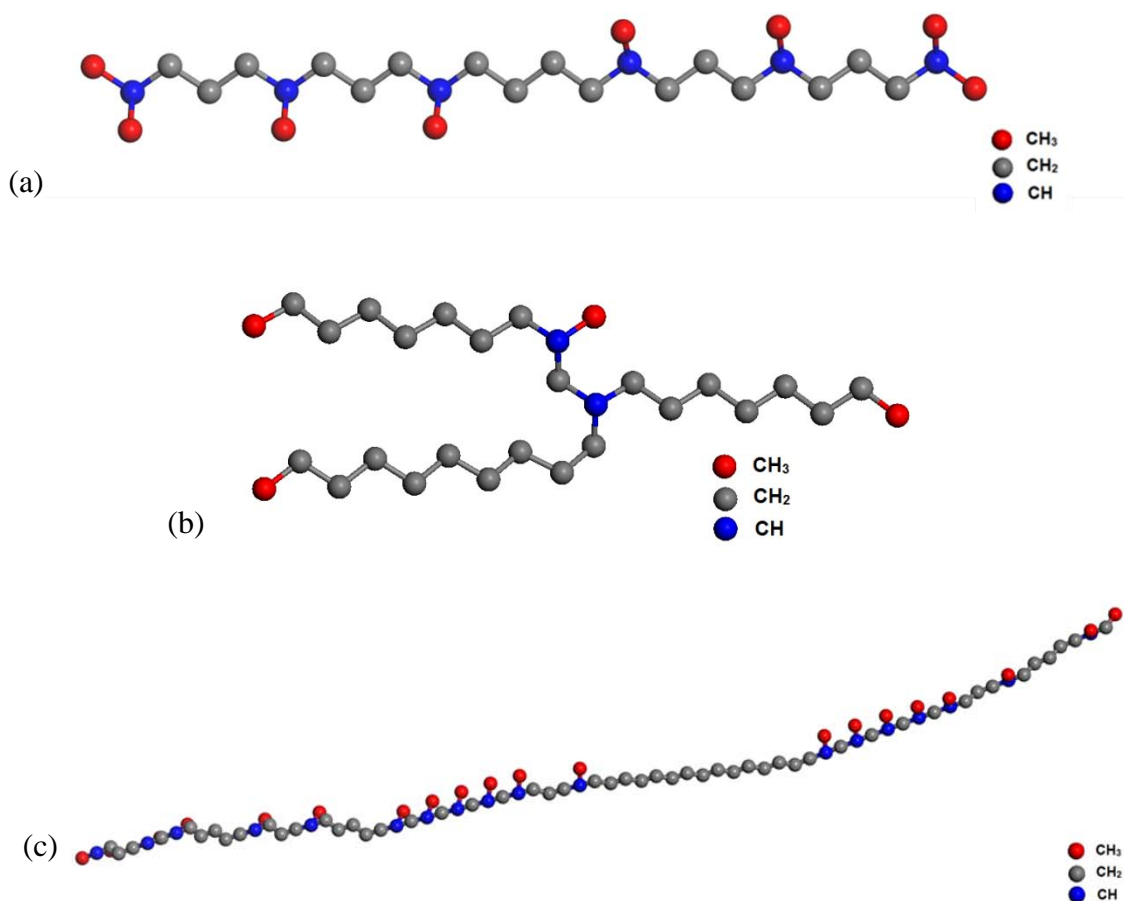


Figure 3.4 Molecular Structures of (a) squalane, (b) PAO 4 and (c) OCP.

The force field used to describe the molecules is consistent with the one used in Chapter 2, where the detailed parameters can be found. The force field was proposed by Siepmann et al. [50], and later extended to branched alkanes by Mondello and Grest [23]. Moreover, the stiff, fixed bond length was replaced by a harmonic potential to generate a fully flexible bond [51].

The systems of different molecules were first created and relaxed in the Materials Studios software for acquiring the initial distribution of the pseudoatoms. The molecules were placed randomly and relaxed in simulation boxes of different sizes. The LAMMPS software [54,55] was used for the MD simulations, and a timestep of 1 fs was applied. During MD simulations, initially, the system ran for 20 ns to enable it to reach equilibrium at the assigned temperature and pressure. This equilibrium configuration provided the initial state for the NEMD simulations and was called the equilibrium step. Then, the molecules underwent a planar Couette flow using the SLLOD equations of motion [28] for 100 ns, called the shear step. The Lees-Edwards periodic boundary conditions were applied and a Nosé/Hoover thermostat was coupled for achieving the energy conservation of the system, as proposed by Tuckerman et al. [57]. The measured resulting shear stress divided by the imposed strain is the value of the shear viscosity and this is averaged after system stabilization. The radius of gyration was acquired by averaging the radius of gyration of each molecule in the system.

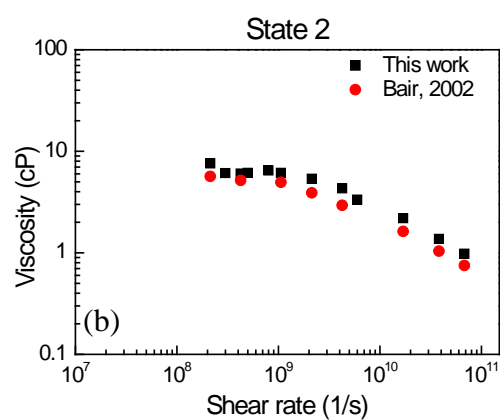
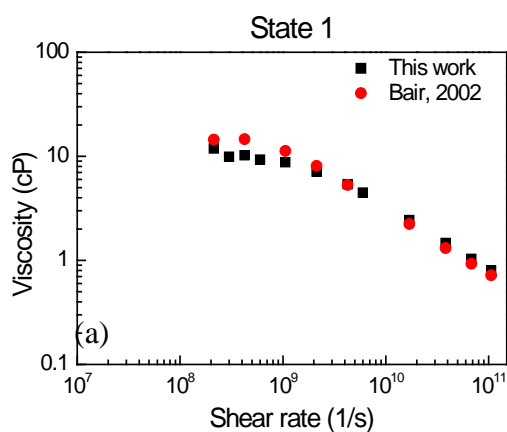
3.4 Results and Discussions

3.4.1 Model Validation: Shear Viscosities of Squalane

The molecular dynamics simulations of squalane were conducted to validate the MD model. Three states of squalane (listed in Table 3.1) were regenerated according to the reference paper [46] and the shear thinning curves were plotted in Figure 3.5 for comparison. We can see that the shear thinning curves of the three states are in a good agreement with the results in the reference.

Table 3.1 NEMD simulation conditions for three molecules at different pressures and temperatures. Three different states of squalane, six different states of PAO 4, and four different states of OCP were calculated

State	Squalane(C ₃₀)			PAO4 (C ₃₀)			OCP (C ₃₀)		
	P(MPa)	T (°C)	$\dot{\gamma}$ (1/s)	P(MPa)	T (°C)	$\dot{\gamma}$ (1/s)	P(MPa)	T (°C)	$\dot{\gamma}$ (1/s)
1	0.1	40	2.13×10^8 - 1.06×10^{11}	0.1	40	2×10^8 - 2×10^{10}	0.1	100	1×10^8 - 2×10^{10}
2	0.1	60	2.13×10^8 - 6.8×10^{10}	0.1	100	2×10^8 - 2×10^{10}	0.1	150	1×10^8 - 2×10^{10}
3	316	100	2.13×10^7 - 6.8×10^{10}	0.1	150	2×10^8 - 3×10^{11}	0.1	200	1×10^8 - 2×10^{10}
4				250	40	2×10^8 - 2×10^{10}	250	200	1×10^8 - 2×10^{10}
5				250	100	2×10^8 - 2×10^{10}			
6				600	175	2×10^8 - 2×10^{10}			



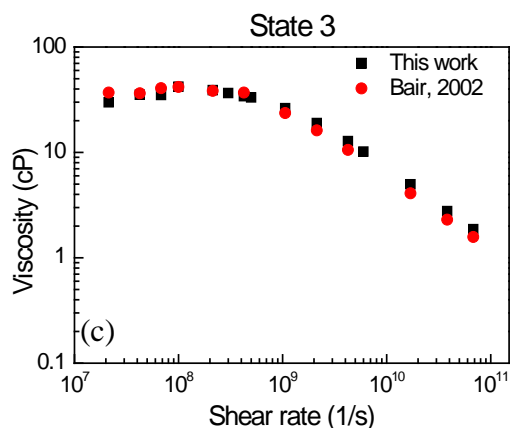


Figure 3.5 Model validation: Shear thinning curves for squalane at (a) State 1: 0.1 MPa, 40 °C, (b) State 2: 0.1 MPa, 60 °C, and (c) State 3: 316 MPa, 100 °C, compared to the MD results in [46].

3.4.2 Change in the Radius of Gyration under Shearing in the Non-Newtonian Regime

In this section, PAO 4 at a state of 600 MPa, 175 °C, with a shear rate of $4 \times 10^9 \text{ s}^{-1}$, was selected to demonstrate some of the details in the simulations. Figure 3.6 clearly shows the increase in the radius of gyration from the equilibrium state (0-20 ns) to the shear thinning state (20-120 ns). This increment in the radius of gyration corresponds to the alignment of the molecules with the flow field, which is the mechanism for temporary shear thinning. This indicates that modeling the variations in radius of gyration catches the root mechanism for shear thinning. Figure 3.7 shows the viscosity and the radius of gyration calculations for PAO 4 at various shear rates. We can see that at equilibrium and at low shear rate conditions, the radius of gyration remains relatively constant, corresponding to the 1st Newtonian regime; when the shear rate increases and the system begins to undergo shear thinning, the radius of gyration increases

with a decrease in the viscosity. Moreover, we found that the transition point, which marks the critical shear rate value, can be correlated in the two graphs. This phenomenon provides an alternative method for evaluating the position of the critical shear rate for tackling the challenges posed by the direct viscosity calculations, particularly, when the 1st Newtonian viscosity cannot be directly achieved for large molecules. Meanwhile, the R_g at equilibrium is more attainable in the MD simulations.

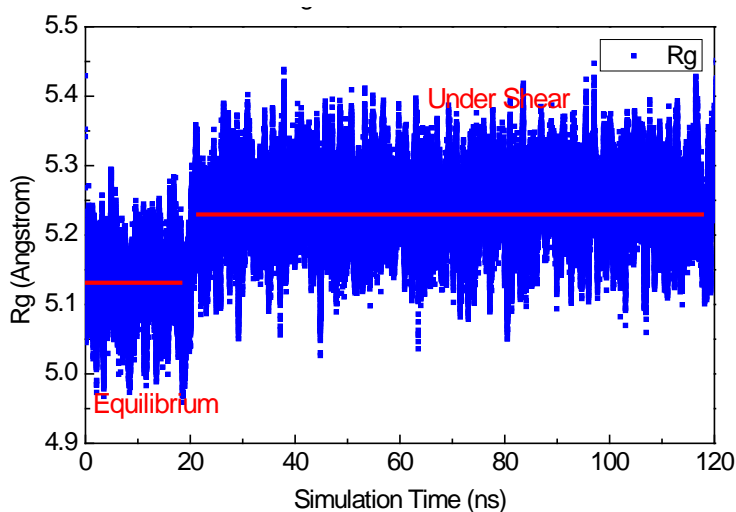


Figure 3.6 Variation of the radius of gyration vs. simulation time. The radius of gyration of the molecule increased under a sufficiently high shear rate.

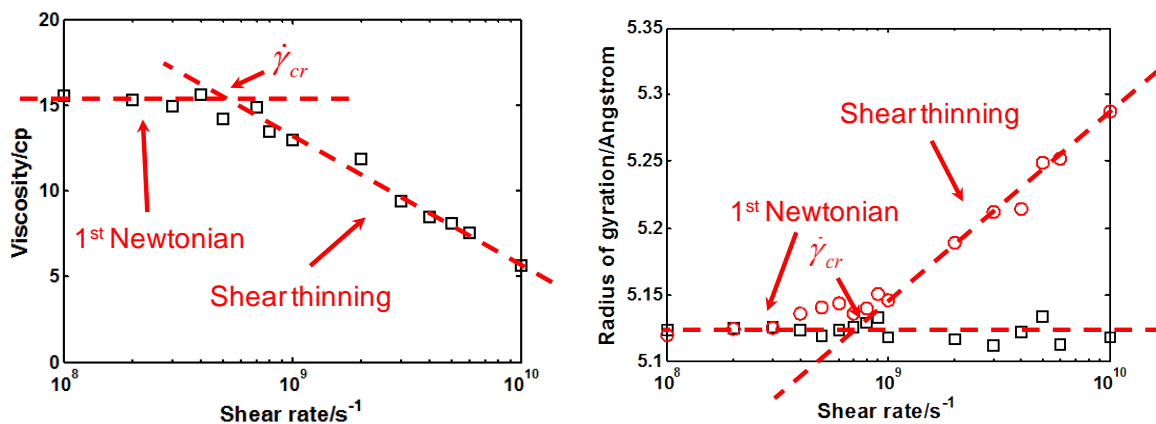


Figure 3.7 (a) Viscosity and (b) the radius of gyration calculations for PAO 4 at various shear rates (log scale). Two lines can be drawn for the 1st Newtonian and the shear thinning regimes. The cross point of the two lines is an estimation of the critical shear rate value, which are $5.6 \times 10^8 \text{ s}^{-1}$ and $6.7 \times 10^8 \text{ s}^{-1}$, respectively.

3.4.3 Comparisons between the Critical Shear Rates Calculated from the Viscosity Curves and those from the Radius of Gyration Curves

The molecular dynamics simulations of PAO 4 (C_{30}), squalane (C_{30}), and OCP (C_{90}) were conducted for a wide range of temperature and pressure (as listed in Table 3.1), for further validations of the method. The viscosity shear thinning curve and the R_g curve were both plotted in the same figure for comparison. The $\dot{\gamma}_{cr}$ from the shear thinning curve was acquired by fitting the viscosity values at different shear rates into the Carreau model (Equation 3.2). The $\dot{\gamma}_{cr}$ from the radius of gyration curve was acquired by fitting a Carreau-like radius of gyration model, as shown in Equation 3.5:

$$R_g = R_g(e) \left[1 + \left(\frac{\dot{\gamma}}{\dot{\gamma}_{cr}} \right)^d \right]^{\frac{n_{Rg}-1}{d}}, \quad (3.5)$$

where $R_g(e)$ is the radius of gyration at the equilibrium stage when the system is fully relaxed under the applied conditions; n_{Rg} is the power-law exponent that is larger than 1 because R_g increases as the shear rate increases. The parameter, d , replaces ratio 2 in the Carreau equation for viscosity. This modification is similar to that of the Carreau-Yasuda equation [40].

In Figure 3.8, the shear thinning curve and its fitted result, the R_g curve, and its fitted result, and the $R_g(e)$ (secondary axis) for PAO 4 are plotted together for a direct comparison. At low shear rates, since it was sufficient for the molecule to relax itself, the shape of the molecule was unchanged. Thus, R_g under a low shear is similar to R_g at its equilibrium (indicated by $R_g(e)$). At high shear rates, R_g increases as the molecules began to align with the flow field. We can see from the first three states of the PAO 4 cases that $\dot{\gamma}_{cr}$ increases as the temperature increases. The thermal motion of the molecules will increase with a rise in temperature; hence the molecules show a quicker response to the applied shear flow. Therefore, the relaxation time is shorter. Thus, the critical shear rate increases accordingly. Both the shear thinning curve and the R_g curve start to turn at approximately the same shear rates, indicating that the R_g curve can be used to estimate $\dot{\gamma}_{cr}$ because it can capture the transition of the shear thinning. Equations 3.2 and 3.5 were used to fit the shear thinning and the R_g curves, and the fitted results of the critical

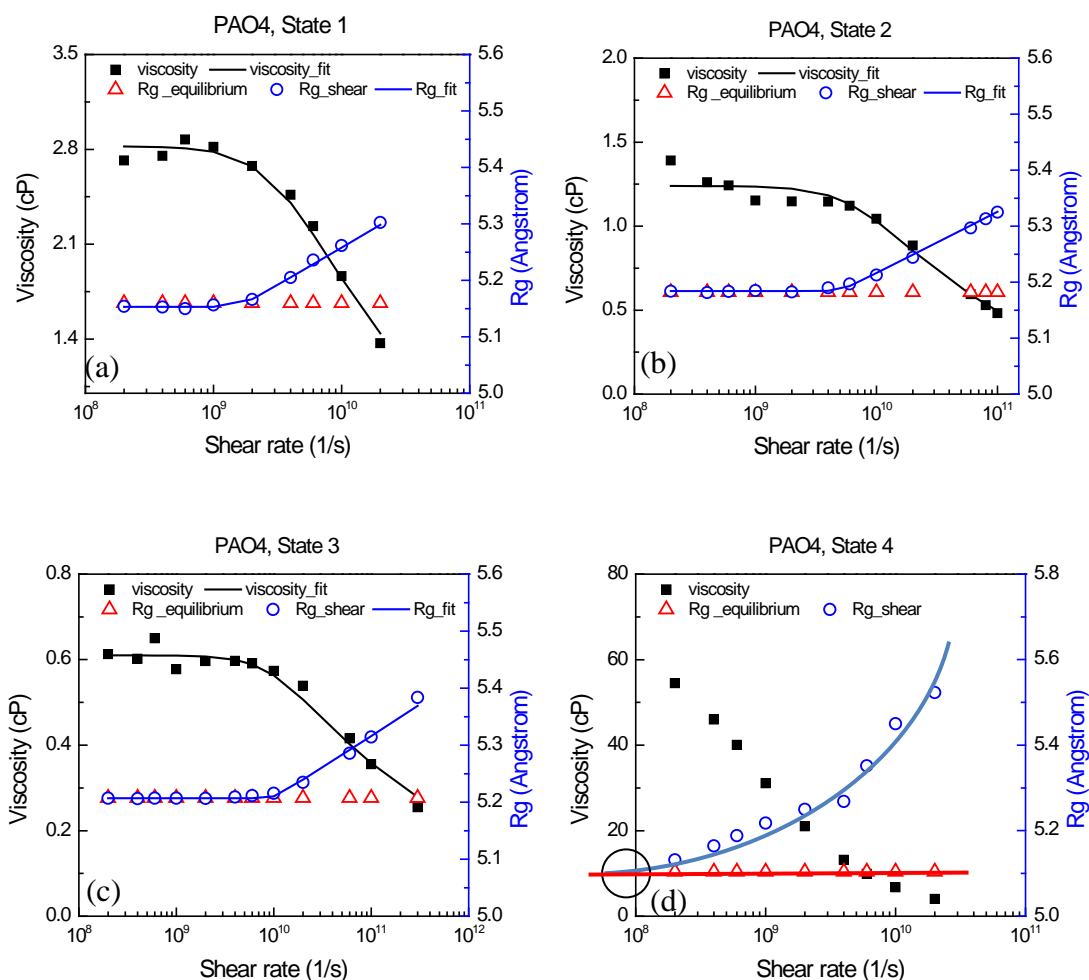
shear rate $\dot{\gamma}_{cr}$ were acquired accordingly. Figure 3.11 shows the comparisons of the critical shear rates acquired through the two methods, and they agreed well with each other in general.

From State 4 of the PAO 4 case, we can see that with the assistance of the R_g curve, an estimation of $\dot{\gamma}_{cr}$ can be acquired, even though the 1st Newtonian viscosity cannot be directly acquired from the MD simulations. As indicated before, R_g in the high shear rate regime increases almost log linearly when the shear rates are plotted in a log scale; hence, by fitting the R_g curve at high shear rates to a log-scale straight line and by connecting this straight line with the R_g (e), we can acquire the cross point of the two straight lines. This cross point indicates the estimation for the start of the transitions in both viscosity and R_g , which should be the critical shear rate, $\dot{\gamma}_{cr}$. Traditionally, the 1st Newtonian plateau in the shear thinning curve is required to determine $\dot{\gamma}_{cr}$, else the transition point cannot be captured. Moreover, we cannot directly combine the 1st Newtonian viscosity from the experiments with the MD simulations at high shear rates because at the current stage, a direct quantitative comparison of the viscosity cannot be achieved. Therefore, using the R_g calculations, $\dot{\gamma}_{cr}$ can be estimated even without reaching the 1st Newtonian plateau because R_g (e) can be acquired at the equilibrium step. This would be crucial for large molecules with large sizes because shear thinning takes place at a low shear rate well before the shear rate range of the MD simulations.

In Figures 3.9 and 3.10, both OCP (C₉₀) and squalane (C₃₀) cases show a trend similar to the PAO 4 cases. The transition regions for both the curves in each state are similar to each other,

except for squalane State 3 (Figure 3.10(c)). In this state, the 1st Newtonian plateau is not well characterized because the shear rate extended below 10^8 s^{-1} , which was expected as the signal-to-noise ratio decreased. We believe that the 1st Newtonian plateau in this state can only be partially captured; hence, the estimated $\dot{\gamma}_{cr}$ is different compared to the $\dot{\gamma}_{cr}$ from the R_g curve. Other than this state, the $\dot{\gamma}_{cr}$ estimation from both curves correlated well for squalane, PAO 4 and OCP, as shown in Figure 3.11. The pressure and temperature applied at each state is listed in Table 3.1.

Table 3.1.



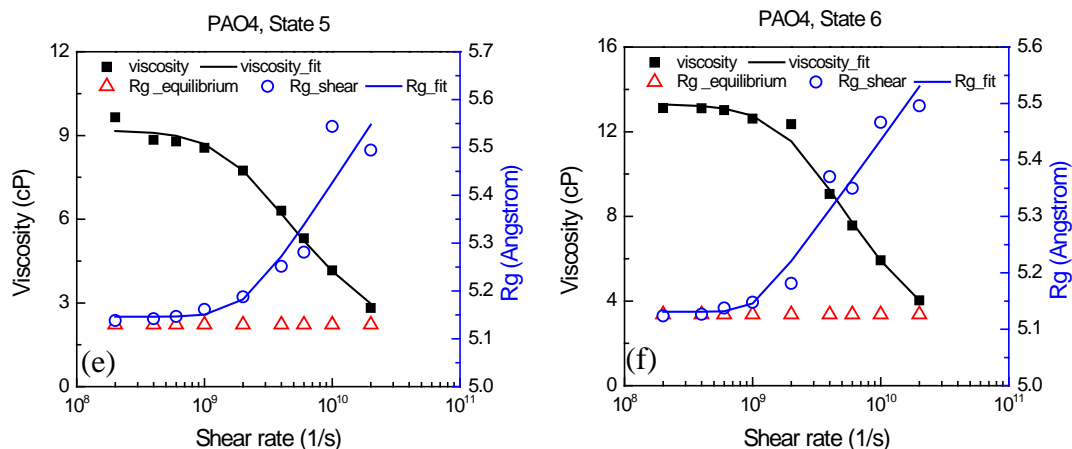
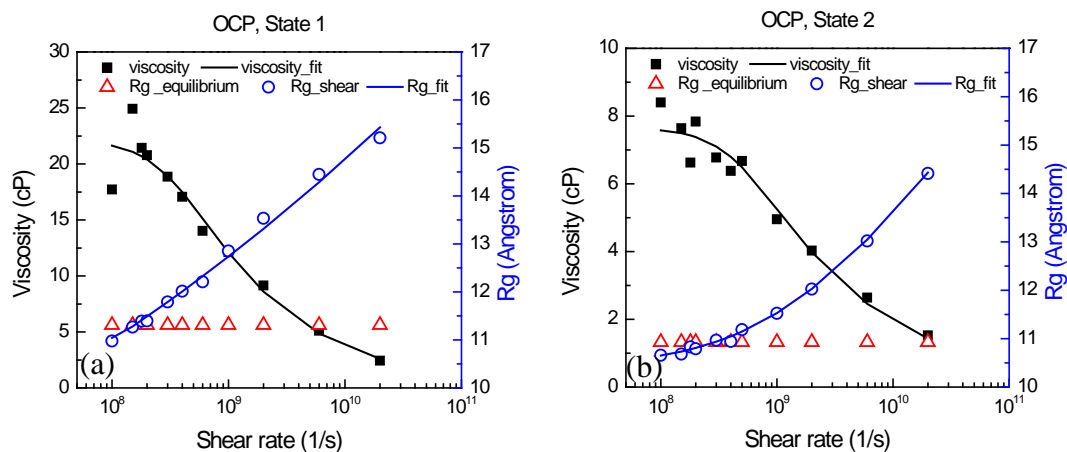


Figure 3.8 The shear thinning and R_g curves for PAO 4 at (a) State 1: 0.1 MPa, 40 °C, (b) State 2: 0.1 MPa, 100 °C, (c) State 3: 0.1 MPa, 150 °C, (d) State 4: 250 MPa, 40 °C, (e) State 5: 250 MPa, 100 °C, (f) State 6: 600 MPa, 175 °C. The critical shear rate reached below 10^8 s^{-1} for State 4, and cannot be properly captured directly through viscosity calculation, whereas it can be estimated using the radius of gyration. The MD calculated viscosity (square) and the radius of gyration (circle) are fitted using Equations 3.2 and 3.5, respectively.



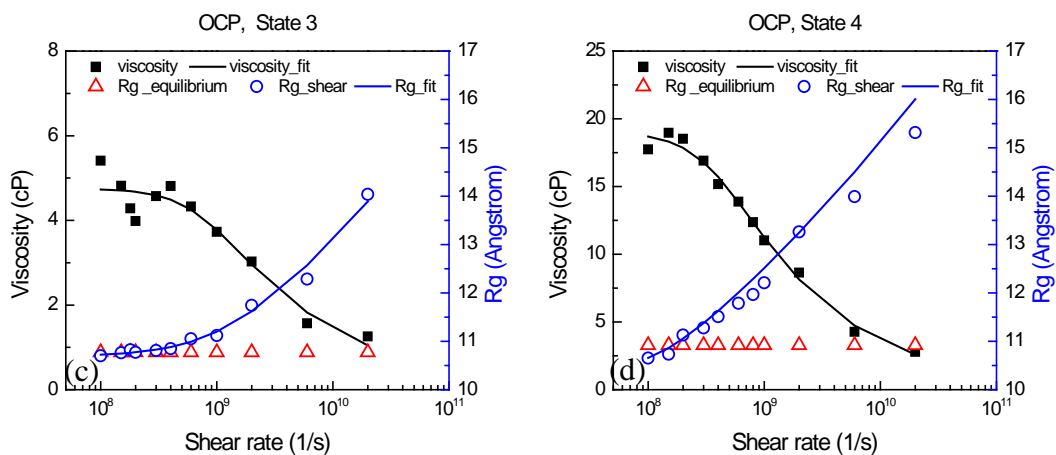
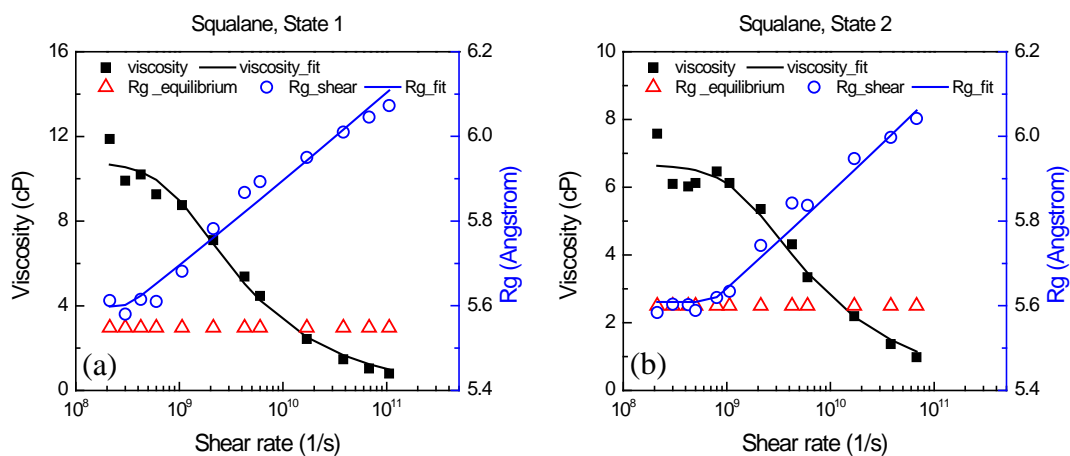


Figure 3.9 The shear thinning and R_g curves for OCP at (a) State 1: 0.1 MPa, 100 °C, (b) State 2: 0.1 MPa, 150 °C, (c) State 3: 0.1 MPa, 200 °C, and (d) State 4: 250 MPa, 200 °C. The MD calculated viscosity (square) and R_g (circle) are fitted using Equations 3.2 and 3.5, respectively.



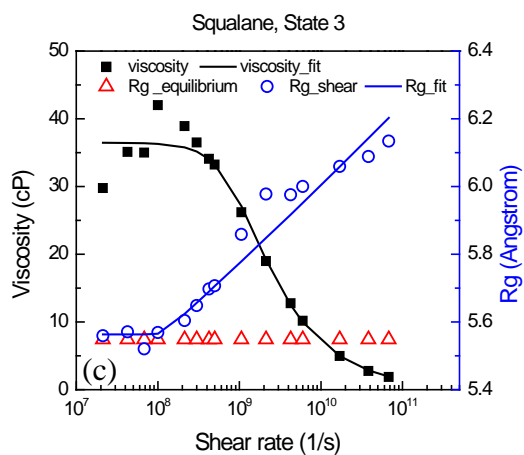
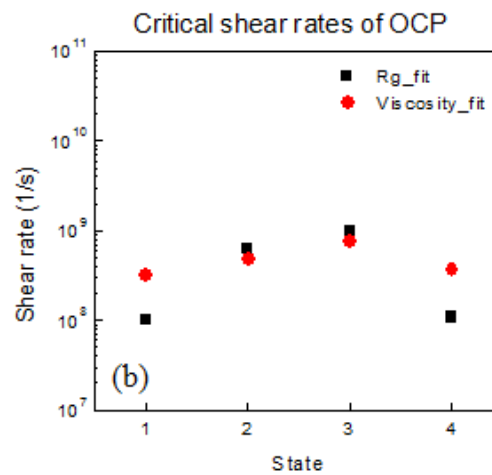
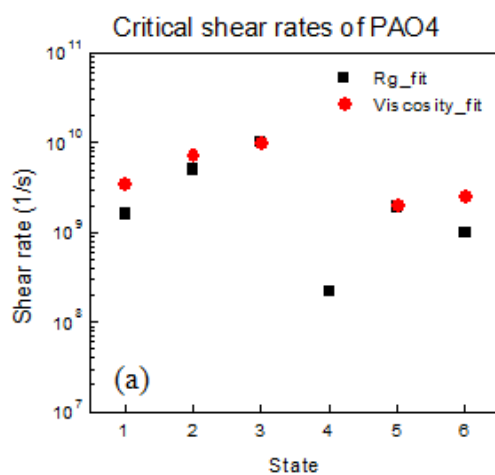


Figure 3.10 The shear thinning and R_g curves for squalane at (a) State 1: 0.1 MPa, 40 °C, (b) State 2: 0.1 MPa, 100 °C, and (c) State 3: 316 MPa, 100 °C. The MD calculated viscosity (square) and the radius of gyration (circle) are fitted using Equations 3.2 and 3.5, respectively.



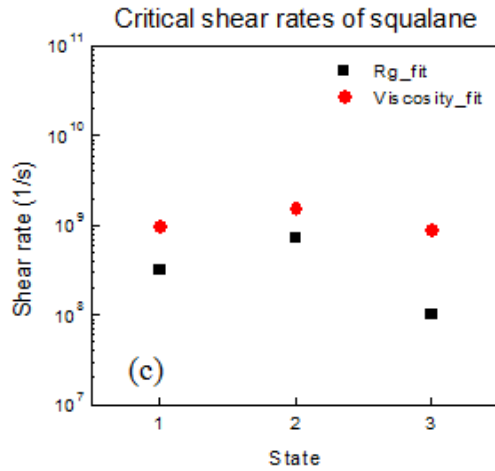
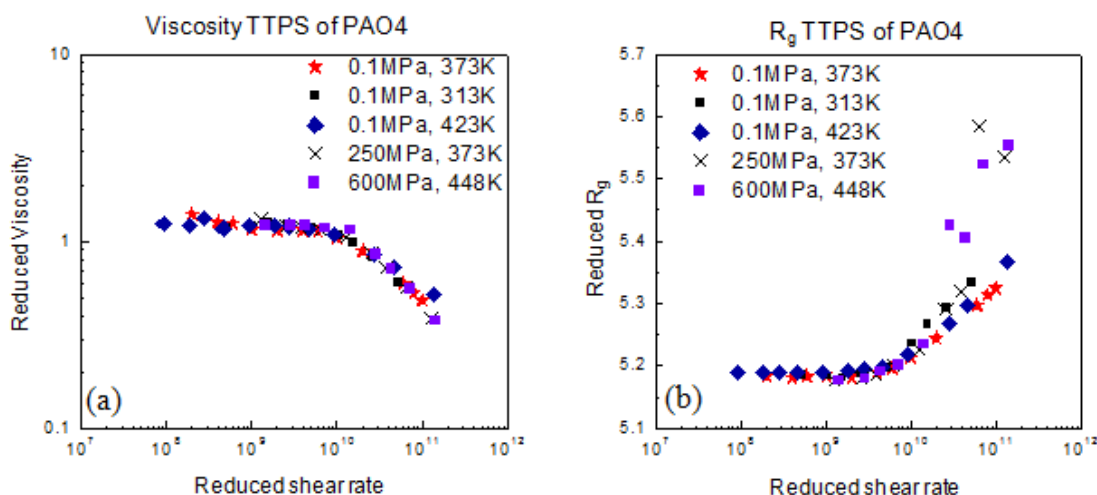


Figure 3.11 Critical shear rates of (a) PAO 4, (b) OCP, and (c) squalane at various states. The critical shear rates are fitted from calculations of the viscosity and the radius of gyration using Equations 3.2 and 3.5, respectively.

3.4.4 Time-Temperature-Pressure Superpositioning (TTPS) of the Viscosity and the Radius of Gyration

Time-temperature-pressure superpositioning (TTPS) can further extend the pressure and temperature range that can be calculated through MD simulations, particularly, for the shear thinning characterization of the critical shear rate and n , the power-law exponent. TTPS were performed to combine the viscosity data and the R_g data from different states into one mastercurve. The viscosity data was plotted using a reduced viscosity $\eta \left(\frac{\eta(T,P)}{\eta_R} \right)$, as a function of the reduced shear rate, using Equation 3.4 as proposed in [65]. For the TTPS of the R_g data, the following method is proposed: the R_g data was plotted using a reduced radius of gyration $R_g \left(\frac{R_g(T,P)}{R_{gR}} \right)$, and using the same function $\dot{\gamma} \left(\frac{\eta}{\eta_R} \right) \left(\frac{G_R}{G} \right)$ for the reduced shear rate.

Figure 3.12 shows the side-by-side comparisons of the TTPS of the three different molecules. Pressure and temperature of 0.1 MPa and 373 K was used as the reference state for PAO4 and OCP, while the pressure of 313 MPa and the temperature of 373 K were used as the reference state for squalane. 250 MPa, 40 °C was not plotted on the mastercurve for PAO 4, because the low shear viscosity data was not known. Figure 3.12 clearly shows that the TTPS of the viscosity followed an appropriate trend throughout the entire shear rate range. For the TTPS of R_g , the trend was well maintained in all the low pressure states for the range of the shear rates; the R_g from all the high pressure states in the high shear regime seemed to deviate from the mastercurve, particularly, in the PAO 4 case, where two high pressure states showed the maximum deviation. However, we believe that this is sufficient for acquiring the value of the critical shear rate, which is the desired parameter in this portion of our study.



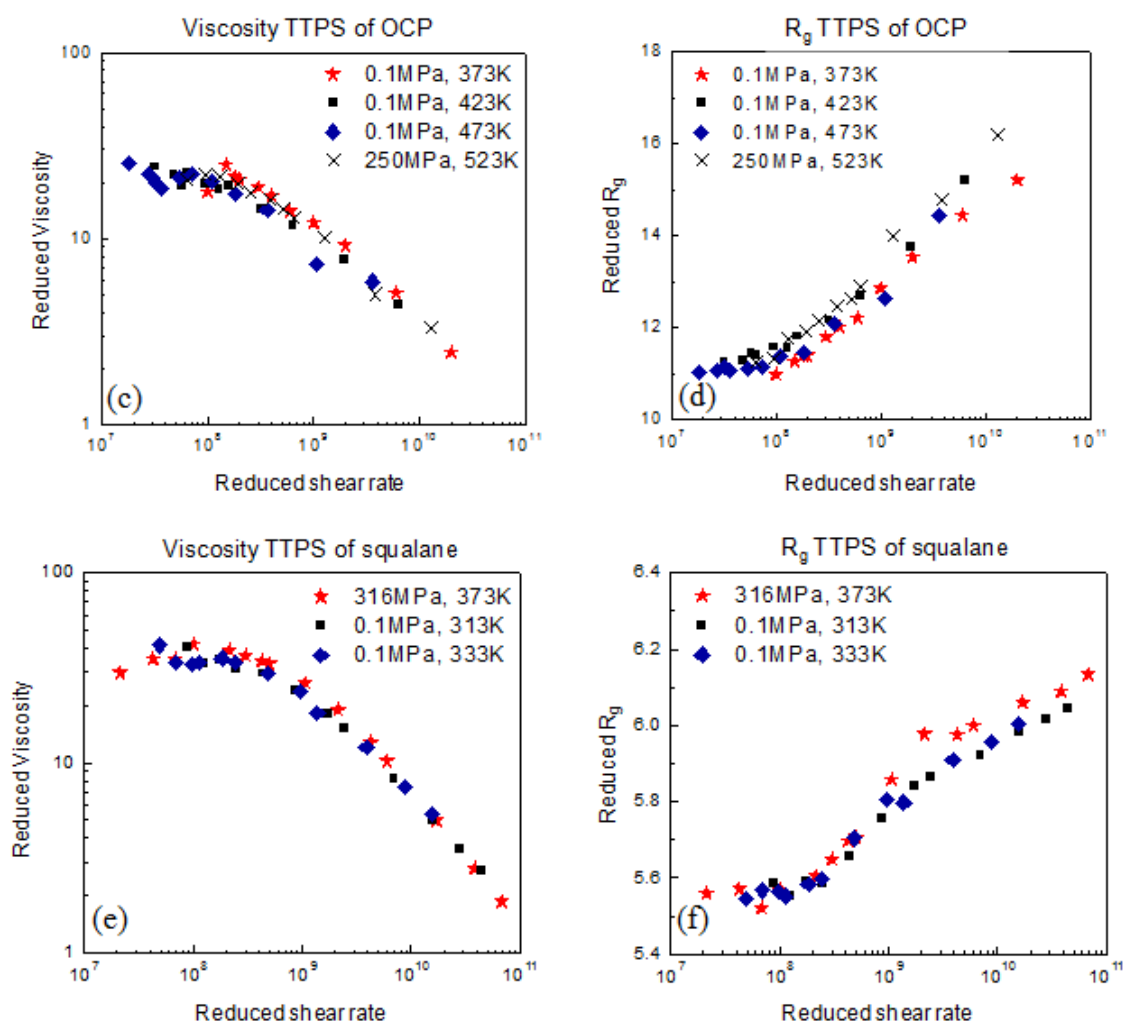


Figure 3.12 The reduced viscosity and the reduced R_g vs. the reduced shear rate for PAO4 ((a) and (b)), OCP ((c) and (d)), and squalane ((e) and (f)).

3.5 Chapter Summary

A novel concept of utilizing the change in radius of gyration to predict the critical shear rate is proposed.

- 1) The radii of gyration at various shear rates were calculated for the three molecular structures, 1-Decene trimer ($C_{30}H_{62}$), squalane ($C_{30}H_{62}$), and OCP ($C_{90}H_{182}$), respectively. The increase in the radius of gyration at increased shear rates was correlated successfully to the temporary shear thinning behavior of the lubricant. The transition region and the critical shear rate estimated by both the shear thinning curve and the R_g curve agreed reasonably well with each other.
- 2) TTPS of both the viscosity and the R_g data through the MD simulations were also demonstrated for a wide range of temperatures and pressures. Mastercurves for both viscosity and R_g was acquired for the three lubricants.

Utilization of R_g as an indicator provides a method for evaluating the shear thinning behaviors of various molecular structures, when a direct acquisition of the viscosity is challenging and at times impractical; TTPS further expands the molecular structures and sizes that can be evaluated for various applications, and reduces the number of simulation cases needed at specific pressure and temperature once the mastercurve is established.

Chapter 4 Viscosity Modeling of Synthetic Polymer Lubricants

Molecular dynamics (MD) simulations is a valuable tool for lubricant development because it enables the lubricant of favorable properties to be built from a molecular level. The viscosities of polymers are of significant interest, because properly designed structures can be used for developing high viscosity index (VI) lubricants, either as base oils [67,68] or for use as viscosity modifiers (VM) [69-71]. However, owing to the time- and length-scale limitations, calculating the viscosities of long-chain polymers using MD are often unpractical with the existing computational power. In this chapter, the viscosities of large molecule polymers are predicted using MD simulations and a structural-viscosity model based on the model developed by Berry and Fox [72], in which the viscosities of the polymers can be determined based on the monomeric friction coefficient and a structural factor. The monomeric friction coefficient, which is independent of the degree of polymerization, is acquired through the viscosity of a structure with the same monomer. All the other necessary parameters for the structural factor such as the density and the radius of gyration are obtained directly from the MD simulations. The model is applied to linear (Polyethylene) and branched (Poly- α -olefin) polymers for validations. Once validated, it should enable us to extend the molecular size that can be evaluated. Poly- α -olefin, in particular, is a key base stock in synthetic lubricants. To improve the accuracy of the original

model, the empirical constants were further modified depending on the specific polymer structures.

4.1 Introduction

Viscosity properties significantly affect the performance of the lubricant at an interface. To accommodate a wide range of working conditions, a high viscosity index (VI) fluid is desired for enabling the system to perform at a high level for a wide temperature range. To achieve such goals, various approaches for synthesizing different new chemicals have been attempted, either as high VI base oils, such as ester [73-75] and poly- α -olefin [76,77], or for the development of VI improvers, such as olefin-copolymers (OCP) [78,79], polyisobutylene (PIB) [80-82], and heavily branched "star" polymers [83,69,84,85]. Regardless of the nature of the approach, a suitable characterizations of the viscosities of such polymer structures, either in a pure form or in mixtures, is necessary for determining the temperature-viscosity performance of the final lubricant. However, owing to the complexity and the availability of several possibilities during the synthesis process, trial and error can be expensive. Meanwhile, in the development stage of the synthesis, acquiring one sample with a relatively low molecular weight is often easier than attaining a large molecular weight sample. Therefore, a predictive evaluation method to extend the size of the molecule we can evaluate for property improvement while reducing the required synthesizing effort will significantly assist the development of new lubricants.

Molecular dynamics (MD) simulations, in which the system can be built from the molecular structure level, offers an opportunity for designing molecules for evaluating their rheological performances. However, owing to time- and length-scale limitations, calculating the viscosity of long-chain polymers using MD are often unpractical with the existing computational power. Chapters 2 and 3 reported the utilization of the concept of time-temperature superpositioning (TTS) and the characterization of the molecular conformation to overcome this challenge. In this Chapter, an empirical-theoretical structural-viscosity model will be used in combination with the MD simulations to extend the size of the molecules that can be evaluated.

4.2 Structural-Viscosity Model

The advances in polymer synthesis techniques in recent decades have facilitated research on the relationship of the polymer structure with the rheological properties of the polymer. Berry and Fox [72] developed an empirical-theoretical structural-viscosity model, based on the previous work of Schaeffgen and Flory [86], Fox [87], and Fox and Allen [88], to include branched polymers, applicable for a range of polymer structures in bulk and solvent conditions.

Fox and Allen [88] introduced a viscosity dimensional factor, X , to approximate the viscosity and molecular entanglement conditions for several polymers using the unperturbed mean square radius of gyration $\langle s^2 \rangle_0$. Berry and Fox [96] later refined the dimensional factor to include the ratio of radii of gyration g to account for the branch content, as shown below:

$$X = Zg(\langle s^2 \rangle_0 / M)\phi_2 / \nu_0 \quad (4.1)$$

where Z is the chain length, $\langle s^2 \rangle_0$ is the mean square radius of gyration, $g = \langle s^2 \rangle_{br} / \langle s^2 \rangle_l$ represents the ratio between the mean square radius of gyration of the branch content to that of a linear chain, φ_2 is the volume fraction and is equal to one for pure lubricants. M is the molecular weight, and v_0 is the specific volume that is the reciprocal of the density. For notation consistency with the previous chapters, the unperturbed radius of gyration $\sqrt{\langle s^2 \rangle_0}$ will be noted as R_g .

The dimensional factor is used to calculate a structural factor (Equation 4.2) that describes the observation relationship between the viscosity and the polymer length, or molecular weight. The structural factor includes Avogadro's number N_0 and an exponent a describing the increase in viscosity with X . The value of the exponent, a , changes at a critical dimensional factor, X_c , which also corresponds to a critical mass, M_c . The monomeric friction factor describes the resistance to motion between the monomers of a given lubricant type. It varies due to the influences of the branch type, length, and content but is not affected by the degree of polymerization.

$$F(X) = \left(\frac{N_0}{6} \right) X_c \left(\frac{X}{X_c} \right)^a, \quad \begin{array}{l} a = 1 \quad \text{for } X < X_c \\ a = 3.4 \quad \text{for } X \geq X_c \end{array} \quad (4.2)$$

Therefore, the viscosities of polymers of different molecular weights are calculated via a two-step process. First, utilizing the viscosity data from one structure, the monomeric friction coefficient, $\zeta_0(T)$ is calculated. Then, the monomeric friction coefficient is multiplied by the

structural factors $F(X)$ of the other molecular weight structures with the same monomer to predict the viscosities of the corresponding structures, as shown in Equation 4.3, where X_1 is the selected structure, for which the viscosity has been previously obtained.

$$\eta_0(T) = F(X) \cdot \zeta_0(T) = \frac{F(X)}{F(X_1)} \cdot \eta_0(X_1, T) \quad (4.3)$$

This structural-viscosity model enables us to calculate the structural factor, $F(X)$, using MD simulations only; therefore, the size of the molecules that can be evaluated is extended. The viscosity value is needed only for one basic structure for acquiring the monomeric friction coefficient which can be obtained by the measurement of one sample, or through MD simulations to develop a completely virtual-type design tool. From a lubricant development point of view, this enables us to significantly reduce the number of samples of different molecular weights during the trial and error in the testing, and acquire an optimal monomer for future polymerization.

To further improve the accuracy of the model, the empirical values of X_c are calculated depending on the specific monomer structures. X_c is a critical parameter because it separates the rate of the viscosity increase. In the original Berry and Fox model, an empirical value is used:

$$X_c = 5.6 \times 10^{15} \quad (4.4)$$

In this chapter, the accuracy of X_c is further improved. In order to acquire X_c , we utilize a transition for the self-diffusion coefficient D_s . Similar to the transition for the viscosity, the

transport property of the self-diffusion coefficient also undergoes a transition with respect to X_c (M_c), which is found to be in the form of $D_s \sim M^{-1}$ for $X < X_c$, and $D_s \sim M^{-2.4}$ for $X \geq X_c$ [89]. As the equilibrium for D_s can be attained faster compared to that for the viscosity in the MD simulations, the evaluation of the self-diffusion coefficient, D_s , is used to further improve the accuracy of X_c . D_s can be calculated directly from the MD simulations because it is proportional to the slope of the mean-square displacement curve. The mean-square displacement (MSD) is defined as:

$$\text{MSD} = \langle (\mathbf{R}_{\text{cm}}(t) - \mathbf{R}_{\text{cm}}(0))^2 \rangle, \quad (4.5)$$

where $\mathbf{R}_{\text{cm}}(t)$ is the location of the molecule's center of the mass at time t , $\mathbf{R}_{\text{cm}}(0)$ is the location of the molecule's center of mass at time $t=0$.

Self-diffusion coefficient (D_s) is calculated as:

$$D_s = \lim_{t \rightarrow \infty} \frac{\text{MSD}}{6t}. \quad (4.6)$$

Figure 4.1 depicts the flow chart for the numerical approach.

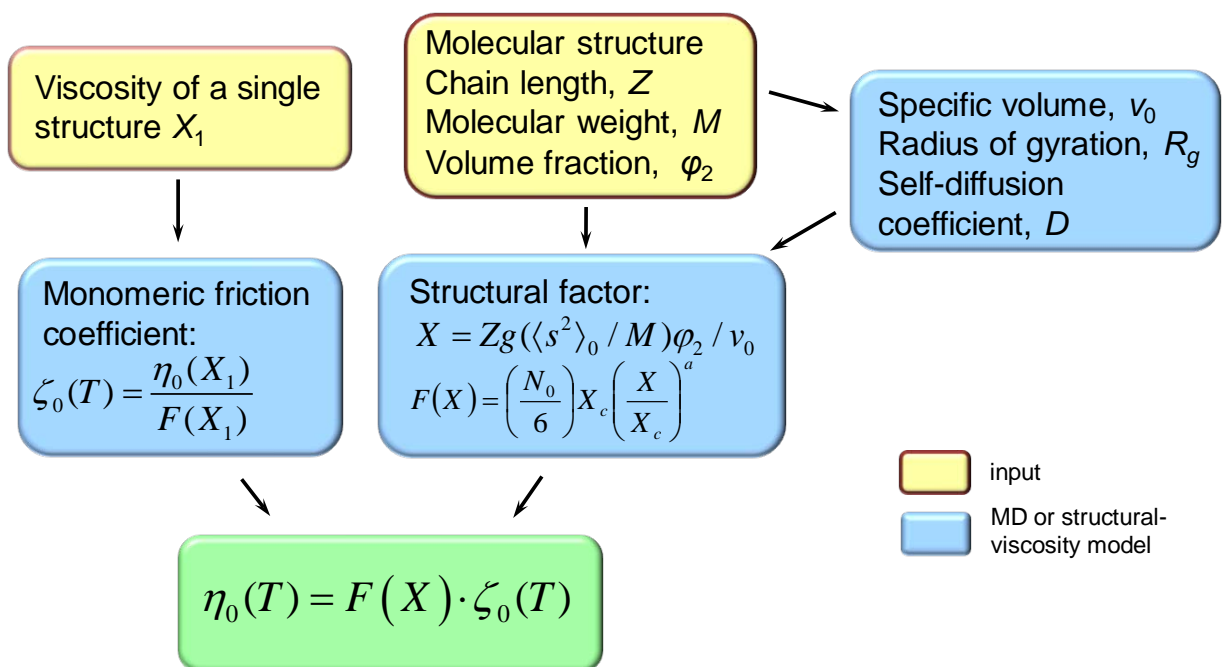


Figure 4.1 Flow chart for the structural-viscosity model.

4.3 Molecular Dynamics Simulation Setups for Polyethylene and Poly- α -olefin

The united atom (UA) method was used to generate the hydrocarbon structures. CH_3 , CH_2 and CH were each considered as pseudoatoms within the hydrocarbon chain with the interaction center at the nucleus of each carbon atom.

Two different structures, Polyethylene (PE), a linear chain polymer, and Poly- α -olefin (PAO), a branched polymer formed from 1-Decene, were used for evaluating the method. PAO, in particular, is an important group in the current synthetic base oil market. PAOs with chain lengths of $Z=2, 3, 4, 6, 10, 12, 16$ were studied.

Figure 4.2 shows a representative structure for PAO at $Z=6$. Viscosities of C_{76} ($Z=76$) and 1-Decene trimer ($Z=3$) are used as the known references for PE and PAO, respectively.

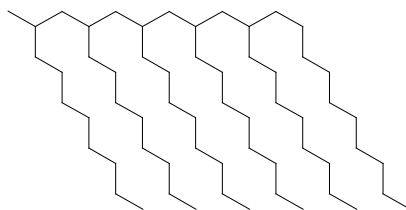


Figure 4.2 Structure of PAO at $Z=6$.

The force field used to describe the hydrocarbon molecules is the Transferable Potentials for Phase Equilibria (TraPPE) force field [25,90]. The stiff, fixed bond length was replaced by a harmonic potential to generate a fully flexible bond [51].

The system was first created and relaxed in the Materials Studios software to acquire the initial distribution of the pseudoatoms. The LAMMPS software [54,55] was used for the MD simulations and a timestep of 1 fs was applied in the simulations. The system was run for 100 ns in the MD simulations at the assigned temperature and pressure to acquire the parameters in the model.

4.4 Simulation Results

4.4.1 Validations of the Radius of Gyration Calculations

The accuracy of the mean squared radius of gyration (R_g) significantly affects the accuracy of our viscosity predictions. The radii of gyration of molecules of various sizes were

directly calculated using the MD simulations. Figure 4.3 shows the R_g calculation for Polyethylene.

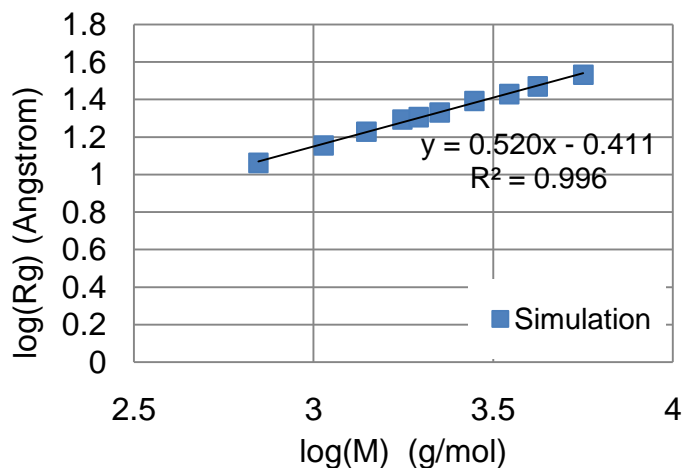


Figure 4.3 Radii of gyration calculated for Polyethylenes of various molecular weights, the values are plotted in the log scale, and curvefitted to acquire the exponent.

For Polyethylene (PE), our MD results depict the relationship as $R_g \sim M^{0.520}$, which agrees well with the literature results of $R_g \sim M^{0.5}$ [91]. As R_g has an exponential increase, extrapolation may be used for larger molecules for which the R_g values may not be directly calculated. For PAOs, an explicit topographical approach developed by Bonchev et. al [92] is used for validation. The Bonchev model [92], developed based on the work of Wiener [93] and Zimm and Stockmayer [94], relates a topological descriptor, the Wiener number, which is based on the distance matrix of the polymer graph, to the mean-square radius of gyration of that polymer. In the following equation, g , which represents the ratio between the mean square radius of gyration of the branch content to that of a linear chain, to be used in Equation 4.1, is calculated.

$$g = \frac{\langle S_{br}^2 \rangle_0}{\langle S_l^2 \rangle_0} = \frac{(B_B+1)^3 + a_B B_B (f_B - 2) [a_B^2 + (B_B+1)(2B_B+3a_B+1) + a_B (f_B-2)(B_B-1)(3a_B+B_B+1) + 3a_B^2 (f_B-3)]}{[a_B (f_B-2) B_B + B_B + 1]^3}, \quad (4.7)$$

where the variables are the number of branches, B_B , the branch functionality, f_B , and the ratio of the branch atomic length to the main chain spacer length, a_B . The variables are adapted to the structural parameters used throughout this chapter. As shown in Figure 4.4, g is calculated for molecules of different sizes, and the ratio with $g(\text{Trimer})$ is plotted with respect to the number of the pseudoatoms, N , since 1-Decene trimer is the selected structure with the previously obtained viscosity values. The values from the MD simulations and the Bonchev model agree well with each other.

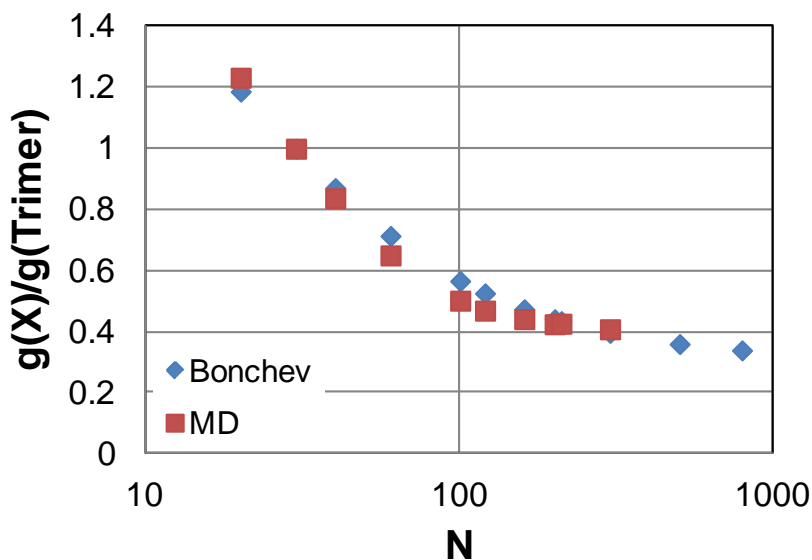


Figure 4.4 Calculated ratio of radii of gyration, g , normalized by that of 1-Decene trimer compared with that from the Bonchev model [92].

4.4.2 Estimations of the Critical Dimensional Factor, X_c

Figure 4.5 shows the calculated mean-square displacements (MSDs) for three PE structures. The self-diffusion coefficient is proportional to the slope of the curve as shown in Equation 4.6.

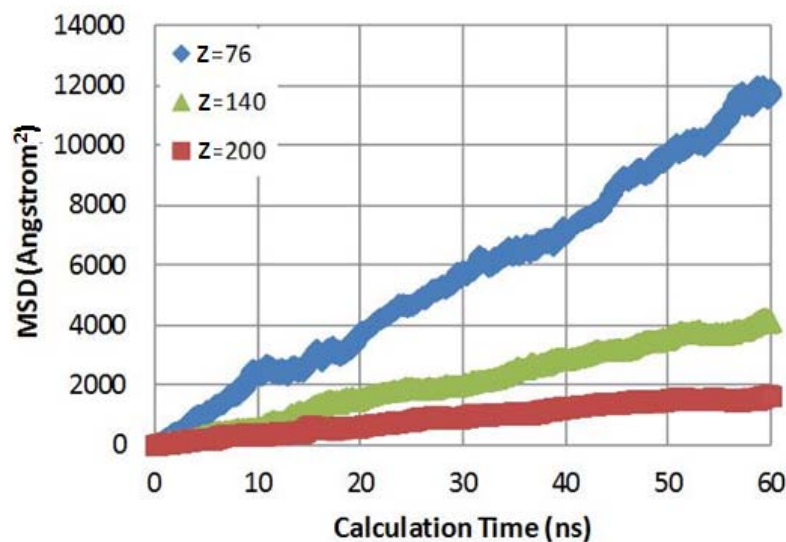


Figure 4.5 Calculated MSD for PE with $Z=76$, 140 and 200, respectively. The self-diffusion coefficient is proportional to the slope of the curve.

Figure 4.6 shows the calculated self-diffusion coefficients with respect to the size of the molecules for PE and PAO, respectively. The transition point was found at approximately $Z_c=178$ for PE, and this value is consistent with that reported by Harmandaris et. al [89]. No transition was observed for PAO, which is consistent with the estimated X_c from the original Berry and Fox model shown in Equation 4.4.

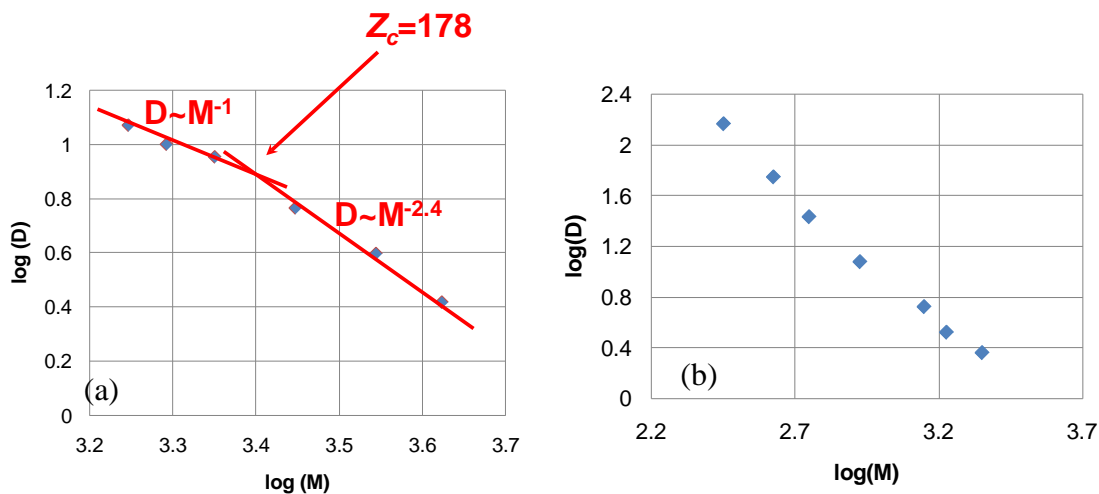


Figure 4.6 Calculated self-diffusion coefficient for (a) PE and (b) PAO vs. molecular weight. The values were plotted in the log scale in order to acquire the exponents. The transition point at $Z=178$ for PE is marked; no transition point was observed for PAO.

4.4.3 Viscosity Predictions and Comparisons with the Experimental Data

With the extrapolation of the radius of gyration, the viscosities of Polyethylene (PE) with different molecular weights were predicted, based on the viscosity of one structure (C_{76}), up to 84,000 g/mol at 0.1 MPa and 175 °C. The results agreed well with experimental data, as shown by the comparison in Figure 4.7. Using the calculated X_c from the MD simulations, we were able to predict viscosity with higher accuracy.

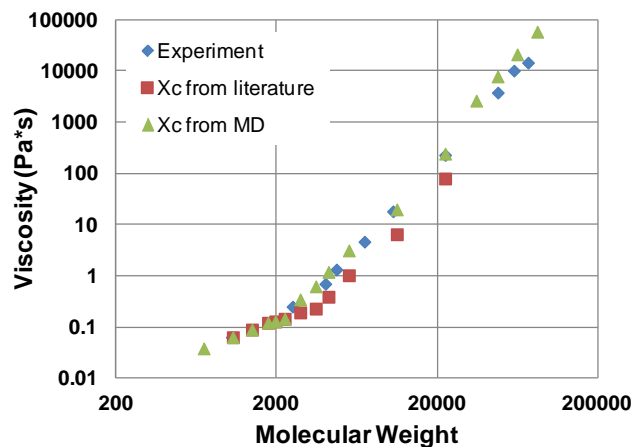


Figure 4.7 Zero-shear rate viscosity vs. molecular weight. The diamond symbol is from experimental measurements [95]; the triangle and rectangular symbols are predictions from the structural-viscosity model, one set uses the X_c from the MD simulations (triangle), while the other uses the X_c from the original Berry and Fox model (square).

Figure 4.8 shows the comparison of the zero-shear viscosity between the structural-viscosity model prediction and the experimental results for PAO at 0.1 MPa and temperatures of 40 and 100° C, respectively. The monomeric friction coefficient was calculated using the 1-Decene trimer ($Z=3$) case (the second data point in the plot). The two values agree reasonably well with each other up to PAO 100. PAOs in this size range are often used to develop mixtures for high quality, high VI synthetic lubricants.

In order to further improve the prediction for large molecules based on the small sized molecules, the value of a is modified using the first two datum points from KV40 (Kinematic viscosity at 40 °C), and first three points from KV100 (Kinematic viscosity at 100 °C). The previous value of 3.4 used in the original Berry and Fox model is often used as an estimate,

whereas for specific polymers at different temperatures, the value of a varies [96,97], particularly, with the increased long-chain branch content [96]. After curvefitting, $a=4.02$ at 40 °C, and $a=2.95$ at 100 °C were acquired, as shown in Figure 4.9. The prediction for PAO 100 after the modification agrees well with experimental results.

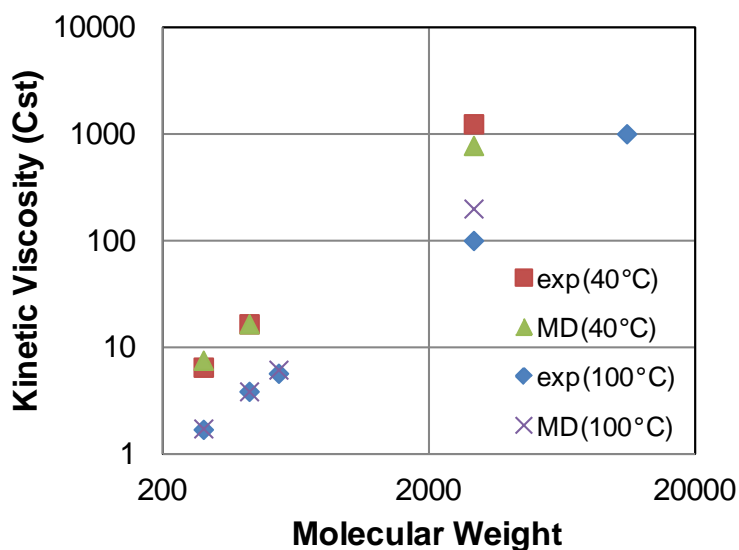


Figure 4.8 Zero-shear rate viscosity vs. molecular weight with $a=3.4$. Experimental measurements are from commercially available data from ExxonMobil [98].

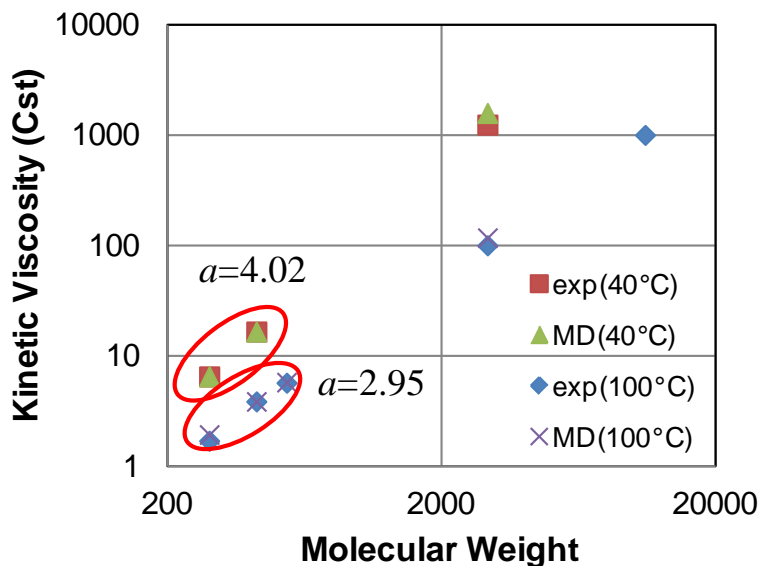


Figure 4.9 Comparison of zero-shear rate viscosity vs. molecular weight; the results from modeling were calculated with the modified a , fitted using two data points of KV40, and three data points of KV100 (circled in red), respectively.

4.5 Chapter Summary

This chapter reports a MD simulation-assisted viscosity calculation method that combines MD computations with the Berry and Fox type structural-viscosity model for predicting the viscosities of linear and branched polymer lubricants with molecular weights up to 10^5 .

- 1) The viscosities of Polyethylene (PE) and Poly- α -olefin (PAO) with different molecular weights, representing a linear polymer and a branched polymer, respectively, were predicted using the viscosity of a low molecular weight molecule (C_{76} for PE and PAO2-PAO6 for PAO). The results agreed well with experimental data, showing that the

modeling method could predict the viscosity high molecular weight molecules using the same monomers.

- 2) The exponent a should be a function of temperature and polymer structure, and its accurate value can be estimated from the slope of multiple low molecular weight liquids. This empirical constant was further modified for PAO based on the MD simulations depending on the individual polymer structures for increasing the accuracy of the model.
- 3) Self-diffusion coefficient can be directly calculated from MD simulations, and it was used to further increase the accuracy of the empirical value, X_c , which is a critical value where the exponent for the viscosity increase changes.

The proposed approach can be a useful method for the development and evaluation of synthetic lubricants because it enables us to build a long-chain polymer with a desired viscosity from a simple, low-weight molecule. It increases the range of the molecular structures that can be explored and reducing the cost of the initial lubricant development.

Chapter 5 Laser Surface Texturing for Reducing Adhesion at the Contact and Rubbing Interfaces

Surface texturing is a growing technology with which special patterns are intentionally created in an engineering surface. Suitably designed surface textures can have a positive impact on adhesion reduction and lubrication enhancement, leading to lower friction and improved performances at the contact interfaces. Laser ablation is a widely used method for surface texturing, which relies on short duration laser pulses with high energy densities that are fired on the surface to be textured. The drilling of materials like titanium is challenging owing to the strong effect of adhesion on drill bit life. The work reported in this chapter explores the possibility to use surface texture for adhesion control. Texture design, laser process design, and fixture setting are committed to manufacture textures on a set of drill bits. Drill test results demonstrate the positive effect of the surface textures on adhesion reductions and in turn, the tool life.

5.1 Introduction

Reducing friction and wear of surfaces under contact and rubbing has become increasingly important as industries strive to improve the energy efficiency in manufacturing processes and machine operations. This is particularly true for the case of cutting tools; high

friction at the cutting interface and wear of machining tools can lead to high cutting forces and frequent needs for cutting tool replacements.

The creation of surface textures in a micro-scale range has attracted wide attention because of the possibility of adhesion reduction and lubrication enhancement. Noticeable tribological improvements are evident if the textures are properly designed and fabricated [99-105]. For example, Tian et al. [99] machined undulating surface features onto titanium samples, in which the reduced friction and wear were attributed to the elimination of wear particles from the interface. Ceramic samples were textured using abrasive jet machining and excimer laser beam machining by Wakuda et al. [100]; a 20% friction reduction in a sliding line-contact interface was measured between ceramic samples and hardened steel cylinders. Geiger et al. [101] realized a significant increase in tool life when an excimer laser was used to micro-texture cold forging tools; the tool life increased by $45\% \pm 21\%$ with 10% of the tool area textured and $69\% \pm 17\%$ with 20% of the tool textured. Twelve and ten samples were used in the 10% and 20% coverage tests, respectively (two outliers of the 20% coverage results were discarded). Theories explaining the effects of surface texturing attribute the tribological benefits to the lubricant pockets created by the dimples. These pockets help to retain lubricant between the contacting parts and reduce side leakage, thereby decreasing friction. Additionally, the textured recesses serve as receptacles for the wear particles, preventing further surface damage via plowing.

Several works have been conducted to study the surface textures for cutting tool applications. Kawasegi et al. [106] generated channels with a spacing of 5 μm , a width of 800 nm, and a depth of 150 nm on the flutes near the cutting edge of drill bits with diameters of 0.5 mm. Drilling experiments were conducted with an aluminum alloy substrate. The results demonstrated a lower thrust for the textured drills when high feed rates were used. Considerable improvements were observed for textures with orientations perpendicular to the chip flow. In another study, Sugihara et al. [107] found reductions in chip adhesion and frictional force, resulting from banded nano/micro-textures in a face-milling experiment on aluminum alloy machining. It was hypothesized that an improvement in lubricant fluid retention was the source of the improvements in the anti-adhesive properties. Micro-dimples were created on mill face cutters and tested on mild steel by Lei et al. [108]. A finite element analysis was conducted on the textured inserts and no adverse effects were found; this conclusion was supported by experimental testing in which no catastrophic failures occurred. It was found that the textured surface reduced the machining forces by 10-30% and shortened the chip-tool contact length by 30%, which causes chip curling and facilitates chip removal. Neves et al. [109] utilized laser surface texturing on twist drills to improve the adhesion of a TiN coating. The results demonstrated longer tool life when drilling steel for the drills textured prior to the coating application.

Laser ablation is a widely used method for surface texturing and was first introduced by Etsion et al. [110,104]. This method relies on short duration laser pulses with high energy densities that are fired on the surface to be textured. The short pulse durations of the laser are utilized to minimize the thermal effects in the material surrounding the ablated zone [111]. Another important advantage of laser surface texturing over the other methods is the versatility of the texture geometries that can be created. This is crucial for the optimization of the surface texturing parameters for specific applications.

Northwestern has a Nd:YVO₄ picosecond laser micromachining system, as shown in Figure 5.1. Picosecond laser pulses (wavelength of 532 nm, pulse duration 8 of ps) travel from the laser to the substrate surface via the beam delivery system. The part to be textured is mounted on the precision positioning system, which has five degrees of freedom with a linear resolution of 10 nm and an axial resolution of 10⁻⁴ degrees. The laser can achieve a high resolution of the textures as a single laser pulse would generate a dimple of approximately 10 μm in diameter.

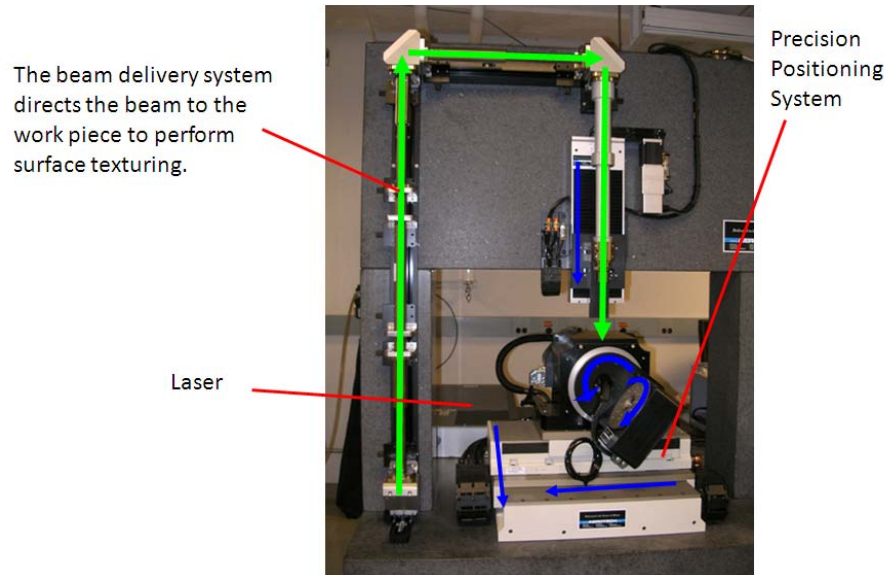


Figure 5.1 Nd:YVO₄ picosecond laser micro-machining system.

5.2 Design and Optimization of the Laser Texturing Process

Several variables may affect the outcome of the texture geometry and the quality of the laser textured surfaces including the laser scanning speed, pulse duration, pulse energy, focusing condition, number of passes, overlap value, etc. Therefore, it is necessary to study these parameters to determine their influences on the texture geometry and quality, to set a guideline for the laser process design.

A flat-bottom circular dimple, with a radius of 200 μm was selected (as shown in Figure 5.2) as the test geometry.

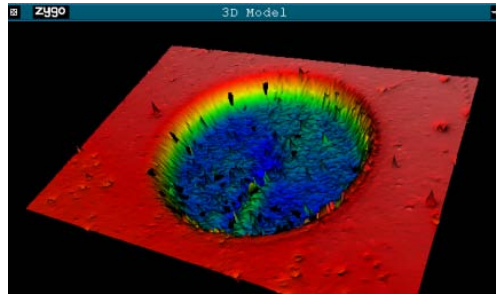


Figure 5.2 An image of a flat-bottom circular dimple acquired using a white-light interferometer.

Since a single pulse can only generate 10 μm diameter of a Gaussian distribution, in order to acquire a 200 μm radius dimple, numerous circles, each with a different radius, need to be made to cover the entire 200 μm radius, as shown in Figure 5.3.

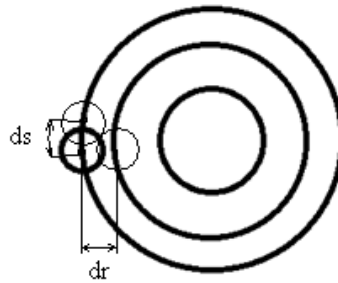


Figure 5.3 Illustration of the laser scanning. Between each firing of the pulse, the focus of the laser moves d_s along the scanning direction; and moves d_r along the radial direction after completing a full circle.

Focus tolerance is a parameter used to describe the variation of the focus distance within which the resulting depth variation of a texture is acceptable during the laser texturing process. Figure 5.4 depicts a test for flat-bottom dimples with a varying distance(z) between the workpiece and the laser lens. The axis is set such that at $z=0$, the maximum depth can be

acquired. We can see that for $\Delta d < 10\%$, we need $\Delta z < \pm 20 \mu\text{m}$; for $\Delta D < 25\%$, we need $\Delta Z < \pm 50 \mu\text{m}$; whereas for offsets more than $200 \mu\text{m}$, the texture quality would be considered unacceptable because the laser is severely out of focus. For depth variations between dimple to dimple, in most cases, we need a focus variation $< \pm 20 \mu\text{m}$ for an acceptable depth variation, whereas, $\Delta Z > \pm 50 \mu\text{m}$ would be usually considered unacceptable. The lens used for this test has a focused laser spot diameter of $10 \mu\text{m}$, which is the one that was mainly used.

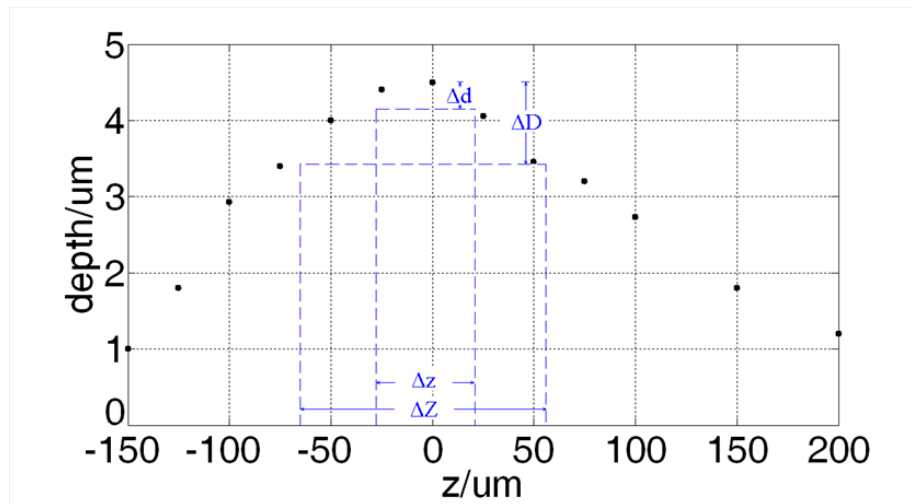


Figure 5.4 Depth variation with respect to the distance from the focal location.

Overlaps [112] in both the radial and scanning directions are the other significant controlling parameters that needs to be studied. As shown in Figure 5.3, $O = (1 - \frac{m}{d_w}) \times 100\%$, where m is the movement of the axis between two laser pulses, d_w is the effective working diameter of the laser beam; d_s the incremental movement in the scanning direction, and d_r the incremental movement in the radial direction. This process is necessary when the required texturing geometry is larger

than the beam diameter of 10 μm ; hence, an incremental relative movement between the laser head and the manufacturing part is needed along the texturing direction while multiple pulses are being fired. Optimal overlap is necessary to acquire a balance between the manufacturing speed and the bottom surface roughness of the texture. The effects of the number of passes, feed rate, and laser parameters such as the power and repetition rate have not yet been studied. In our test, they were set as pass No. =1, feed rate=1 mm/s, repetition rate = 500 KHz, and power = 1.00 W, respectively.

Figure 5.5 reveals that the depth increases as the overlap increases; for an overlap between 70-90%, the depth varies mostly from 1 to 3 μm . This would be the main depth range that can be achieved with one pass of the laser.

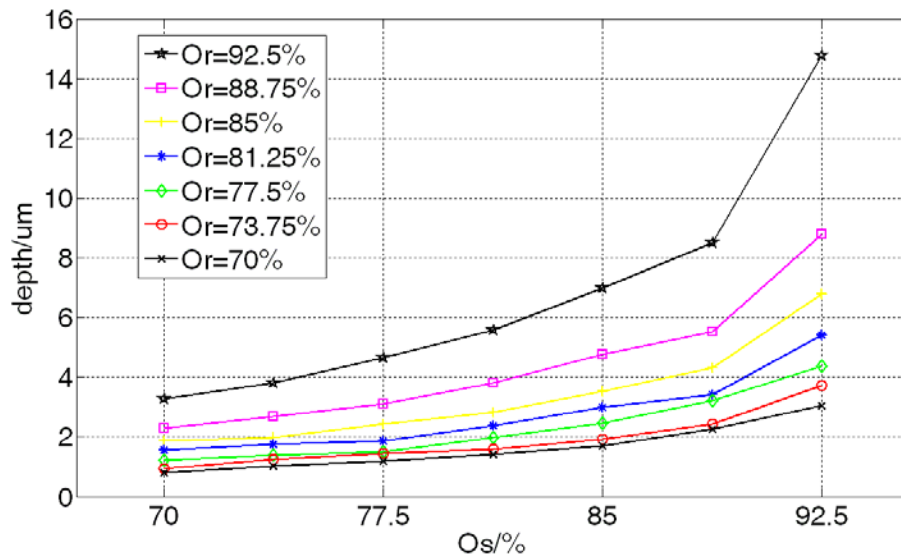


Figure 5.5 Effect of the overlap on the depth. O_r is the overlap along the radial direction, O_s is the overlap along the scanning direction.

Since laser ablation removes an absolute value of a material, the original surface roughness may be reflected on the resultant bottom surface RMS of the dimple. For our sample, the RMS of the surface before texturing was measured as $0.012\ \mu\text{m}$. Figure 5.6 suggests that the RMS of the dimple's bottom surface can be approximately $0.1\text{--}0.2\ \mu\text{m}$ for an overlap less than 80%, and could increase rapidly for an overlap greater than 85%.

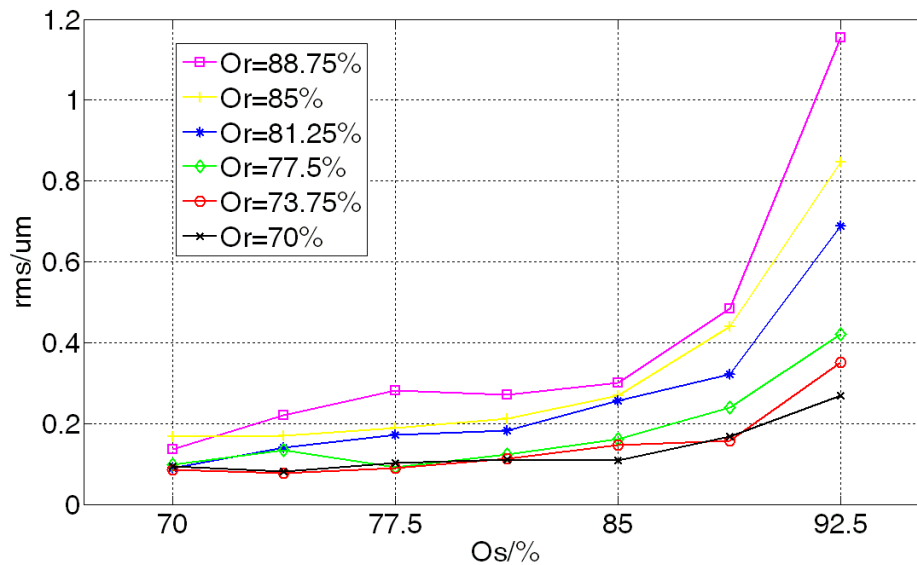


Figure 5.6 Effect of overlap on the bottom surface roughness. O_r is the overlap along the radial direction, O_s is the overlap along the scanning direction.

Owing to the complexity of the laser texturing process, as well as the fact that the relationships amongst the various parameters and their effects on the machining quality have not been fully understood, the above studies can act as guidelines for the process design of the desired texture geometry. An overlap of 85% is selected for the laser texturing process to achieve a good balance between productivity and the texture quality.

5.3 Fixture Design and Processing Method for Texturing Cylindrical Workpieces

Texturing cylindrical surfaces is a major challenge; rotational and translational movements of the axes are required while maintaining the workpiece within the focus tolerance during the texturing process. A fixture for precise rigid mounting, concentric to the axis of rotation of the positioning system, has been designed, made, and installed. This highly versatile system permits the precise positioning of cylindrical and other complex surfaces for an accurate texturing. A collet adapter system is used for mounting cylinders between 0.090" and 0.905", as shown in Figures 5.7 and 5.8. Rubber-flex collets were selected because they outperform conventional split-steel collets in terms of the gripping power, accuracy, and durability. Larger cylindrical workpieces with diameters between 0.98-2.75" can be mounted with the three-jaw chuck, as shown in Figure 5.9.

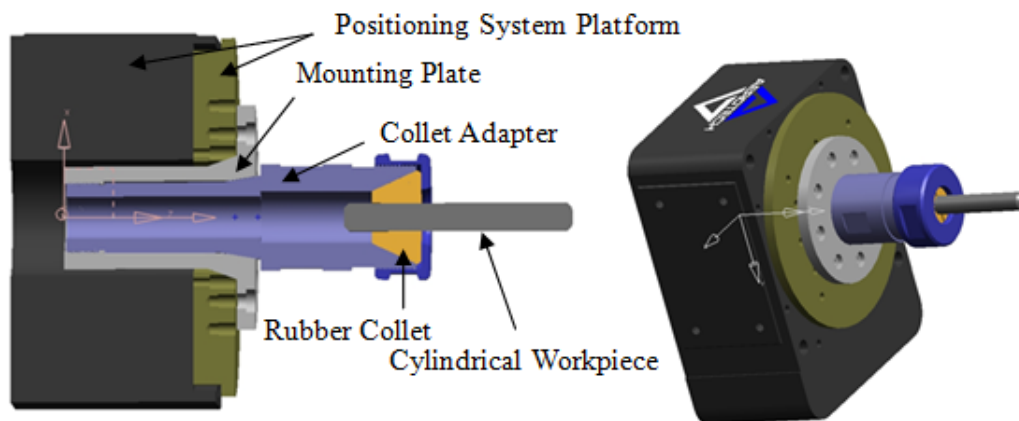


Figure 5.7 CAD model of the collet fixture for mounting cylindrical parts.



Figure 5.8 Photos of the collet system.



Figure 5.9 Photos of the 3-jaw chuck system.

The alignment of the system was tested as a benchmark for the actual texturing. The rubber collet system was used for testing the alignment with a sample cylinder radius of $5/16$ ". The sample itself was considered to be a perfect cylinder. Three positions (a-5 mm, b-20 mm, and c-35 mm from the edge of the collet nut, respectively,) were tested for the translational focus variation, as shown in Figure 5.10.

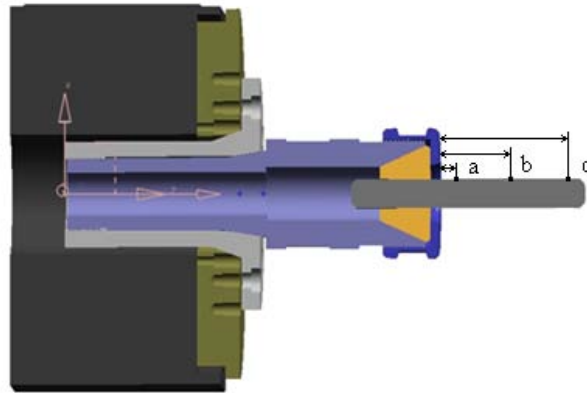


Figure 5.10 Positions for testing the translational focus variation.

For examining the rotational focus variation, dimples were created around the cylinder at positions a, b, and c, 45 degrees apart, as shown in Figure 5.11. The laser was initially focused at a-1 ($\Delta z=0$ for a-1).

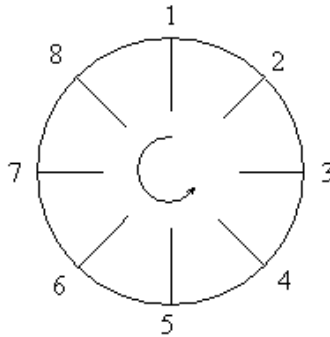


Figure 5.11 Test points for the rotational focus variation.

Figure 5.12 shows that the focus error at each position, a, b or c, is approximately $10\ \mu\text{m}$, which is within the focus tolerance. Compensation in the z direction may be necessary if the texturing length is long.

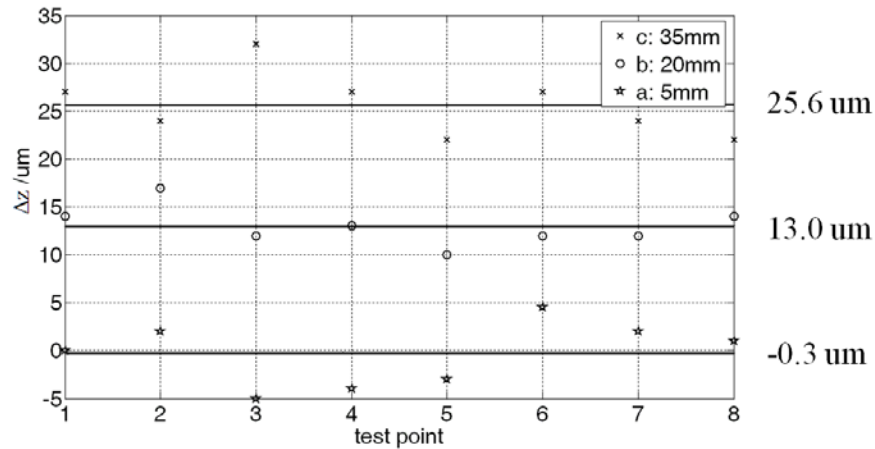


Figure 5.12 Focus variation at different test points

To maintain the focus of the laser during the texturing process along the cylindrical surface, a texturing scheme for rectangular grooves along a helical line should be designed.

Figure 5.13 shows the trajectory of the helix line, where $Helix_angle = \tan^{-1} \frac{2\pi r_m}{lead}$. For a helix l_h , $l_h \cdot \cos(Helix_angle)$, which is the lead, is achieved by a translational motion, $l_h \cdot \sin(Helix_angle)$, which also equals to $2\pi r_m$, is achieved by a rotational motion to form the helix length, and the necessary rotational angle should be $l \cdot \sin(Helix_angle) * \frac{360}{2\pi r}$. Then, a zigzag motion is used to accommodate the width of the groove. The texturing results are shown in Figure 5.14.

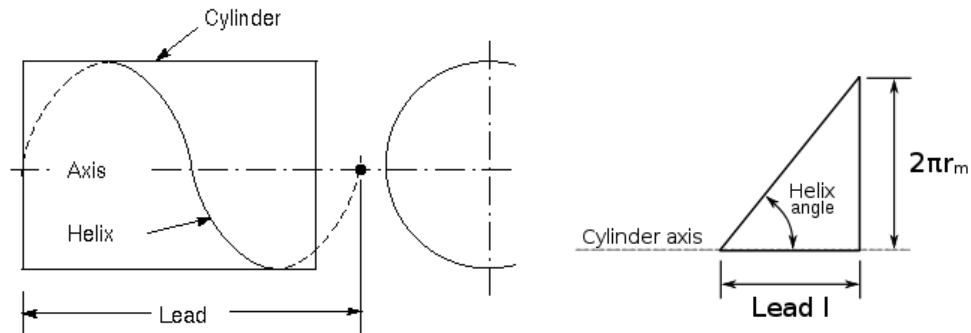


Figure 5.13 Trajectory of the helix line. The lead, l , is the amount travel along the translational direction with a 360 degrees rotation

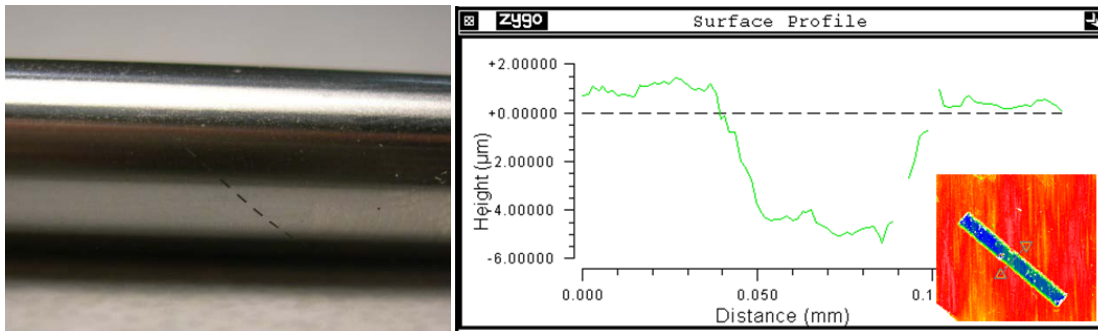


Figure 5.14 Photo of the textured rectangular grooves along the helix (left) and the measured cross section of the texture using a white-light interferometer (right).

5.4 Surface Texturing High-Speed Drill Bit Margins for Adhesion Reduction

5.4.1 Laser Surface Texturing Drill Bit Margins

This study aims to reduce chip adhesion in a drilling process and enhance the tool life by applying surface textures on suitable locations on the drill bits. The failure of cutting tools is particularly troublesome for cutting materials that involve strong adhesion, for example, titanium; cutting chips are often found near the tip of the drill bit, as shown in Figure 5.15. The needed

cutting force increases with the built-ups, and a failure occurs when the drilling forces reach a sufficiently high level. We strategically applied a group of micro-scale surface textures in the drill bit surfaces and examined the capability of the textures to control chip adhesion; thereby, enhancing the tool life.

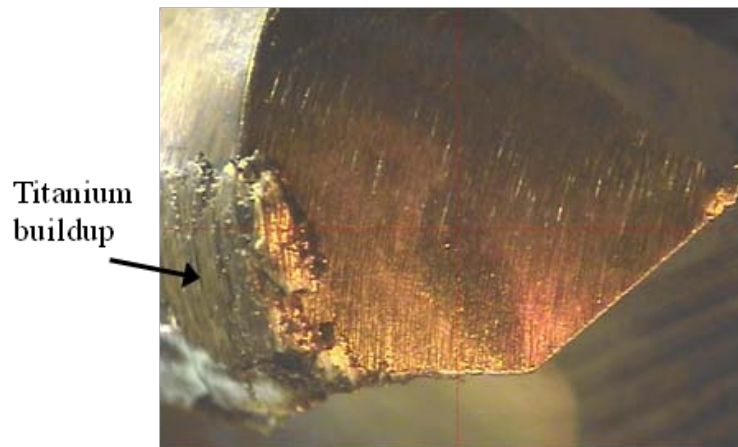


Figure 5.15 Example of titanium buildup on the drill margin and the cutting edge

Candidate surfaces for texturing the drill bits include the margins, lip relief, and flute, as shown in Figure 5.16. During drilling, frictional heating occurs on the drill margins due to contact with the wall of the newly made hole. Heat accumulation can cause chips to adhere to this area. Thus, surface textures have the potential to reduce such heat and adhesion; thereby improving the tool life. The lip relief is the surface that develops the most wear; hence, surface textures might help reduce friction and heat accumulation in this region. However, textures too close to the cutting edge may affect the mechanical strength of the drill, and wear could quickly wipe out any textures there. Although texturing the flutes could help in providing lubricant to

facilitate chip removal from the drill tip, chip adhesion is generally not problematic in this area. Therefore, this study focuses on texturing the margin surfaces of a drill bit. The results show that the choice is correct.

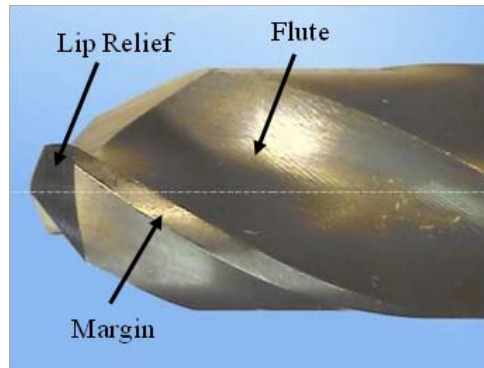


Figure 5.16 Candidate surfaces of a drill bit for texturing

The desired surface texture design is to make microscale shallow depressions, as shown in Figures 5.17 and 5.18, with lateral dimensions L and W which are one or two orders of magnitude larger than the depth dimension. These depressions can serve as micro reservoirs to retain lubricant. Previous work has shown that rectangular surface depressions arrayed in a triangular pattern (shown in Figure 5.17) result in the preferred beneficial lubrication condition [113-116]. Based on these results, the selected surface texture geometry was an array of rectangular depressions of $50\ \mu\text{m}$ in width, $450\ \mu\text{m}$ in length and $4\ \mu\text{m}$ in depth. The work by Wang and Zhu [117] has suggested that each depression has its zone of influence. For the purpose of lubrication, the effects of neighboring influence zones are summed together. Due to the nature of cutting, lubrication is generally ineffective at the tooling-workpiece interface; the

function of the depression is mainly for adhesion reduction through the introduction of a different interfacial condition along the track of the relative motion of the chip flow so that the mating surfaces do not continuously experience the same metal-metal rubbing. Therefore, an overlap of the influence zones along the chip path should be created to intersect the relative motion direction.

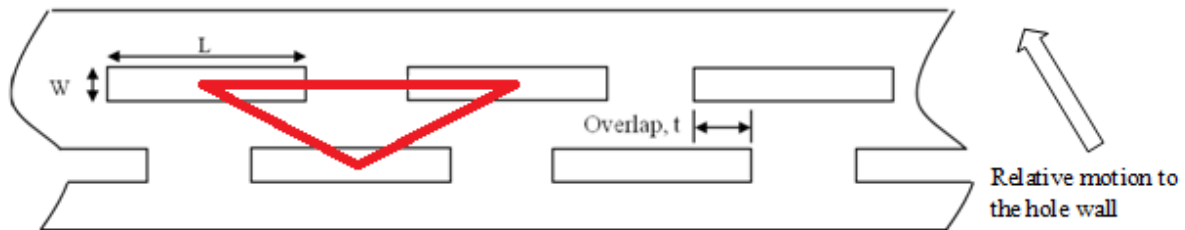


Figure 5.17 Texture design of a triangular distribution on the margin. A section of the margin is plotted, the rectangles are the location of the textures with dimensions L and W .

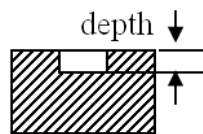


Figure 5.18 Cross section of the texture design. A flat bottom shape is used.

Figure 5.19 shows an estimate of the fluid pressure around the rectangular depressions, where the relative motion perpendicular to the texture length is analyzed. The length of the pressurized zone is almost the same as that of the rectangles. Therefore, for cutting, the influence zone can simply be the same shape as the depressions, and the overlap, t , can be defined based on the texture shapes, as indicated in Figure 5.17. The best distribution pattern for the most

effective overlap is the triangular distribution, shown in Figure 5.17. The textures are designed so that they are deep and sufficiently large to store lubricant but shallow and sufficiently small to not induce a reduction in cutter strength.

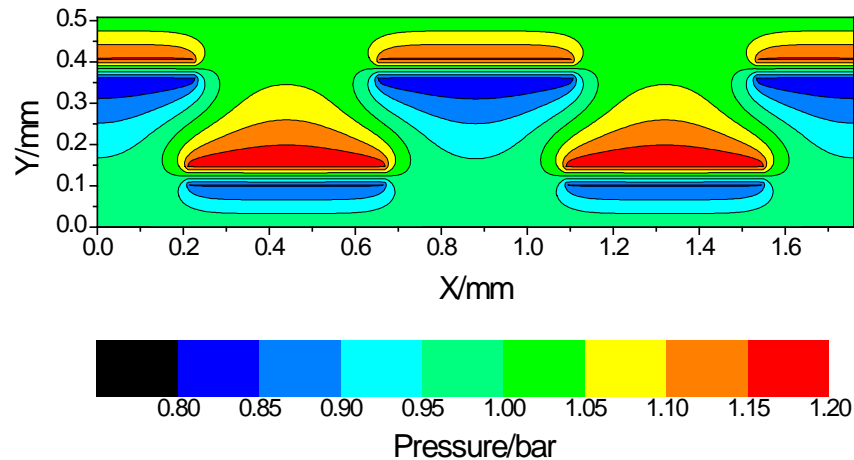


Figure 5.19 Estimate of the fluid pressure around the rectangular depressions.

The designs of two different coverage areas, approximately 10% and 20% of the margin surface area, were accomplished. Using the laser micro-machining system described previously, high strength steel drill bits (Dormer A920, 7.9 mm diameter by 40.6 mm flute, 76.2 mm overall length) were textured as depicted in Figure 5.20. After texturing, the samples were cleaned by sliding a cloth along the textured margins.

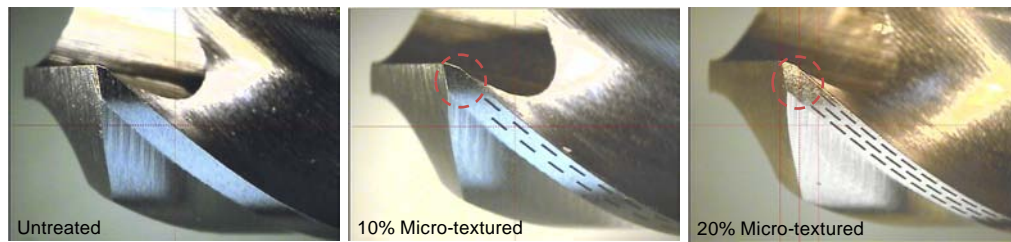


Figure 5.20 Comparison of the drills: untreated, 10% of the margins micro-textured, and 20% of the margins micro-textured. Each rectangular depression is $50\ \mu\text{m}$ wide, $450\ \mu\text{m}$ long and $4\ \mu\text{m}$ deep. Note that the tip of the margin, shown in the circle, was not textured.

The texture depth of each processed drill was measured at ten different spots (5 on each margin) using the ZygoNewView™ 7300 3D optical surface profiler. Figure 5.21 presents the resultant average depths and standard deviations of the textures for the 10% and 20% textured drills. While a variability in the texture depth was evident, the deviations were considered acceptable for this application.

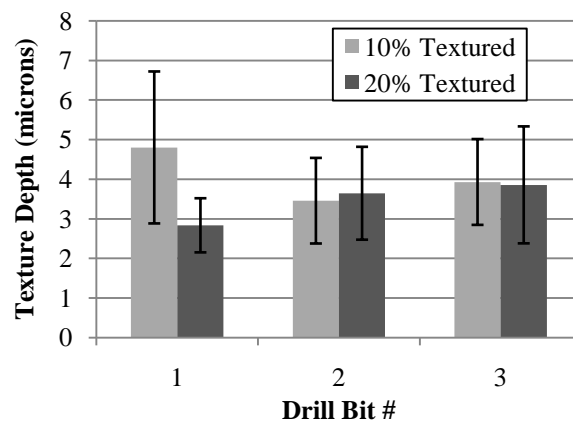


Figure 5.21 Average texture depth of each laser textured drill bit.

5.4.2 Drilling Test Results and Discussions

A series of drilling tests were run at Boeing, as a collaborative work, in which three drills of each type were used to drill a set of holes at a constant feed of 24.9 mm per min and a constant speed of 245 revolutions per min. These parameters were selected to produce work material adherence to the baseline drills at a reasonable rate, so that the impact due to the texturing could easily be identified. The drills were first dipped in a Boelube 70104 lubricant for 15 s, after which a hole was drilled through a 9.5 mm thick plate of annealed titanium 6Al-4V. Visual inspections of the drill bit were performed for every 10-15 holes. The holes were drilled using each drill, until a failure occurred. A failure was determined when the cutter was no longer able to drill through the titanium sheet.

The adhesion of a larger area of the workpiece on the drill is directly linked to tool failures. Baseline drill bits #1, #2, and #3 failed at 30, 52, and 60 holes, respectively. The drill bits that have 10% of the margin area textured performed better, with the first drill failing at 45 holes and the remaining two drills failing at 70 and 78 holes, respectively. Drill bits with a 20% textured area failed at holes 72, 30, and 71.

Figure 5.22 illustrates the tool life comparison for the three drill types; the average number of holes produced for the untreated, 10% textured, and 20% textured drills were 47.3, 64.3, and 57.7 holes, respectively.

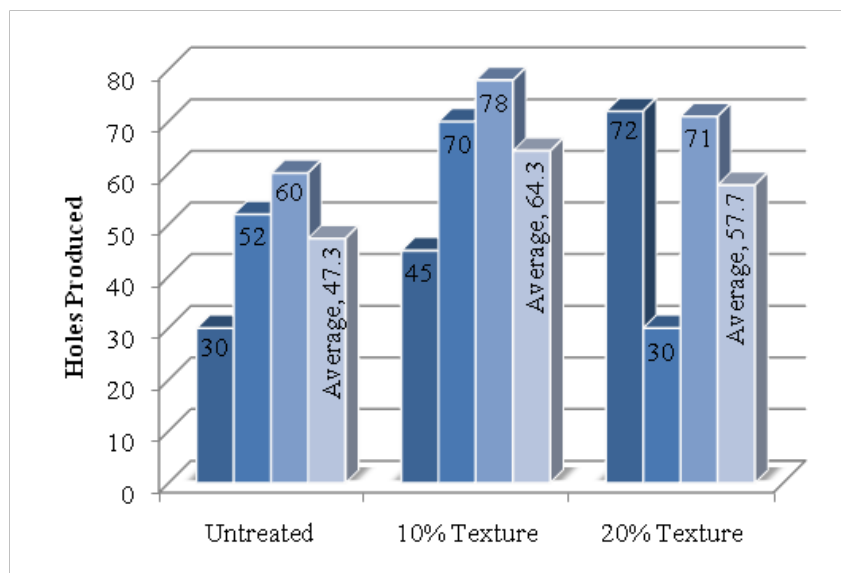


Figure 5.22 Tool life comparison for the untreated, 10%, and 20% textured area drills, respectively.

Figure 5.23 shows an example of the resulting images captured during the test of the baseline drill bit #2 after 0, 30, and 52 holes had been drilled. A small amount of chip adhesion was present after 30 holes were drilled. After the failure at 52 holes, a substantial amount of chip adhesion was visible, indicating that the failure mechanism was the titanium buildup on the drill margins. The images taken at failure or after 60 holes for baseline, 10% textured, and 20% textured drill bits are provided in Figures 5.24-5.26. In all the cases, the textured drill bits exhibited significantly less titanium buildup than the baseline non-textured drills. Much more buildup is visible at failure, again confirming the failure mechanism of chip adhesion. These images indicate that the titanium build-up on the drill margins was the dominant failure mode of the drills; they also reveal a correlation between a large titanium buildup on the margin and the

drilling torque above 7 N·m with a peak temperature exceeding 475 °C. The circled area, where no textures were made, shows continuance of the material build-up, and may have contributed to the final failure of the drill bits.

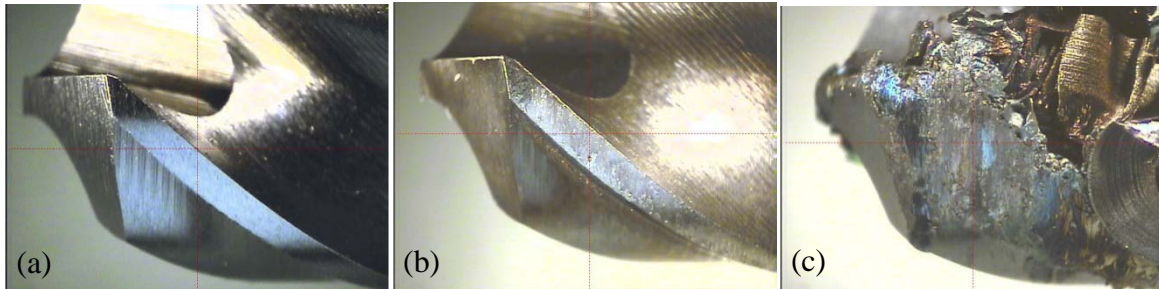


Figure 5.23 Images of the baseline drill #2 after (a) 0 holes drilled, (b) 30 holes drilled, and (c) 52 holes drilled (Images taken after the drilling of 10, 20, 40 and 52 holes are omitted here due to space concerns).



Figure 5.24 Baseline drills at failure (a) #1 after 30 holes drilled, (b) #2 after 52 holes drilled, and (c) #3 after 60 holes drilled.



Figure 5.25 10% textured drills at failure (a) #1 after 45 holes drilled, (b) #2 after 60 holes drilled, and (c) #3 after 60 holes drilled. Circles indicate the tips of the drill bit margin where no textures were made.

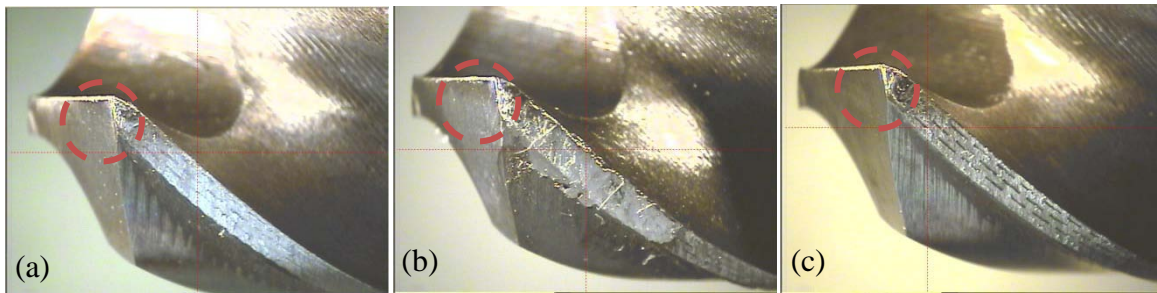


Figure 5.26 20% textured area at failure (a) #1 after 60 holes drilled, (b) #2 after 30 holes drilled, and (c) #3 after 60 holes drilled. Circles indicate the tips of the drill bit margin where no textures were made.

In addition to surface inspections, measurements of the drill diameter near the tip were performed for every 10-15 holes to assess the thickness of the titanium material adhering to the drill margins. It was found that in some instances, an inter-hole shedding occurred, where the measured chip buildup was found to be thinner than that in the previous measurement. For untextured drills, two of nine sequential comparisons, or 22%, showed less build-up than in the previous drill condition examination, while for micro-textured drills, eight of 17 comparisons, or 47%, show less build-up than in the previous drill condition check. The improvement in inter-hole shedding observed for the textured drills indicates that the titanium chip adhesion is notably reduced by the texture features.

The results from this study reveal that creating textures on the margins of drill bits is a promising method for reducing adhesion and enhancing drill life. Rectangular texture features with an overlapping triangular distribution pattern appear to be promising texture designs.

5.5 Chapter Summary

This chapter reports the development of a laser texturing process and tooling for texturing cylindrical surfaces. Consistency in manufacturing the surface textures was achieved. This process was applied for surface texturing drill bits to reduce chip adhesion and enhance drill life.

- 1) Three drill bit groups were textured and tested, which are non-textured drills, and those with 10% and 20% of the drill margin surface textured. A larger area of workpiece adhesion on the drill bit margin is directly linked to tool failure. Textured drill bits were found to exhibit less adhesion and improved the shedding of the adhered chips hole-to-hole.
- 2) The shedding of the build-up ultimately led to a reduction in chip adhesion and therefore, extended the tool life. While 100% of non-textured drills failed at or before 60 holes were drilled, both of the texture designs tested (with 10% and 20% of the drill margin surface area textured) only resulted in a 33% failure when 60 holes were drilled.
- 3) No discernible difference was found between the two texture designs in terms of the drill life at the tested conditions.

The results from this portion of the study reveal that creating textures on the margins of drill bits is a promising method for these purposes. Rectangular texture features with a triangular distribution pattern appear to be promising texture designs.

Chapter 6 Understanding the Hydrodynamics of Surface Textures

Surface textures affect the lubrication at the interface of the two components under contact and their relative motion. Although several factors are involved in the characterization of the interface, the hydrodynamics of the surface micro geometry is among the key concerns. This chapter aims to explore the texture effect on the hydrodynamics based on textures only, without the coupled influence of a macroscopic wedge. A model for a flat-flat interface formed by a textured and an untextured surface is developed based on the revised Payvar-Salant mass-conservation approach that focuses on the texture design only for understanding the effects of the texture geometry on the hydrodynamic pressure generation and load capacity under different working conditions.

Single texture features are analyzed to explore the optimal geometry for a load capacity improvement. An empirical relationship is formulated to correlate the load capacity with the texture size, shape, and depth. Multiple texture features are studied for the interaction of the hydrodynamics of the features, for further optimizing the texture performance. The design limit after which the texture no longer generates a positive loading effect is determined. The magnitude of the load supporting the effect of the surface textures was also studied with a combination of the initial surface roughness. A maximum allowed initial roughness value for the texture application was explored.

6.1 Introduction

Over the past decades, experimental studies have shown that suitable surface modifications by textures can have positive effects, including friction reduction, load capacity increase, wear prevention, tool life increase, etc. [118-120]. Significant efforts have been made on modeling surface texturing, which may be categorized into three types: the application of the Reynolds equation with the Reynolds boundary conditions, the implementation of a mass-conservation model of the lubricant flows, and the usage of computational fluid dynamics (CFD) models to solve the Navier-Stokes equation. For applications of the Reynolds model, the algorithm is well-developed, and the results can be achieved in a relatively short duration [121-123,116,124,125]; the models often involve thermal and/or elastic effects [126,127]. The mass-conservation model is a correction of the Reynolds model for flow continuity, where a striated flow is considered. It attempts a better description of the cavitation effect that is defined as the disruption of a continuous liquid phase by the emergence of a gas or vapor [128]. Since the beginning of the application of the JFO condition [129,130], several researchers have tried to improve the algorithm and the convergence of the computation using the finite difference method [115-118]. Models based on the finite element method have also been developed [119, 120]. Fowell et al. [121] identified the inlet suction and entrapment as the two mechanisms for the hydrodynamic lubrication of the textured bearings by means of an analytical solution of a 2D geometry. Recent studies, both from the numerical [122] and experimental [123] points of view,

have shown that the mass-conservation model generates a better prediction than the Reynolds model. Further, with the developments in computational power and open source CFD codes, more effort has been focused on the usage of the CFD for modeling the effects of the surface textures because it can take into account more physical phenomena such as fluid inertia, turbulence, etc. However, owing to the costs of a significant computational time increase, CFD studies, currently, mainly focus on the analyses of single pockets [124-127].

This study intends to understand the texture physics with a mass-conservation model of a flat-flat sliding interface, where the surface texture is the only source of pressure generation. We attempt to optimize the texture geometry for the maximum load capacity, and to study the effects of different boundary conditions on the optimal texture size with respect to different applications. The combined effect texture and the machined surface roughness is also explored.

6.2 Numerical Model of a Flat-Flat Interface with Textures

A schematic of the single dimple flat-flat model is presented in Figure 6.1. It consists of an infinitely long untextured sliding top surface and a textured but nominally flat bottom surface. The nominally flat-flat interface is utilized to view the effect of the surface textures only because the macroscopic wedge effects are all excluded. The top surface slides with a constant velocity, U , in the presence of a viscous lubricant with viscosity, η . The viscous flow between the two surfaces produces the hydrodynamic pressure. The bottom surface is attached to a rigid foundation. The viscous lubricant has a local thickness of $h(x,y)$, while the clearance between the

nontextured area and the top plate is maintained constant at H_{ref} . The texture analyses focus on the load capacity. Finally, to benefit the motion in both sliding directions, symmetric texture geometries and distributions are preferred.

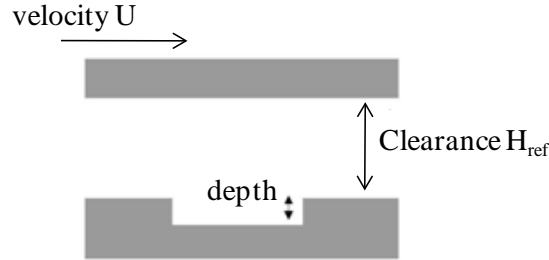


Figure 6.1 A schematic of a nominally flat-flat interface with a single texture. The textured (bottom) surface is fixed while the top surface is sliding with velocity U .

The model used for the texture analysis is the steady-state Payvar-Salant mass-conservation model [118], with the non-dimensionalized form as follows:

$$\frac{\partial}{\partial X} \left(H^3 \frac{\partial F \phi}{\partial X} \right) + \frac{\partial}{\partial Y} \left(H^3 \frac{\partial F \phi}{\partial Y} \right) = \frac{6\eta LU}{H_{ref}^2 (p_0 - p_c)} \frac{\partial \left([1 + (1-F)\phi]^* H \right)}{\partial X} \quad (6.1)$$

where $H = \frac{h}{H_{ref}}$, $X = \frac{x}{L}$, $Y = \frac{y}{L}$, $F\phi = (p - p_c) / (p_0 - p_c)$, $\rho / \rho_c = 1 + (1-F)\phi$,

$$F = \begin{cases} 1 & \text{for } \phi \geq 0 \text{ (full film region)} \\ 0 & \text{for } \phi < 0 \text{ (cavitation region)} \end{cases}$$

In Equation 6.1, x and y are the Cartesian coordinates, L is the length and width of the square solution domain, X and Y are the non-dimensionalized coordinates, p is the local pressure, p_0 is the ambient pressure, p_c is the cavitation pressure, η is the dynamic viscosity of the fluid, U is the

relative speed between the mating surfaces, h is the local thickness of the film, H_{ref} is the reference film thickness that is set as the clearance, F is the cavitation index with ϕ as a type of non-dimensionalized pressure, ρ is the density of the lubricant, and ρ_c is the averaged density in the cavitation region, where the lubricant is considered to be a mixture of fluid and gas (or air).

$\frac{6\eta LU}{H_{ref}^2(p_0 - p_c)}$ is the non-dimensionalized working condition. For the baseline analysis,

the parameters are set at $U=1$ m/s, $\eta=35$ cp, $H_{ref}=2$ μ m, and $L=1$ mm. The ambient pressure p_0 is set as the atmospheric pressure of 1 bar, and the cavitation pressure p_c is set as zero in this study.

The mesh grid size is set as 201*201. The elastic deformation of the surfaces is not considered because the pressure generated by the flat-flat sliding interface is low.

Figure 6.2 shows a group of such textured features, and N_1 is the number of dimples along the perpendicular direction, and N_2 is the number of dimples along the flow direction. Based on the consideration of edge-effect minimization, three sets of boundary conditions are employed (Figure 6.3): B.C. 1: For $N_1 \ll N_2$, the boundary conditions are defined as periodic in the flow direction and prescribed in the perpendicular direction; B.C. 2: For N_1 and N_2 of similar magnitudes, the boundary conditions are considered to be prescribed in both the directions; B.C. 3: For $N_1 \gg N_2$, the boundary conditions are set as prescribed in the flow direction and periodic in the perpendicular direction.

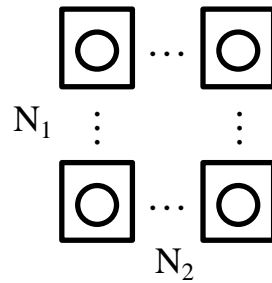


Figure 6.2 Distribution of the textured features. Square indicates the basic cell and the calculation domain for each dimple; circle indicates the dimple. N_1 is the number of dimples along the perpendicular direction, and N_2 is the number of dimples along the flow direction.

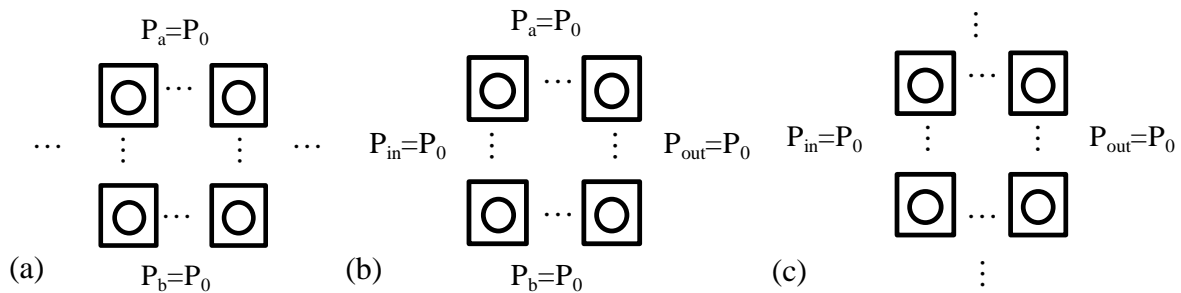


Figure 6.3 Three different boundary condition treatments corresponding to (a) B.C.1: periodic in the flow direction, prescribed in the perpendicular direction, (b) B.C.2: prescribed in both the directions, and (c) B.C.3: prescribed in the flow direction, periodic in the perpendicular direction.

The basic cell of a single texture is analyzed with the B.C.1. As shown in Figures 6.4 and 6.5, the top geometries of the texture features studied are rectangular (rect) or elliptical (ellip) in shape, and the cross section shapes are flat-bottom (flat), arc (cos) that is characterized by a cosine function, and triangular shapes. For triangular shapes, three different shapes were considered with the cross points at the center (triC), left corner (triL), and right corner (triR), respectively. The texture parameters, A , B , and the texture depth, d , are studied; A and B are the two axes for the elliptical dimples, or the width and length for the rectangular dimples,

respectively. Multiple textures on the surface are analyzed with all the three B.C.s, and the effects of N_1 and N_2 on the texture size are also explored. The average generated pressure, P_{avg} , shown below, is used for pressure evaluations.

$$P_{avg} = \frac{Load}{L^2} = \frac{\iint p(x, y) dx dy}{L^2} - p_0 \quad (6.2)$$

Because the ambient pressure p_0 has already been subtracted, $P_{avg} > 0$ indicates a positive pressure gained from a texture design, whereas on the other hand, $P_{avg} < 0$ suggests a negative texture effect.

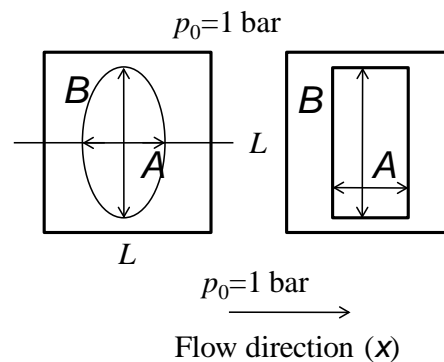


Figure 6.4 Parameters for single texture design for the elliptical (ellip) and rectangular (rect) dimples. A is the width along the flow direction, and B is the width along the perpendicular direction, respectively.

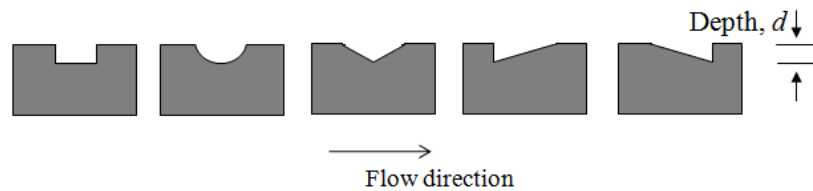


Figure 6.5 Cross sections studied for a single texture design, which are flat-bottom (flat), arc (cos), triangular center (triC), triangular left (triL), and triangular right (triR), respectively, from left to right.

6.3 Numerical Results and Discussions

6.3.1 Design and Optimization of a Single Texture

In the single texture analysis subjected to B.C.1, the geometric parameters are the focus. Figure 6.6 indicates that for the geometric parameter B/L , regardless of the texture geometry, P_{avg} increases as B/L increases. In future analysis, B/L will be set at 0.9 to avoid the side flow and maintain the material strength between textures. This is owing to the fact that in the current setup, the textures always generate a positive effect; therefore, the non-textured area in the direction perpendicular to the flow would not offer a load capacity improvement.

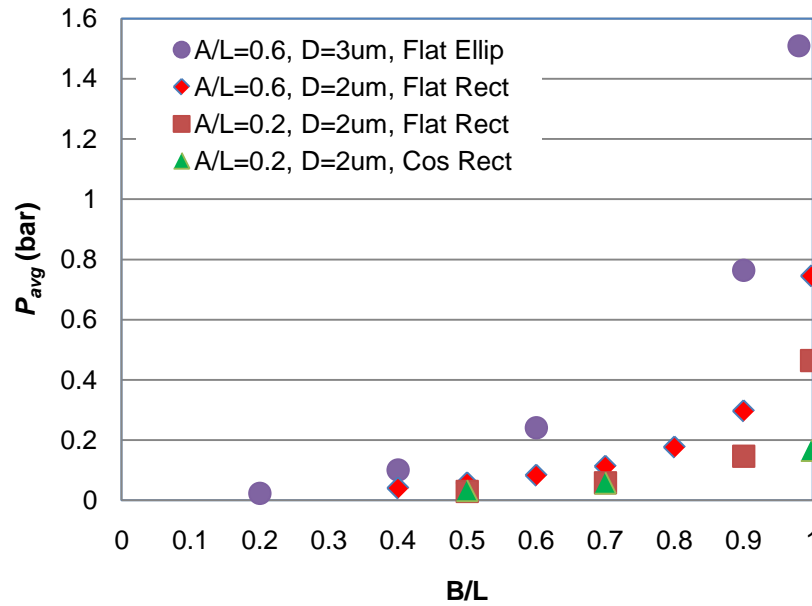


Figure 6.6 Effect of B/L on P_{avg} for elliptical, flat-bottom dimple with $A/L=0.6$, depth= $3\ \mu\text{m}$ (circle), rectangular, flat-bottom dimple with $A/L=0.6$, depth= $2\ \mu\text{m}$ (diamond), rectangular, flat-bottom dimple with $A/L=0.2$, depth= $2\ \mu\text{m}$ (square), rectangular, arc-bottom dimple with $A/L=0.2$, depth= $2\ \mu\text{m}$ (triangle).

For the depth, from Figure 6.7, regardless of the texture top geometry, cross section, or size, a non-dimensionalized empirical equation was acquired, as shown below:

$$P = F(D) = C_1 \cdot \frac{D^a}{e^{(C_2 \cdot D^b)} - 1}, \quad (6.3a)$$

with non-dimensionalized $P=P_{avg}/p_0$, and $D=d/H_{ref}$ based on the calculated results, C_1 , C_2 , a , and b are the fitted parameters.

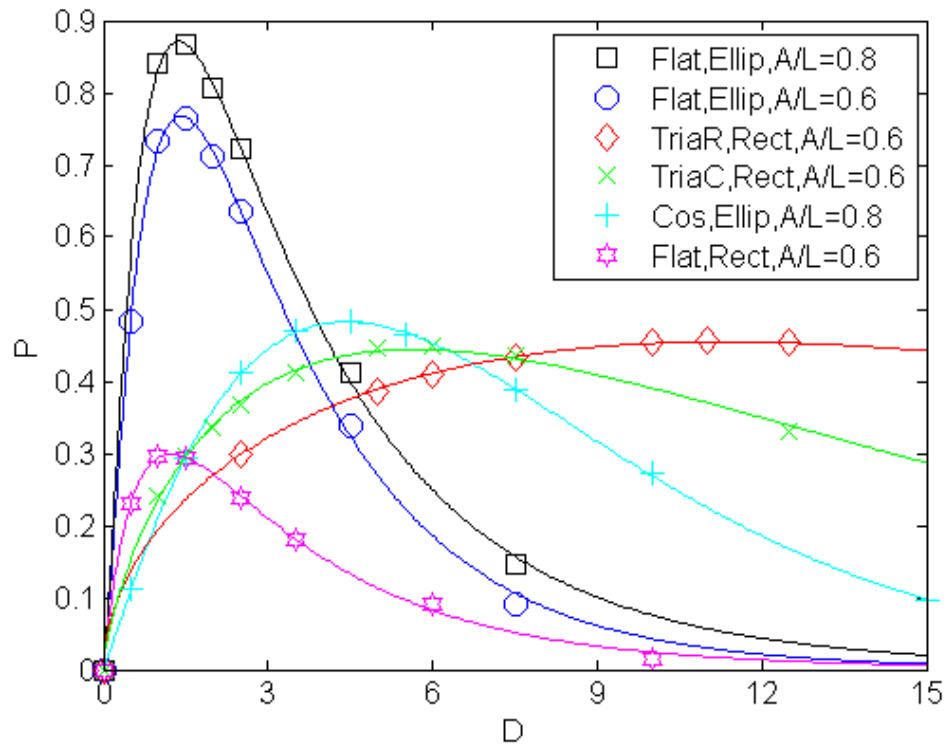


Figure 6.7 Effect of depth $D=d/H_{ref}$ on pressure $P=P_{avg}/p_0$ for various geometries. $B/L=0.9$. The symbols are from the simulations, and the curves are from the fitted Equation 6.3a. The flat-bottom elliptical dimple generated the highest pressure.

The symbols shown in Figure 6.7 are the numerical results, whereas the lines are the fitted curves using Equation 6.3a. We can see that they match well with $R>0.999$ for all the cases. The high peak values are from the flat-bottom elliptical dimple, suggesting a possible optimal texture geometry. Further study into flat-bottom elliptical dimples of different A/L parameters show that the pressure-depth equation, Equation 6.3a can be further decomposed into the following with C_1 now a function of A/L .

$$P = F(A/L) \cdot G(D) = F(A/L) \cdot \frac{D^a}{e^{(C_2 \cdot D^b)} - 1} \quad (6.3b)$$

The result of the above equation is shown in Figure 6.8, with $R > 0.998$, where F and G are functions of A/L and D as the only variables, respectively. The symbols are from the simulations, and the curve is obtained by curvefitting Equation 6.3a with a unique C_1 , or $F(A/L)$, for each A/L .

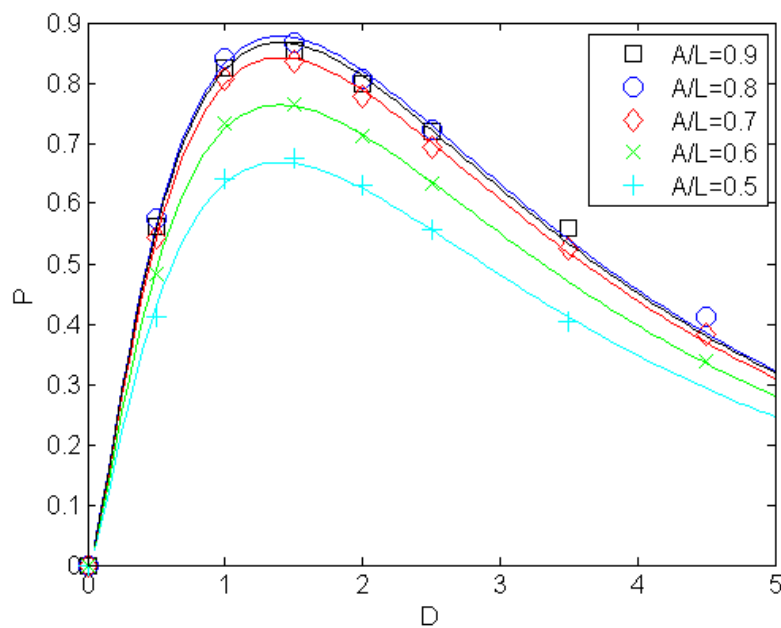


Figure 6.8 Effect of $D=d/H_{ref}$ on pressure $P=P_{avg}/p_0$ for different values of A/L of the flat-bottom elliptical dimple. $B/L=0.9$. The symbols are from the simulation, and the curve are from fitted Equation 6.3a with a unique C_1 for each A/L . As C_1 is unique for each A/L , it can be written as a function of A/L , $F(A/L)$.

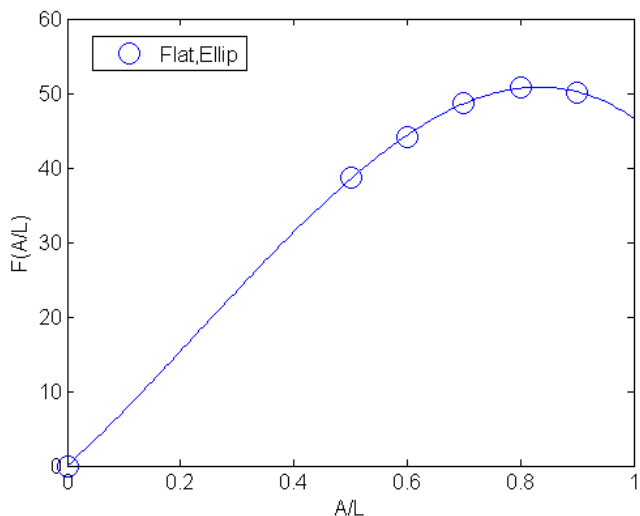


Figure 6.9 Third order polynomial form for $F(A/L)$ vs. A/L for the flat-bottom elliptical dimple, $B/L=0.9$. The symbols are from the simulation, and the curve is fitted to a third order polynomial.

In order to obtain the form of function $F(A/L)$, a third-order polynomial is used, as shown in Figure 6.9. The third-order polynomial relationship between P and A/L is further validated with flat-bottom rectangular dimples and cosine-bottom elliptical dimples with $R>0.993$ and $R>0.999$ for both the cases, respectively, as shown in Figure 6.10.

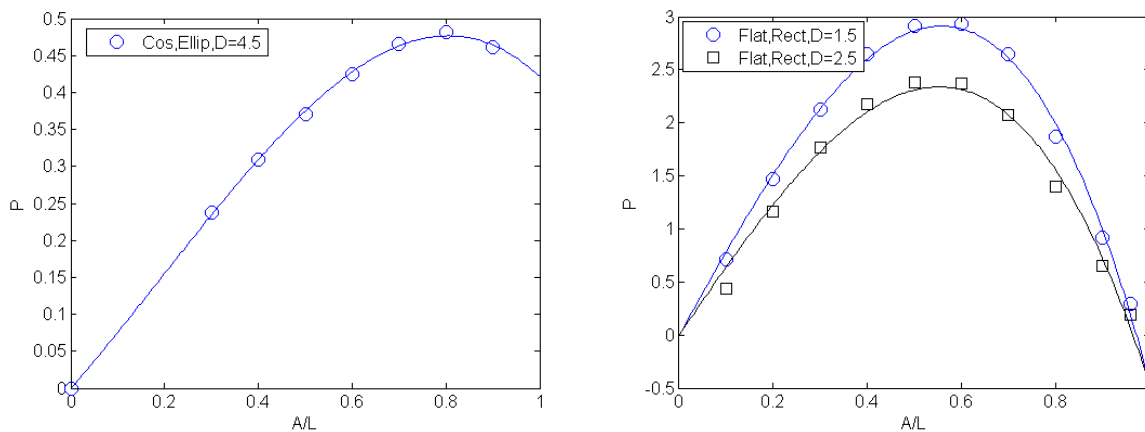


Figure 6.10 Effect of A/L on P for the arc-bottom elliptical dimple and the flat-bottom rectangular dimple, respectively. $B/L=0.9$. The symbols are from the simulation, and the curves are fitted to a third order polynomial.

Based on the above analysis, we obtained an empirical formula,

$$P = F(A/L) \cdot G(D) = [C_1(A/L)^3 + C_2(A/L)^2 + C_3(A/L)] \cdot \frac{D^a}{e^{(C_4 \cdot D^b)} - 1} \quad (6.4)$$

where C_1 , C_2 , C_3 , C_4 , a , and b are the fitted parameters.

Comparing the different combinations of the top geometries and cross sections, Figure 6.11 reveals that the flat-bottom elliptical dimple provides the maximum P_{avg} , at $A/L=0.83$, corresponding to a coverage density of 59% when $B/L=0.9$ at $D=1.35$ (depth=2.7 μm for $H_{ref}=2$ μm), with the generated $P=0.88$ (P_{avg} at 0.88 bar above the ambient pressure).

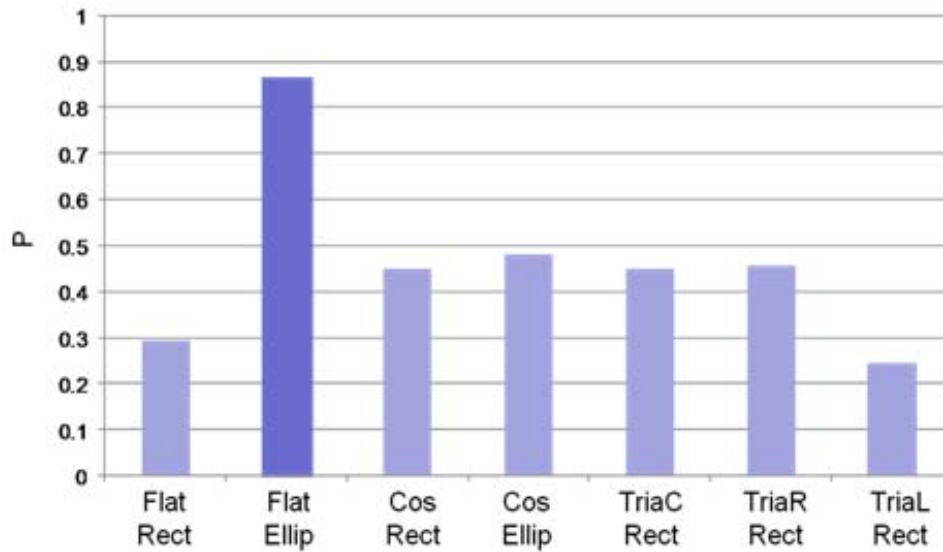


Figure 6.11 Maximum P for various dimple geometries, $B/L=0.9$. The flat-bottom elliptical dimple generated the highest pressure.

The effect of the sliding velocity U is studied, and the results are shown in Figure 6.12. The symbols are the calculated non-dimensionalized $P=P_{avg}/p_0$ from the simulation, and the curves are from the fitted Equation 6.4. Because all the analyses mentioned above are based on a

non-dimensional working condition parameter $\frac{6\eta LU}{H_{ref}^2(p_0 - p_c)}$, the numerical results can also be interpreted as an accumulative effect owing to the changes in the other parameters, such as η , H_{ref} , and L for other applications. Flat-bottom elliptical dimples were used in this study because they had demonstrated an optimal performance in the single texture load-capacity analysis, shown in Figure 6.11. Figure 6.12 suggests that the optimal depth is related to the reference film thickness, $D=d/H_{ref} \approx 1$, or slightly larger than one. As U increases, the optimal depth increases. For the high speed cases, a wide range of speeds are capable of supporting considerably large loads. The design can tolerate a wide range of depths, up to $D=4$ for $U=1$ m/s, and the usable D range could be even larger for higher speeds. When the speed decreases, the texture can no longer generate a noticeable load capacity. When U drops to approximately 0.05 m/s, a noticeable pressure cannot be generated. Meanwhile, the optimal A/L values are consistent, between 0.7 to 0.9, with a slight increase with increasing U , as shown in Figure 6.13.

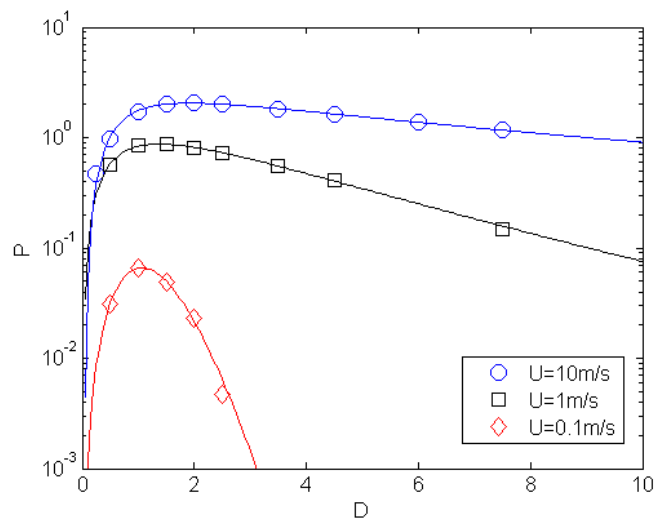


Figure 6.12 Effect of $D=d/H_{ref}$ on pressure $P=P_{avg}/p_0$ at three relative speeds. $B/L=0.9$. The symbols are from the simulation, and the curves are from the fitted Equation 6.4.

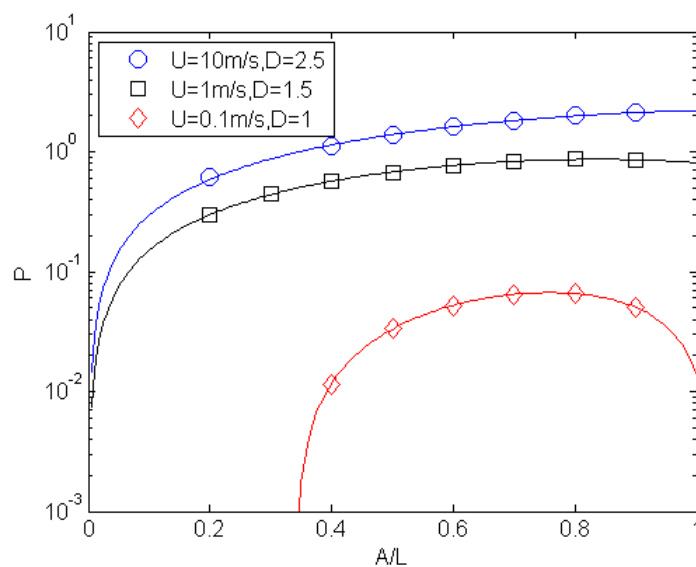


Figure 6.13 Effect of A/L on $P=P_{avg}/p_0$ for various speeds at an appropriate D . $B/L=0.9$. The symbols are from the simulation, and the curves are from the fitted Equation 6.4.

6.3.2 Design and Optimization of Multiple Textures

Analyses of the performance of multiple textures subjected to B.C. 2 are conducted for the study of the effect of N_1 and N_2 on the texture size, namely the optimal A/L value. Flat-bottom elliptical dimples are used for the analyses because they had demonstrated the maximum load capacity in the single texture analysis. For the texture distribution shown in Figure 6.2, two cases are studied: The first case maintains $N_1=1$ but increases N_2 from 1 to $N_2 \gg N_1$, which can be simulated using the periodic boundary conditions along the N_2 direction (B.C.1); The second case keeps $N_2=1$ but increases N_1 from 1 to which correspond to $N_1 \gg N_2$, which can be simulated using B.C.3. The results suggest that as N_2 increases, the optimized A/L value increases (as shown in Figure 6.14), whereas as N_1 increases, the optimized A/L value decreases (as shown in Figure 6.15). For all the cases with $P < 0$, the surface texture generates a negative effect. The following curves are fitted to the previously acquired third-order polynomial relationship for A/L , $F(A/L) = C_1(A/L)^3 + C_2(A/L)^2 + C_3(A/L)$.

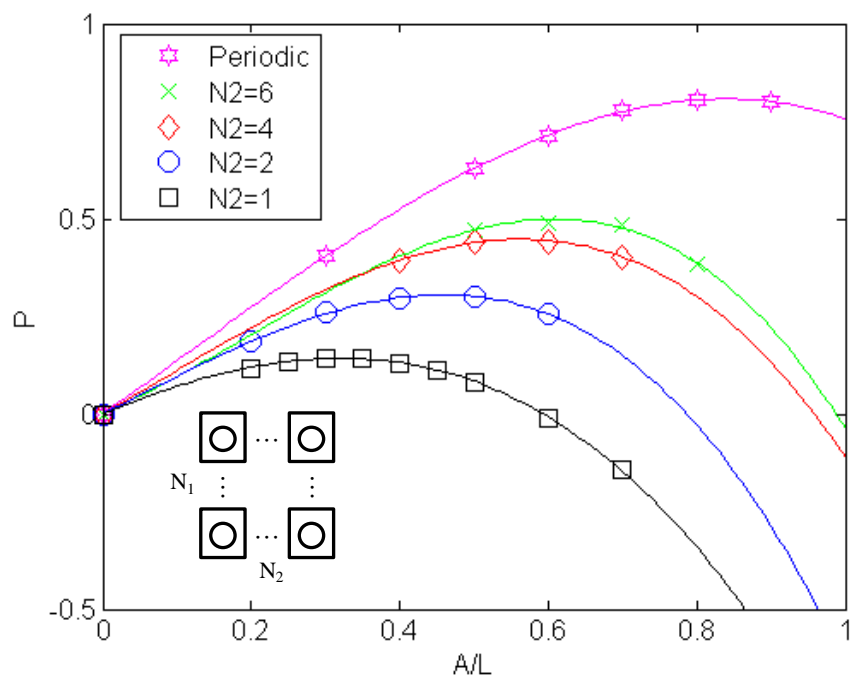


Figure 6.14 Size effect of A/L for multiple dimples with an increasing N_2 . $N_1=1$, $B/L=0.9$. The symbols are from the simulation, and the curves are from the fitted third-order polynomial.

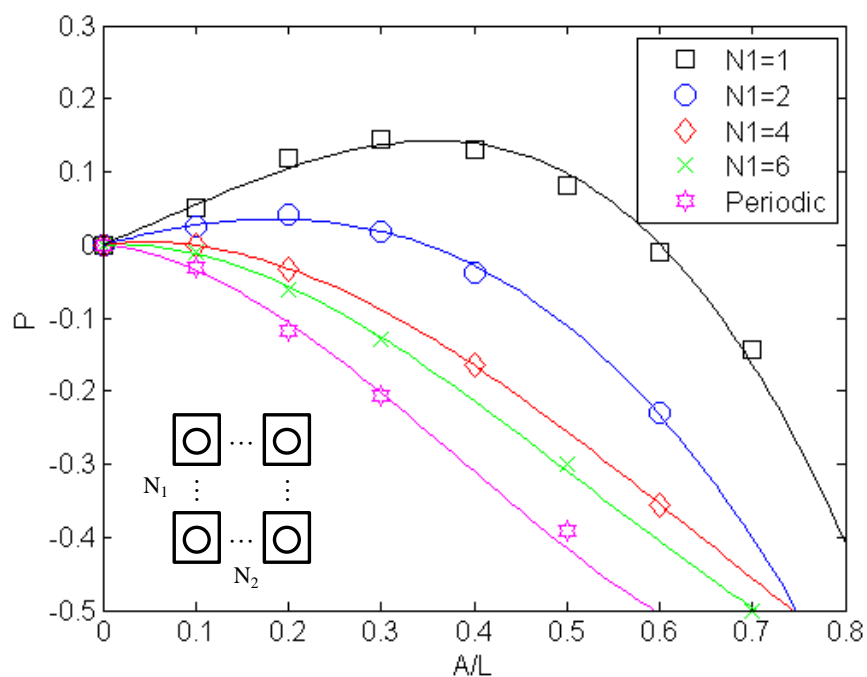


Figure 6.15 Size effect of A/L for multiple dimples with an increasing N_1 . $N_2=1$, $B/L=0.9$. The symbols are from the simulation, and the curves are from the fitted third-order polynomial.

When plotting the relationship between N_2/N_1 and the optimal A/L in Figure 6.16, with B.C.1 and 3 for the both ends (for plotting purposes, set N_2/N_1 at 10^4 for B.C.1 and 10^{-4} for B.C.3, respectively), we can see that the data points land on an almost quarter elliptical curve, and there exists a critical $A/L = \lambda$ (for our case $\lambda=0.4$). For $N_2/N_1 < \lambda$, the textures always generate a negative effect. For the case of $N_1=N_2$, the optimal A/L value is currently only around 0.35, compared to 0.83 for the single texture analysis under B.C.1.

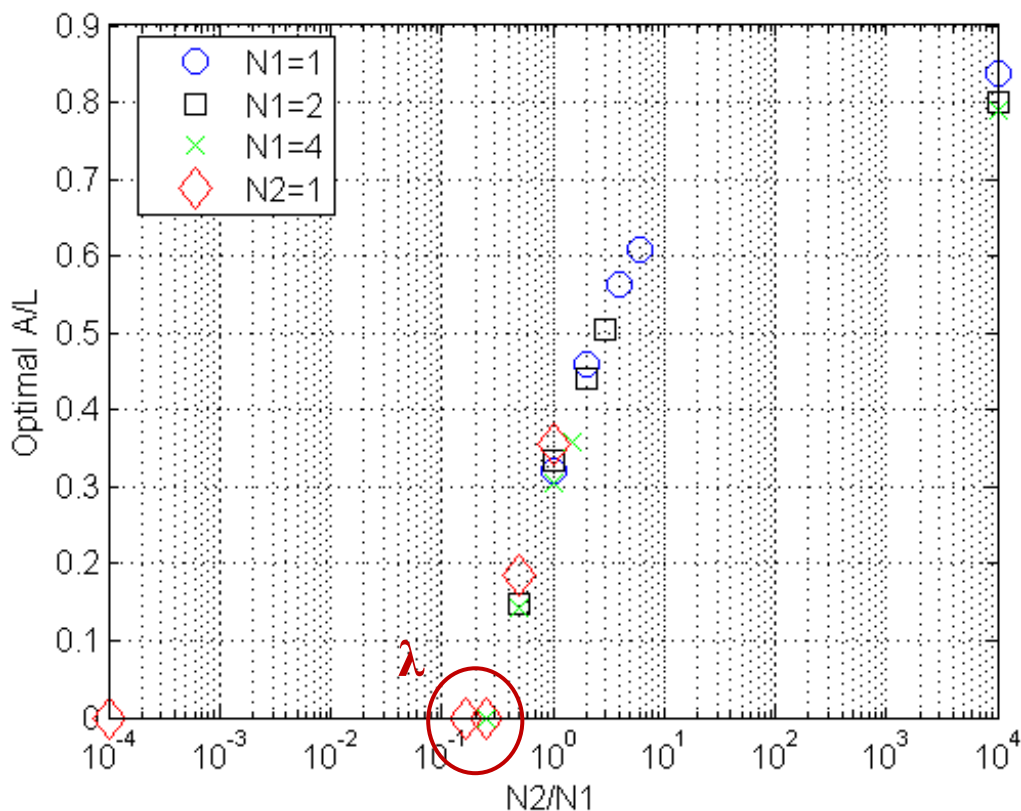


Figure 6.16 Effect of N_2/N_1 on the optimal A/L . $B/L=0.9$. At different N_2/N_1 ratio, the optimal A/L value changes. For $N_2/N_1 < \lambda \approx 0.4$, the textures always generate a negative effect.

6.3.3 Influence of the Original Surface Roughness

The original surface roughness with a Gaussian distribution is generated using the method by Patir [128]. Five surfaces were generated for each case and the optimal single texture geometry for the flat-bottom elliptical dimples was used for the analysis with the application of B.C.1. Figure 6.17 compares the load carrying ability of the textures when combined with different initial RMS surface roughnesses. With no initial surface roughness, the texture would generate the load capacity by itself, as shown in the results presented in the previous section. When only the surface roughness exists without the texture, the surface would generate a non-zero average load that varies based on the magnitude of the surface roughness and the specific surface profile. When we combine the surface texture with the initial surface roughness, the final load generated is the average of the surface texture effect with a variation corresponding to the initial surface roughness. This observation suggests that the final load capacity generation is a combined effect of the two. The comparison between the two cases, $RMS=0.1\ \mu\text{m}$ and $RMS=0.2\ \mu\text{m}$, suggests that as the surface roughness increases, the resulting variation also increases, and the effect of the surface roughness may offset the positive effect of the surface texture.

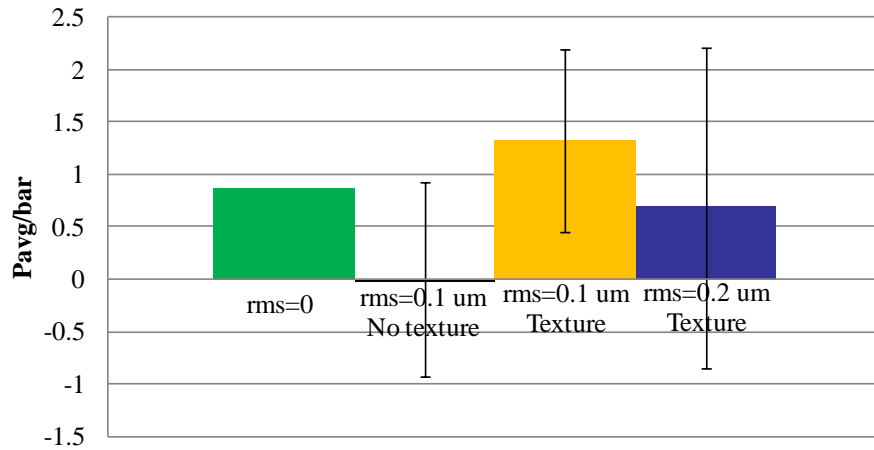


Figure 6.17 Combined effect of the surface texture and surface roughness on P_{avg} for the flat-bottom elliptical dimple with $D=1.5$, $A/L=0.8$, $B/L=0.9$.

Figure 6.17 also suggests that the surface texture we had assigned at the current working conditions is able to tolerate a roughness of $RMS=0.1 \mu\text{m}$ while maintaining its positive effect on the load capacity. Therefore, when designing for different applications, design engineers need to take into consideration the influence of the initial surface roughness for ensuring that the positive effect of the surface roughness is sufficiently large to overcome the variations.

6.3.4 Cavitation Effect

The pressure distribution for single textures is studied to compare the differences caused by the geometric changes. The cavitation pressure $p_c=0$ is below the ambient pressure which is currently set at $p_0=1$ bar; therefore, it causes a negative effect on the load capacity P_{avg} since the ambient pressure is subtracted. The pressure build-up on reaching the geometric step produces a positive load effect and a smaller cavitation region with higher pressure build-up is preferred.

However, when a cavitation no longer exists, the pressure build-up becomes negligible for a noticeable positive load capacity effect. Therefore, the cavitation region cannot be zero.

A comparison between elliptical and rectangular dimples of the same size and depth shown in Figure 6.18 suggests that the elliptical dimples yield a smaller cavitation region and a higher-pressure build-up. This is owing to the fact that the lubricant attains the step edge earlier in the elliptical dimples because of the edge curvature. Physically, this should lead to an inward flow of the lubricant to the center inside the texture, decreasing the cavitation region. Meanwhile, a pressure is generated and accumulates around the central area, and a larger P_{\max} is achieved.

A comparison between flat-bottom elliptical dimples with different A/L values is shown in Figure 6.19. A larger A/L results in a larger cavitation region, suggesting a larger inlet suction effect that generates a higher pressure build-up. Therefore, a balance between the cavitation region and the pressure build-up is necessary for an optimal A/L value.

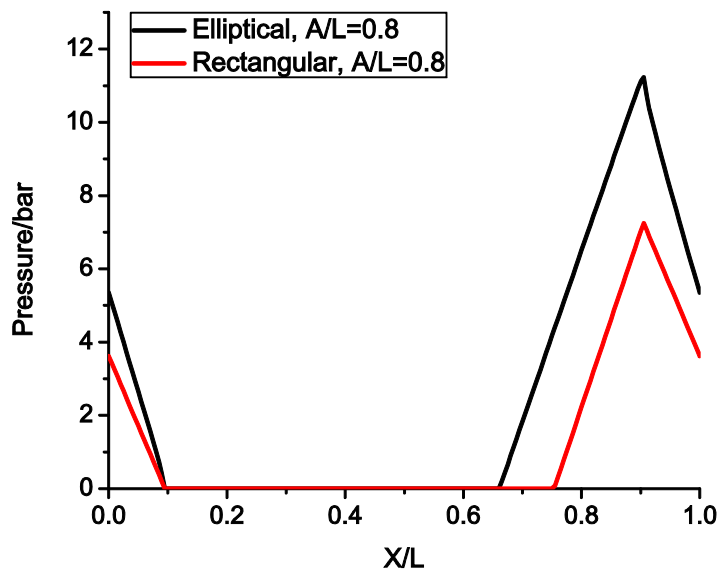


Figure 6.18 Pressure distributions for the cases with different texture top geometries. The elliptical dimple showed smaller cavitation region and a higher pressure build-up.

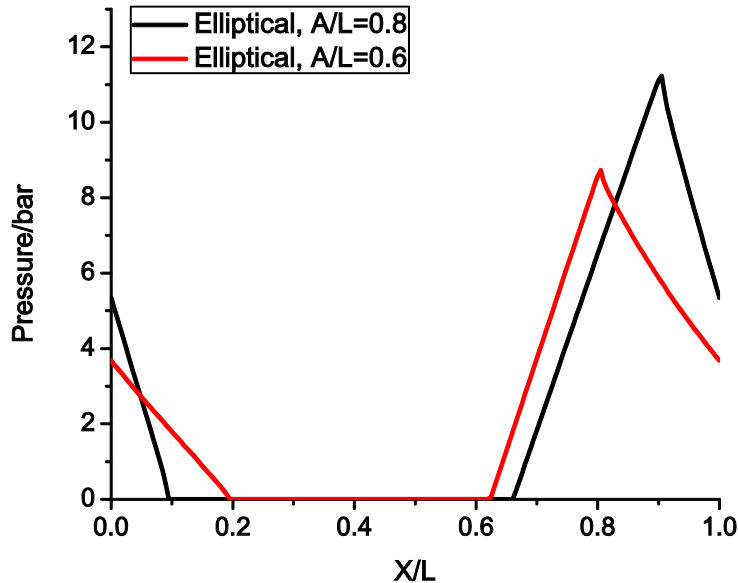


Figure 6.19 Pressure distribution over the textures with the same top geometry but different texture sizes A/L . Larger texture size generated a larger cavitation region with a higher pressure build-up. A balance between the cavitation region and the pressure build-up is necessary for optimization.

Figure 6.20 depicts the behaviors of elliptical top geometry textures with two different bottom shapes, namely, the flat-bottom and the cosine-bottom; the cavitation area is found to be the same. Although the shapes of the inlet are different, under the current working conditions, both still reach cavitation at the immediate edge of the textures. For dimples with a flat-bottom shape, the step generates a higher-pressure build-up compared to the gradual wedge of the cosine shape.

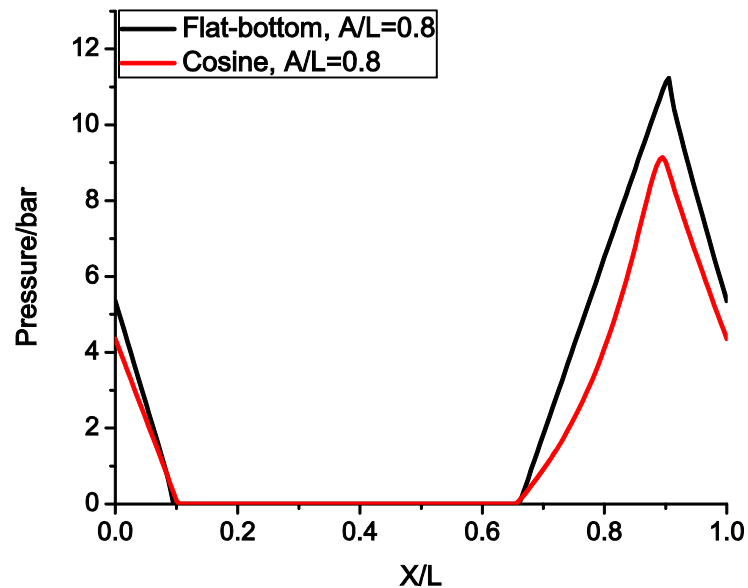


Figure 6.20 Pressure distributions for textures of different cross sections. Compared with the arc-bottom dimple (described with a cosine function), the flat-bottom dimples generated a higher pressure build-up, whereas the cavitation regions are similar.

6.4 Chapter Summary

A mass-conservation model for the lubrication of the interface of two nominally flat and parallel surfaces with textures was developed. The texture geometry was optimized for single

and multiple textures under different boundary conditions. The following conclusions can be made:

- 1) For single texture features analyzed with the periodic boundary condition along the flow direction and the prescribed boundary condition along the perpendicular direction, an empirical formula between the non-dimensionalized $P=P_{avg}/p_0$ and the geometric parameters A/L and depth $D=d/h_{ref}$ is acquired as follows:

$$P = [C_1(A/L)^3 + C_2(A/L)^2 + C_3(A/L)] \cdot \frac{D^a}{e^{(C_4 \cdot D^b)} - 1},$$
 which can be used for texture geometry optimization.

- 2) The optimal single texture geometry was found to be a flat-bottom elliptical dimple with $A/L=0.83$ (coverage density=59%, when $B/L=0.9$) and $D=d/h_{ref}=1.35$, (corresponding to a depth $d=2.7 \mu\text{m}$ when $h_{ref}=2 \mu\text{m}$) under the currently analyzed working conditions.
- 3) Multiple textures design was analyzed by studying the effect of N_1/N_2 with the prescribed boundary conditions along both the directions. As N_1 increases, the optimal A/L value decreases; whereas as N_2 increases, the optimal A/L increases. For the currently analyzed working conditions, when $N_2/N_1 < 0.4$, the textures would always generate a negative effect on the load supporting ability.
- 4) For textures on machined rough surfaces, the resultant load capacity is the combined effects of the surface roughness and the engineered texture; the variation caused by the initial surface roughness may surpass the surface texture effect, if the initial surface is

very rough. For the currently analyzed working conditions, an $\text{RMS}=0.1 \mu\text{m}$ can be tolerated. This may be crucial for surface texturing applications because the effect of the initial surface finish is often overlooked.

Chapter 7 Conclusions

The tribological behaviors of lubricated interfaces are highly affected by the interactions between the mating surfaces and the rheological properties of the lubricant between them. Lubrication improvement requires two approaches, 1) designing surface textures for lubrication enhancement and adhesion reduction, and 2) developing lubricants of desired rheology. The research reported in this thesis tackles both from model-based simulations.

Molecular dynamics simulations enable us to predict the properties of the lubricant based on the molecular structures. However, due to the time- and length- scale limitations, direct viscosity calculations cannot be achieved for high pressure and high molecular weight polymers. In Chapters 2-4, modeling methods were developed to overcome such challenges. The key findings are summarized as following:

In Chapter 2, The viscosities of a branched alkane, 1-Decene trimer, under various pressures and temperatures were calculated through direct NEMD, together with a time-temperature superposition (TTS)-based extrapolations using the simulated results from the NEMD at elevated temperatures, based on the analyses of the rotational relaxation time to determine the successful capture of the 1st Newtonian. The data were used to obtain the pressure-viscosity coefficients, α_0 and α^* , for this typical base oil. The calculated α values well agree with the experimentally measured data, although the absolute values of the shear viscosity

were underestimated by the calculations in general. Well agreed experimental and calculated pressure-viscosity relationships indicate that the proposed model is a promising method for the evaluation of such relationships of base oils in the C₂₀-C₄₀ range. The acquisition of a more accurate and convenient temperature-viscosity model for extrapolation would further improve the accuracy of the α^* prediction.

In Chapter 3, a novel concept of utilizing the change in radius of gyration to predict the critical shear rate is proposed.

- 1) The radii of gyration at various shear rates were calculated for the three molecular structures, 1-Decene trimer (C₃₀H₆₂), squalane (C₃₀H₆₂), and OCP (C₉₀H₁₈₂), respectively. The increase in the radius of gyration at increased shear rates was correlated successfully to the temporary shear thinning behavior of the lubricant. The transition region and the critical shear rate estimated by both the shear thinning curve and the R_g curve agreed reasonably well with each other.
- 2) TTPS of both the viscosity and the R_g data through the MD simulations were also demonstrated for a wide range of temperatures and pressures. Mastercurves for both viscosity and R_g was acquired for the three lubricants.

Utilization of R_g as an indicator provides a method for evaluating the shear thinning behavior of various molecular structures, when a direct acquisition of the viscosity is challenging and at times impractical; TTPS further expands the molecular structures and sizes that can be

evaluated for various applications, and reduces the number of simulation cases needed at specific pressure and temperature once the mastercurve is established.

Chapter 4 reports a MD simulation-assisted viscosity calculation method that combines MD computations with the Berry and Fox type structural-viscosity model for predicting the viscosities of linear and branched polymer lubricants with molecular weights up to 10^5 .

- 1) The viscosities of Polyethylene (PE) and Poly- α -olefin (PAO) with different molecular weights, representing a linear polymer and a branched polymer, respectively, were predicted using the viscosity of a low molecular weight molecule (C_{76} for PE and PAO2-PAO6 for PAO). The results agreed well with experimental data, showing that the modeling method could predict the viscosity high molecular weight molecules using the same monomers.
- 2) The exponent a should be a function of temperature and polymer structure, and its accurate value can be estimated from the slope of multiple low molecular weight liquids. This empirical constant was further modified for PAO based on the MD simulations depending on the individual polymer structures for increasing the accuracy of the model.
- 3) Self-diffusion coefficient can be directly calculated from MD simulations, and it was used to further increase the accuracy of the empirical value, X_c , which is a critical value where the exponent for the viscosity increase changes.

The proposed approach can be a useful method for the development and evaluation of synthetic lubricants because it enables us to build a long-chain polymer with a desired viscosity from a simple, low-weight molecule. It increases the range of the molecular structures that can be explored and reducing the cost of the initial lubricant development.

Chapters 5 and 6 study the effect of surface texturing in different lubrication regimes. The key findings are summarized as following:

Chapter 5 reports the development of a laser texturing process and tooling for texturing cylindrical surfaces. Consistency in manufacturing the surface textures was achieved. This process was applied for surface texturing drill bits to reduce chip adhesion and enhance drill life.

- 1) Three drill bit groups were textured and tested, which are non-textured drills, and those with 10% and 20% of the drill margin surface textured. A larger area of workpiece adhesion on the drill bit margin is directly linked to tool failure. Textured drill bits were found to exhibit less adhesion and improved the shedding of the adhered chips hole-to-hole.
- 2) The shedding of the build-up ultimately led to a reduction in chip adhesion and therefore, extended the tool life. While 100% of non-textured drills failed at or before 60 holes were drilled, both of the texture designs tested (with 10% and 20% of the drill margin surface area textured) only resulted in a 33% failure when 60 holes were drilled.

- 3) No discernible difference was found between the two texture designs in terms of the drill life at the tested conditions.

The results from this portion of the study reveal that creating textures on the margins of drill bits is a promising method for these purposes. Rectangular texture features with a triangular distribution pattern appear to be promising texture designs.

A mass-conservation model for the lubrication of the interface of two nominally flat and parallel surfaces with textures was developed. The texture geometry was optimized for single and multiple textures under different boundary conditions. The following conclusions can be made:

- 1) For single texture features analyzed with the periodic boundary condition along the flow direction and the prescribed boundary condition along the perpendicular direction, an empirical formula between the non-dimensionalized $P=P_{avg}/p_0$ and the geometric parameters A/L and depth $D=d/h_{ref}$ is acquired as follows:

$$P = [C_1(A/L)^3 + C_2(A/L)^2 + C_3(A/L)] \cdot \frac{D^a}{e^{(C_4 \cdot D^b)} - 1},$$
 which can be used for texture geometry optimization.

- 2) The optimal single texture geometry was found to be a flat-bottom elliptical dimple with $A/L=0.83$ (coverage density=59%, when $B/L=0.9$) and $D=d/h_{ref}=1.35$, (corresponding to a depth $d=2.7 \mu\text{m}$ when $h_{ref}=2 \mu\text{m}$) under the currently analyzed working conditions.

- 3) Multiple textures design was analyzed by studying the effect of N_1/N_2 with the prescribed boundary conditions along both the directions. As N_1 increases, the optimal A/L value decreases; whereas as N_2 increases, the optimal A/L increases. For the currently analyzed working conditions, when $N_2/N_1 < 0.4$, the textures would always generate a negative effect on the load supporting ability.
- 4) For textures on machined rough surfaces, the resultant load capacity is the combined effects of the surface roughness and the engineered texture; the variation caused by the initial surface roughness may surpass the surface texture effect, if the initial surface is very rough. For the currently analyzed working conditions, an RMS=0.1 μm can be tolerated. This may be crucial for surface texturing applications because the effect of the initial surface finishes is often overlooked.

The results in this study provide multiple tools for advancing the understanding of lubrication performances at the lubricated interfaces and designing of mating surface topography and the lubricant between them. The rheological modeling of the lubricant enables us to predict the viscosity of the lubricant based on its molecular structure, and the operating temperature, pressure and shear rates. The predictive capabilities of the models enable us to develop and tailor the lubricant to offer optimal performances at the working interfaces. The positive effects of the surface textures on the mating surfaces were demonstrated both experimentally and numerically. Guidelines for texture design and promising texture patterns were provided. At the given

working conditions, either one or both of these solutions can be utilized for improving the tribological performances of lubricating interfaces.

References

1. Jost, H.P.: Lubrication (tribology) education and research. A Report on the Present Position and Industry Needs, Department of Education and Science, HM Stationary Office, London (1966).
2. Holmberg, K., Andersson, P., Erdemir, A.: Global energy consumption due to friction in passenger cars. *Tribology International* **47**, 221-234 (2012).
3. Stribeck, R.: Kugellager für beliebige Belastungen (Ball Bearings for any Stress). *Zeitschrift des Vereins Deutscher Ingenieure*(45) (1901).
4. Stribeck, R.: Die wesentlichen Eigenschaften der Gleit- und Rollenlager (Characteristics of Plain and Roller Bearings). *Zeitschrift des Vereins Deutscher Ingenieure*(46) (1902).
5. Jacobson, B.: The Stribeck memorial lecture. *Tribology International* **36**(11), 781-789 (2003).
6. Woydt, M., Wäsche, R.: The history of the Stribeck curve and ball bearing steels: The role of Adolf Martens. *Wear* **268**(11–12), 1542-1546 (2010).
7. Wang, Y., Wang, Q.J., Lin, C., Shi, F.: Development of a set of Stribeck curves for conformal contacts of rough surfaces. *Tribology Transactions* **49**(4), 526-535 (2006).
8. Bair, S., Liu, Y., Wang, Q.J.: The pressure-viscosity coefficient for Newtonian EHL film thickness with general piezoviscous response. *Journal of Tribology* **128**(3), 624-631 (2006).
9. Bair, S., Qureshi, F.: Accurate measurements of pressure-viscosity behavior in lubricants. *Tribology Transactions* **45**(3), 390-396 (2002).
10. Seeton, C.: Viscosity–temperature correlation for liquids. *Tribology Letters* **22**(1), 67-78 (2006).
11. Totten, G.E., Westbrook, S.R., Shah, R.J.: *Fuels and lubricants handbook: technology, properties, performance, and testing*, vol. 37. ASTM International, (2003)
12. Vogel, H.: Das temperaturabhängigkeitsgesetz der viskosität von flüssigkeiten. *Phys. Z* **22**, 645-646 (1921).
13. Fulcher, G.S.: Analysis of recent measurements of the viscosity of glasses. *Journal of the American Ceramic Society* **8**(6), 339-355 (1925).

14. Tammann, G., Hesse, W.: Die Abhängigkeit der Viscosität von der Temperatur bei unterkühlten Flüssigkeiten. *Zeitschrift für anorganische und allgemeine Chemie* **156**(1), 245-257 (1926).
15. Stachowiak, G., Batchelor, A.W.: *Engineering tribology*. Butterworth-Heinemann, (2013)
16. Schaschke, C.J.: High Pressure Viscosity Measurement with Falling Body Type Viscometers. *International Review of Chemical Engineering-Rapid Communications* **2**(5), 564-576 (2010).
17. Bair, S.: A Routine High-Pressure Viscometer for Accurate Measurements to 1 GPa. *Tribology Transactions* **47**(3), 356-360 (2004).
18. Cook, R.L., Herbst, C.A., King Jr, H.: High-pressure viscosity of glass-forming liquids measured by the centrifugal force diamond anvil cell viscometer. *The Journal of Physical Chemistry* **97**(10), 2355-2361 (1993).
19. Hamrock, B.J., Dowson, D.: Isothermal elastohydrodynamic lubrication of point contacts: Part III—fully flooded results. *Journal of Lubrication Technology* **99**(2), 264-275 (1977).
20. Hamrock, B.J., Dowson, D.: Isothermal Elastohydrodynamic Lubrication of Point Contacts: Part 1—Theoretical Formulation. *Journal of Lubrication Technology* **98**(2), 223-228 (1976).
21. Ramasamy, U.S., Bair, S., Martini, A.: Predicting Pressure–Viscosity Behavior from Ambient Viscosity and Compressibility: Challenges and Opportunities. *Tribology Letters* **57**(2), 1-7 (2015).
22. Wu, C., Klaus, E., Duda, J.: Development of a method for the prediction of pressure-viscosity coefficients of lubricating oils based on free-volume theory. *Journal of tribology* **111**(1), 121-128 (1989).
23. Mondello, M., Grest, G.S.: Molecular dynamics of linear and branched alkanes. *The Journal of chemical physics* **103**(16), 7156-7165 (1995).
24. Nath, S.K., Escobedo, F.A., de Pablo, J.J.: On the simulation of vapor–liquid equilibria for alkanes. *The Journal of chemical physics* **108**, 9905 (1998).
25. Martin, M.G., Siepmann, J.I.: Novel configurational-bias Monte Carlo method for branched molecules. Transferable potentials for phase equilibria. 2. United-atom description of branched alkanes. *The Journal of Physical Chemistry B* **103**(21), 4508-4517 (1999).

26. Padilla, P., Toxværd, S.: Self-diffusion in n-alkane fluid models. *The Journal of chemical physics* **94**(8), 5650-5654 (1991).
27. Chang, J., Sandler, S.I.: Interatomic Lennard-Jones potentials of linear and branched alkanes calibrated by Gibbs ensemble simulations for vapor-liquid equilibria. *The Journal of chemical physics* **121**(15), 7474-7483 (2004).
28. Evans, D.J., Morriss, G.: *Statistical mechanics of nonequilibrium liquids*. Cambridge University Press, (2008)
29. Morriss, G.P., Daivis, P.J., Evans, D.J.: The rheology of n alkanes: Decane and eicosane. *The Journal of chemical physics* **94**(11), 7420-7433 (1991).
30. Cui, S., Cummings, P., Cochran, H., Moore, J., Gupta, S.: Nonequilibrium molecular dynamics simulation of the rheology of linear and branched alkanes. *International journal of thermophysics* **19**(2), 449-459 (1998).
31. Cui, S., Gupta, S., Cummings, P., Cochran, H.: Molecular dynamics simulations of the rheology of normal decane, hexadecane, and tetracosane. *Journal of Chemical Physics* **105**(3), 1214-1220 (1996).
32. Khare, R., de Pablo, J., Yethiraj, A.: Rheological, thermodynamic, and structural studies of linear and branched alkanes under shear. *The Journal of chemical physics* **107**, 6956 (1997).
33. Kioupis, L.I., Maginn, E.J.: Molecular simulation of poly- α -olefin synthetic lubricants: impact of molecular architecture on performance properties. *The Journal of Physical Chemistry B* **103**(49), 10781-10790 (1999).
34. Moore, J., Cui, S., Cochran, H., Cummings, P.: Rheology of lubricant basestocks: A molecular dynamics study of C30 isomers. *The Journal of chemical physics* **113**(19), 8833-8840 (2000).
35. Jabbarzadeh, A., Atkinson, J., Tanner, R.: Effect of molecular shape on rheological properties in molecular dynamics simulation of star, H, comb, and linear polymer melts. *Macromolecules* **36**(13), 5020-5031 (2003).
36. Moore, J., Cui, S., Cummings, P., Cochran, H.: Lubricant characterization by molecular simulation. *American Institute of Chemical Engineers. AIChE Journal* **43**(12), 3260-3263 (1997).

37. Mundy, C.J., Klein, M.L., Siepmann, J.I.: Determination of the Pressure-Viscosity Coefficient of Decane by Molecular Simulation. *The Journal of Physical Chemistry* **100**(42), 16779-16781 (1996).
38. Kioupi, L.I., Maginn, E.J.: Impact of molecular architecture on the high-pressure rheology of hydrocarbon fluids. *The Journal of Physical Chemistry B* **104**(32), 7774-7783 (2000).
39. McCabe, C., Cui, S., Cummings, P.T., Gordon, P.A., Saeger, R.B.: Examining the rheology of 9-octylheptadecane to giga-pascal pressures. *The Journal of chemical physics* **114**, 1887 (2001).
40. Bair, S., Qureshi, F.: The generalized Newtonian fluid model and elastohydrodynamic film thickness. *Journal of Tribology* **125**(1), 70-75 (2003).
41. Gordon, P.A.: Development of intermolecular potentials for predicting transport properties of hydrocarbons. *The Journal of chemical physics* **125**, 014504 (2006).
42. Gordon, P.A.: Characterizing isoparaffin transport properties with Stokes-Einstein relationships. *Industrial & engineering chemistry research* **42**(26), 7025-7036 (2003).
43. Pan, G., McCabe, C.: Prediction of viscosity for molecular fluids at experimentally accessible shear rates using the transient time correlation function formalism. *The Journal of chemical physics* **125**, 194527 (2006).
44. Morriss, G.P., Evans, D.J.: Application of transient correlation functions to shear flow far from equilibrium. *Physical Review A* **35**(2), 792 (1987).
45. Evans, D.J., Morriss, G.P.: Transient-time-correlation functions and the rheology of fluids. *Physical Review A* **38**(8), 4142 (1988).
46. Bair, S., McCabe, C., Cummings, P.T.: Comparison of nonequilibrium molecular dynamics with experimental measurements in the nonlinear shear-thinning regime. *Physical Review Letters* **88**(5), 58302 (2002).
47. Hansen, J.-P., McDonald, I.R.: *Theory of simple liquids*. Elsevier, (1990)
48. Williams, G., Watts, D.C.: Non-symmetrical dielectric relaxation behaviour arising from a simple empirical decay function. *Transactions of the Faraday Society* **66**, 80-85 (1970).

49. Bair, S.: The high pressure rheology of some simple model hydrocarbons. Proceedings of the Institution of Mechanical Engineers, Part J: Journal of Engineering Tribology **216**(3), 139-149 (2002).
50. Siepmann, J.I., Karaborni, S., Smit, B.: Simulating the critical behaviour of complex fluids. Nature **365**, 330-332 (1993).
51. Mundy, C.J., Siepmann, J.I., Klein, M.L.: Calculation of the shear viscosity of decane using a reversible multiple time-step algorithm. The Journal of chemical physics **102**(8), 3376 (1995).
52. Lennard-Jones, J.E.: Cohesion. Proceedings of the Physical Society **43**(5), 461 (1931).
53. Jorgensen, W.L., Madura, J.D., Swenson, C.J.: Optimized intermolecular potential functions for liquid hydrocarbons. Journal of the American Chemical Society **106**(22), 6638-6646 (1984).
54. Plimpton, S.: Fast parallel algorithms for short-range molecular dynamics. Journal of Computational Physics **117**(1), 1-19 (1995).
55. <http://lammps.sandia.gov>: LAMMPS WWW Site.
56. Lees, A., Edwards, S.: The computer study of transport processes under extreme conditions. Journal of Physics C: Solid State Physics **5**(15), 1921 (1972).
57. Tuckerman, M.E., Mundy, C.J., Balasubramanian, S., Klein, M.L.: Modified nonequilibrium molecular dynamics for fluid flows with energy conservation. The Journal of chemical physics **106**(13), 5615-5621 (1997).
58. http://www.cpchem.com/msds/100000010950_SDS_JP_EN.PDF: Material Safety Data Sheet for PAO 4 cSt.
59. Booser, E.R.: CRC handbook of lubrication. Theory and practice of tribology: Volume II: Theory and design. (1984).
60. Rudnick, L.R.: Lubricant additives: chemistry and applications. CRC press, (2009)
61. Mezger, T.G.: The rheology handbook: for users of rotational and oscillatory rheometers. Vincentz Network GmbH & Co KG, (2006)

62. Goksem, P., Hargreaves, R.: The Effect of Viscous Shear Heating on Both Film Thickness and Rolling Traction in an EHL Line Contact—Part I: Fully Flooded Conditions. *Journal of Lubrication Technology* **100**(3), 346-352 (1978).
63. Spikes, H., Jie, Z.: History, origins and prediction of elastohydrodynamic friction. *Tribology Letters* **56**(1), 1-25 (2014).
64. Zolper, T.J., Seyam, A.M., Chen, C., Jungk, M., Stammer, A., Stoegbauer, H., Marks, T.J., Chung, Y.-W., Wang, Q.: Energy efficient siloxane lubricants utilizing temporary shear-thinning. *Tribology Letters* **49**(3), 525-538 (2013).
65. Qureshi, F., Bair, S.: Time-Temperature-Pressure Superposition in Polymer Thickened Liquid Lubricants. *Journal of Tribology* **136**(2), 021505 (2014).
66. Harris, K.R.: Temperature and pressure dependence of the viscosities of 2-ethylhexyl benzoate, bis (2-ethylhexyl) phthalate, 2, 6, 10, 15, 19, 23-hexamethyltetracosane (squalane), and diisodecyl phthalate†. *Journal of Chemical & Engineering Data* **54**(9), 2729-2738 (2009).
67. Mortier, R.M., Orszulik, S.T., Fox, M.F.: *Chemistry and technology of lubricants*, vol. 107115. Springer, (2010)
68. Coffin, P., Lindsay, C., Mills, A., Lindenkamp, H., Fuhrmann, J.: The application of synthetic fluids to automotive lubricant development: Trends today and tomorrow. *Journal of Synthetic Lubrication* **7**(2), 123-143 (1990).
69. Wang, J., Ye, Z., Zhu, S.: Topology-engineered hyperbranched high-molecular-weight polyethylenes as lubricant viscosity-index improvers of high shear stability. *Industrial & engineering chemistry research* **46**(4), 1174-1178 (2007).
70. Stöhr, T., Eisenberg, B., Müller, M.: A new generation of high performance viscosity modifiers based on comb polymers. *SAE International Journal of Fuels and Lubricants* **1**(2008-01-2462), 1511-1516 (2008).
71. Morgan, S., Ye, Z., Subramanian, R., Zhu, S.: Higher-molecular-weight hyperbranched polyethylenes containing crosslinking structures as lubricant viscosity-index improvers. *Polymer Engineering & Science* **50**(5), 911-918 (2010).
72. Berry, G., Fox, T.: The viscosity of polymers and their concentrated solutions. *Fortschritte der Hochpolymeren-Forschung*, 261-357 (1968).

73. Nagendramma, P., Kaul, S.: Development of ecofriendly/biodegradable lubricants: An overview. *Renewable and Sustainable Energy Reviews* **16**(1), 764-774 (2012).
74. Saxena, K., Bisaria, C., Saxena, A.: Synthesis and characterization of some novel silicon esters and their application as lubricant base stock solution. *Applied Organometallic Chemistry* **23**(12), 535-540 (2009).
75. Weller Jr, D.E., Perez, J.M.: A study of the effect of chemical structure on friction and wear: Part 1--synthetic ester base fluids. *Tribology & Lubrication Technology* **56**(11), 39 (2000).
76. Ray, S., Rao, P.V., Choudary, N.V.: Poly- α -olefin-based synthetic lubricants: a short review on various synthetic routes. *Lubrication Science* **24**(1), 23-44 (2012).
77. Brown, M., Fotheringham, J., Hoyes, T., Mortier, R., Orszulik, S., Randles, S., Stroud, P.: Synthetic base fluids. In: *Chemistry and Technology of Lubricants*. pp. 35-74. Springer, (2010)
78. Pourhossaini, M.R., Vasheghani-Farahani, E., Gholamian, M., Gholamian, M.: Synthesis and characterization of olefin copolymers as viscosity modifiers for engine oil. *Iranian Polymer Journal* **14**(6), 549 (2005).
79. Thong, D., Hutchinson, P.A., Wincierz, C., Schimmel, T.: Viscosity modifiers. In: *Encyclopedia of Lubricants and Lubrication*. pp. 2292-2316. Springer, (2014)
80. Tanveer, S., Prasad, R.: Enhancement of viscosity index of mineral base oils. *Indian journal of chemical technology* **13**(4), 398 (2006).
81. Mach, H., Rath, P.: Highly reactive polyisobutene as a component of a new generation of lubricant and fuel additives. *Lubrication Science* **11**(2), 175-185 (1999).
82. Bair, S., Qureshi, F.: The high pressure rheology of polymer-oil solutions. *Tribology International* **36**(8), 637-645 (2003).
83. Liou, I., Tsiang, R.C.C., Wu, J., Liou, J.S., Sheu, H.C.: Synthesis of a star-shaped poly (ethylene-co-propylene) copolymer as a viscosity index improver for lubricants. *Journal of applied polymer science* **83**(9), 1911-1918 (2002).
84. Wang, T.Y., Tsiang, R.C.C., Liou, J.S., Wu, J., Sheu, H.C.: Preparation and characterization of a star-shaped polystyrene-b-poly (ethylene-co-propylene) block copolymer as a viscosity index improver of lubricant. *Journal of applied polymer science* **79**(10), 1838-1846 (2001).

85. Stambaugh, R.: Viscosity index improvers and thickeners. In: Chemistry and technology of lubricants. pp. 124-159. Springer, (1994)
86. Schaeffgen, J.R., Flory, P.J.: Synthesis of multichain polymers and investigation of their viscosities I. Journal of the American Chemical Society **70**(8), 2709-2718 (1948).
87. Fox, T.: Properties of dilute polymer solutions III: Intrinsic viscosity/temperature relationships for conventional polymethyl methacrylate. Polymer **3**, 111-128 (1962).
88. Fox, T.G., Allen, V.R.: Dependence of the Zero Shear Melt Viscosity and the Related Friction Coefficient and Critical Chain Length on Measurable Characteristics of Chain Polymers. The Journal of chemical physics **41**(2), 344 (1964).
89. Harmandaris, V., Mavrantzas, V., Theodorou, D., Kröger, M., Ramirez, J., Öttinger, H., Vlassopoulos, D.: Crossover from the rouse to the entangled polymer melt regime: signals from long, detailed atomistic molecular dynamics simulations, supported by rheological experiments. Macromolecules **36**(4), 1376-1387 (2003).
90. Martin, M.G., Siepmann, J.I.: Transferable potentials for phase equilibria. 1. United-atom description of n-alkanes. The Journal of Physical Chemistry B **102**(14), 2569-2577 (1998).
91. Linxi, Z., Kuiqi, G.: Simulation studies of mean-square radius of gyration of polyethylene chains. European polymer journal **29**(12), 1631-1633 (1993).
92. Bonchev, D., Markel, E.J., Dekmezian, A.H.: Long chain branch polymer chain dimensions: application of topology to the Zimm–Stockmayer model. Polymer **43**(1), 203-222 (2002).
93. Wiener, H.: Structural determination of paraffin boiling points. Journal of the American Chemical Society **69**(1), 17-20 (1947).
94. Zimm, B.H., Stockmayer, W.H.: The dimensions of chain molecules containing branches and rings. The Journal of chemical physics **17**(12), 1301-1314 (1949).
95. Pearson, D.S., Fetters, L.J., Graessley, W.W., Ver Strate, G., von Meerwall, E.: Viscosity and self-diffusion coefficient of hydrogenated polybutadiene. Macromolecules **27**(3), 711-719 (1994).
96. Lohse, D., Milner, S., Fetters, L., Xenidou, M., Hadjichristidis, N., Mendelson, R., Garcia-Franco, C., Lyon, M.: Well-defined, model long chain branched polyethylene. 2. Melt rheological behavior. Macromolecules **35**(8), 3066-3075 (2002).

97. Rahalkar, R., Lamb, J., Harrison, G., Barlow, A., Hawthorne, W., Semlyen, J., North, A., Pethrick, R.: Viscoelastic studies of reptational motion of linear polydimethylsiloxanes. In: Faraday Symposia of the Chemical Society 1983, pp. 103-114. Royal Society of Chemistry (1965)
98. https://imageserv10.team-logic.com/mediaLibrary/440/SCC_Presentation_PureSyn_PAO.pdf: PureSynTM Polyalphaolefins (PAO) - Team-Logic.
99. Tian, H., Saka, N., Suh, N.: Boundary Lubrication Studies on Undulated Titanium Surfaces. Tribology Transactions **32**(3), 289-296 (1988).
100. Wakuda, M., Yamauchi, Y., Kanzaki, S., Yasuda, Y.: Effect of surface texturing on friction reduction between ceramic and steel materials under lubricated sliding contact. Wear **254**(3-4), 356-363 (2003).
101. Geiger, M., Popp, U., Engel, U.: Excimer laser micro texturing of cold forging tool surfaces - Influence on tool life. Cirp Annals-Manufacturing Technology **51**(1), 231-234 (2002).
102. Etsion, I.: State of the Art in Laser Surface Texturing. Journal of Tribology **127**(1), 248 (2005).
103. Pettersson, U., Jacobson, S.: Influence of surface texture on boundary lubricated sliding contacts. Tribology International **36**(11), 857-864 (2003).
104. Etsion, I., Halperin, G.: A Laser Surface Textured Hydrostatic Mechanical Seal. Tribology Transactions **45**(3), 430-434 (2002).
105. Kovalchenko, A., Ajayi, O., Erdemir, A., Fenske, G., Etsion, I.: The effect of laser surface texturing on transitions in lubrication regimes during unidirectional sliding contact. Tribology International **38**(3), 219-225 (2005).
106. Kawasegi, N., Sugimori, H., Morimoto, H., Morita, N., Hori, I.: Drilling aluminum alloy using small-diameter drills with micro/nanometer-scale textures. Transactions of the Japan Society of Mechanical Engineers, Part C **76**(762), 446.452 (2010).
107. Sugihara, T., Enomoto, T.: Development of a cutting tool with a nano/micro-textured surface-Improvement of anti-adhesive effect by considering the texture patterns. Precision Engineering **33**(4), 425-429 (2009).

108. Lei, S.T., Devarajan, S., Chang, Z.H.: A study of micropool lubricated cutting tool in machining of mild steel. *Journal of Materials Processing Technology* **209**(3), 1612-1620 (2009).
109. Neves, D., Diniz, A.E., de Lima, M.S.: Efficiency of the laser texturing on the adhesion of the coated twist drills. *Journal of Materials Processing Technology* **179**(1-3), 139-145 (2006).
110. Etsion, I., Kligerman, Y., Halperin, G.: Analytical and Experimental Investigation of Laser-Textured Mechanical Seal Faces. *Tribology Transactions* **42**(3), 511-516 (1999).
111. Coyne, E., O'Connor, G.M., Mannion, P., Magee, J., Glynn, T.J.: Analysis of thermal damage in bulk silicon with femtosecond laser micromachining. *Lasers and Applications in Science and Engineering. International Society for Optics and Photonics*, 73-83 (2004).
112. Hellrung, D., Gillner, A., Poprawe, R.: Laser beam removal of microstructures with Nd:YAG lasers. *Lasers and Optics in Manufacturing III. International Society for Optics and Photonics*, 267-273 (1997).
113. Davis, T., Zhou, R., Pallav, K., Beltran, M., Cao, J., Ehmann, K., Wang, Q.J., Xia, C., Talwar, R., Lederich, R.: Experimental Friction Study of Micro-Scale Laser-Textured Surfaces. Paper presented at the International Workshop on Microfactories, Evanston, IL, (2008)
114. Meng, F., Zhou, R., Davis, T., Cao, J., Wang, Q.J., Hua, D., Liu, J.: Study on effect of dimples on friction of parallel surfaces under different sliding conditions. *Applied Surface Science* **256**(9), 2863-2875 (2010).
115. Zhu, D., Nanbu, N., Ren, N., Yasuda, Y., Wang, Q.: Model-Based Virtual Surface Texturing for Concentrated Conformal-Contact Lubrication. *Proceedings of the Institution of Mechanical Engineers, Part J: Journal of Engineering Tribology* **224**(8), 685-696 (2010).
116. Ren, N., Nanbu, T., Yasuda, Y., Zhu, D., Wang, Q.: Micro Textures in Concentrated-Conformal-Contact Lubrication: Effect of Distribution Patterns. *Tribology Letters* **28**(3), 275-285 (2007).
117. Wang, Q.J., Zhu, D.: Virtual Texturing: Modeling the Performance of Lubricated Contacts of Engineered Surfaces. *Journal of Tribology* **127**(4), 722 (2005).

118. Wang, X., Kato, K., Adachi, K., Aizawa, K.: Loads carrying capacity map for the surface texture design of SiC thrust bearing sliding in water. *Tribology International* **36**(3), 189-197 (2003).
119. Etsion, I., Halperin, G., Brizmer, V., Kligerman, Y.: Experimental Investigation of Laser Surface Textured Parallel Thrust Bearings. *Tribology Letters* **17**(2), 295-300 (2004).
120. Lu, X., Khonsari, M.M.: An Experimental Investigation of Dimple Effect on the Stribeck Curve of Journal Bearings. *Tribology Letters* **27**(2), 169-176 (2007).
121. Brizmer, V., Kligerman, Y., Etsion, I.: A Laser Surface Textured Parallel Thrust Bearing. *Tribology Transactions* **46**(3), 397-403 (2003).
122. Rahmani, R., Shirvani, A., Shirvani, H.: Optimization of Partially Textured Parallel Thrust Bearings with Square-Shaped Micro-Dimples. *Tribology Transactions* **50**(3), 401-406 (2007).
123. Nanbu, T., Ren, N., Yasuda, Y., Zhu, D., Wang, Q.J.: Micro-Textures in Concentrated Conformal-Contact Lubrication: Effects of Texture Bottom Shape and Surface Relative Motion. *Tribology Letters* **29**(3), 241-252 (2008).
124. Yu, H., Wang, X., Zhou, F.: Geometric Shape Effects of Surface Texture on the Generation of Hydrodynamic Pressure Between Conformal Contacting Surfaces. *Tribology Letters* **37**(2), 123-130 (2009).
125. Tala-Ighil, N., Fillon, M., Maspeyrot, P.: Effect of textured area on the performances of a hydrodynamic journal bearing. *Tribology International* **44**(3), 211-219 (2011).
126. Dobrica, M.B., Fillon, M.: Thermohydrodynamic Behavior of a Slider Pocket Bearing. *Journal of Tribology* **128**(2), 312 (2006).
127. Shinkarenko, A., Kligerman, Y., Etsion, I.: The effect of surface texturing in soft elasto-hydrodynamic lubrication. *Tribology International* **42**(2), 284-292 (2009).
128. Jacobson, B.O., Hamrock, B.J.: High-Speed Motion Picture Camera Experiments of Cavitation in Dynamically Loaded Journal Bearings. *Journal of Lubrication Technology* **105**(3), 446-452 (1983).
129. Jakobsson, B., Floberg, L.: The finite journal bearing considering vaporization. *Transactions of Chalmers University of Technology, Goteborg, Sweden* **190**, 1-119 (1957).

130. Olsson, K.O.: Cavitation in dynamically loaded bearing. Transactions of Chalmers University of Technology, Gothenburg, Sweden **308** (1965).